



## Review

# Isoscalar and isovector dipole excitations: Nuclear properties from low-lying states and from the isovector giant dipole resonance

A. Bracco <sup>a,b,\*</sup>, E.G. Lanza <sup>c</sup>, A. Tamii <sup>d</sup><sup>a</sup> Dipartimento di Fisica dell'Università degli Studi di Milano, Italy<sup>b</sup> INFN, Sezione di Milano, Italy<sup>c</sup> INFN, Sezione di Catania, Italy<sup>d</sup> Research Center for Nuclear Physics, Osaka University, Japan

## ARTICLE INFO

## Article history:

Available online 27 February 2019

## Keywords:

Pygmy dipole resonance

Isoscalar dipole excitation

Giant dipole resonance

## ABSTRACT

This review paper concerns the research devoted to the study of the properties of dipole excitations in nuclei. The main focus is on questions related to isospin effects in these types of excitations. Particular attention is given to the experimental and theoretical efforts made to understand the nature and the specific structure of the low-lying dipole states known as the Pygmy Dipole Resonance (PDR). The main experimental methods employed in the study of the PDR are reviewed as well as the most interesting theoretical aspects. The main features of the experiments and of theoretical models are reported with special emphasis on the reaction cross sections populating the dipole states. Results are organized for nuclei according to different mass regions. The knowledge of the isovector dipole response as well as its low energy part is important in order to deduce the nuclear polarizability as accurate as possible. This issue is discussed in this paper together with the connection with the neutron skin and the nuclear equation of state. The important role played by the dipole response to deduce other physical quantities of general interest is discussed in the last two chapters. One concerns the level density and the other the isospin mixing in nuclei at finite temperature and its relation with beta decay.

© 2019 The Authors. Published by Elsevier B.V. This is an open access article under the CC BY license (<http://creativecommons.org/licenses/by/4.0/>).

## Contents

1. Introduction.....	361
2. Overview of the experimental methods.....	363
3. Overview of the total dipole response .....	370
3.1. Coulomb excitation by proton scattering .....	370
3.2. Nuclear resonance fluorescence for low-lying dipole states .....	375
4. Theoretical studies of low-lying isovector and isoscalar dipole states.....	384
4.1. Introductory overview.....	384
4.2. The dipole strength distribution.....	386
4.3. Isovector and isoscalar dipole transition densities.....	388
4.4. Nuclear form factor of the low lying dipole states .....	392
4.5. Collectivity of the low lying dipole states.....	394

\* Corresponding author at: Dipartimento di Fisica dell'Università degli Studi di Milano, Italy.

E-mail address: [Angela.Bracco@mi.infn.it](mailto:Angela.Bracco@mi.infn.it) (A. Bracco).

4.6. Isospin character of the low-lying dipole states from theory.....	396
5. The isospin character of low-lying dipole states from experiments .....	398
6. Results from experiments using isoscalar probes .....	398
6.1. The isospin character of dipole states in light nuclei (mass $\leq 30$ ) .....	398
6.2. The isospin character of dipole states in Ca isotopes .....	399
6.3. The isospin character of dipole states in nuclei in the mass region $\approx 70$ .....	402
6.4. The isospin character of dipole states in the mass region 90 .....	405
6.5. The isospin character of dipole states in the $^{124}\text{Sn}$ nucleus .....	407
6.6. The isospin character of dipole states in the semimagic N=82 nuclei $^{140}\text{Ce}$ nucleus .....	409
6.7. The isospin character of dipole states in the $^{208}\text{Pb}$ nucleus .....	413
7. The structure of pygmy states from beta decay studies .....	414
8. Further aspects .....	417
8.1. The dipole response and the nuclear level density .....	417
8.2. Isospin symmetry at finite temperature .....	420
9. Summary and conclusions .....	427
Acknowledgments .....	429
References .....	430

## 1. Introduction

Collective modes are among the most interesting and ubiquitous excitations along the entire Segré diagram. In particular, nuclear excitations corresponding to oscillations of dipole type, very much studied for several decades, are attracting nowadays special attention both from experimental and theoretical point of view. Indeed, extensive works focusing in particular on more exclusive results and more refined theoretical approaches were carried out recently. The rather recent wealth of information on these nuclear dipole states has motivated this review which is primarily concentrated on isospin aspects. Previous reviews are in [1,2] and [3].

It is well known that the electric dipole strength (E1) in nuclei is characterized by the presence of a broad resonance, the Giant Dipole Resonance (GDR). In addition, the presence of structures of rather small size at around and below the energy corresponding to the neutron separation energy was well identified. These structures are commonly denoted as Pygmy Dipole Resonance (PDR) states. Because of this more complex structure of the dipole nuclear response it became clear that it is very important to investigate with adequate sensitivity a broad energy region of nuclear excitation covering the response below and above the particle separation energies. In particular, the very interesting question concerning the microscopic nature of pygmy states is currently being addressed. A large fraction of this review paper is centered on results from experiments and theory concerning this question. According to the common picture, which conceives the GDR as an oscillation of all protons against all neutrons and the PDR as an oscillation of a neutron skin against an isospin symmetric core (see Fig. 1), these modes should be investigated via isovector and isoscalar probes that are sensitive to the isospin of the nucleons. For nuclei with different numbers of neutrons and protons, an isoscalar probe should be able to induce the excitation of the PDR states. Therefore we find in an ideal situation where a problem can be addressed with different means; a kind of multi-messenger investigation which has brought to light new features of this new mode. Indeed, experiments performed with different nuclear reactions like  $(\text{p}, \text{p}')$ ,  $(\gamma, \gamma')$ ,  $(\alpha, \alpha'\gamma)$  or  $(^{17}\text{O}, ^{17}\text{O}'\gamma)$  on stable nuclei and other on nuclei far from the stability line with inverse reactions on  $^{208}\text{Pb}$ ,  $^{nat}\text{Au}$  and  $^{12}\text{C}$ , have produced several data that provide some interesting answers to this problem. The selection of results here discussed is rather large and cover different mass regions. In fact, the first major issue was to investigate in a rather systematic way how general is the PDR in nuclei and the potential effects related to the closed shells, level density, number of neutrons (or protons) involved in the excitation among others. Therefore this paper is organized in subsections discussing the results in different mass regions. The importance for detailed investigations in the low energy region is manifold. The neutron-skin oscillation picture suggests a dependence of the dipole strength on the neutron skin. Some theoretical approaches ( e.g. Refs. [4–6]) show a connection to the symmetry term of the nuclear binding energy and the nuclear equation of state. However, other approaches employing a correlation analysis [7] conclude that there is only a marginal correlation between the low-lying E1 strength and these quantities. At present, the situation remains controversial but the strength in the PDR region cannot be neglected for precise determination of the nuclear polarizability (see discussion in the following sections). The presence of additional E1 strength near the neutron separation threshold has an impact on neutron capture rates in astrophysical processes (see e.g. Ref. [8]). The  $1^-$  levels forming the PDR have lifetimes in the lower femtosecond or even attosecond range. These levels, having a broad resonance width, act as wide open doorway states in the neutron-capture process. Additionally, the short lifetimes, close to typical neutron evaporation times, permit a fast depopulation of the capture levels to lower-lying bound states, which stabilizes the newly formed nucleus against subsequent neutron emission. According to the detailed balance, in the photon bath of an astrophysical r-process environment, the PDR levels above the threshold enhance the reverse process of photo-dissociation ( $\gamma, \text{n}$ ). Consequently, the astrophysical r-process that proceeds via neutron rich nuclei, is expected to be enhanced by the presence of an E1 strength around particle binding energy. In the r-process the neutron capture competes with gamma decay, which is of E1 type, and originates at excitation energy around the neutron binding energy. Therefore, the amount of E1 strength and its energy position

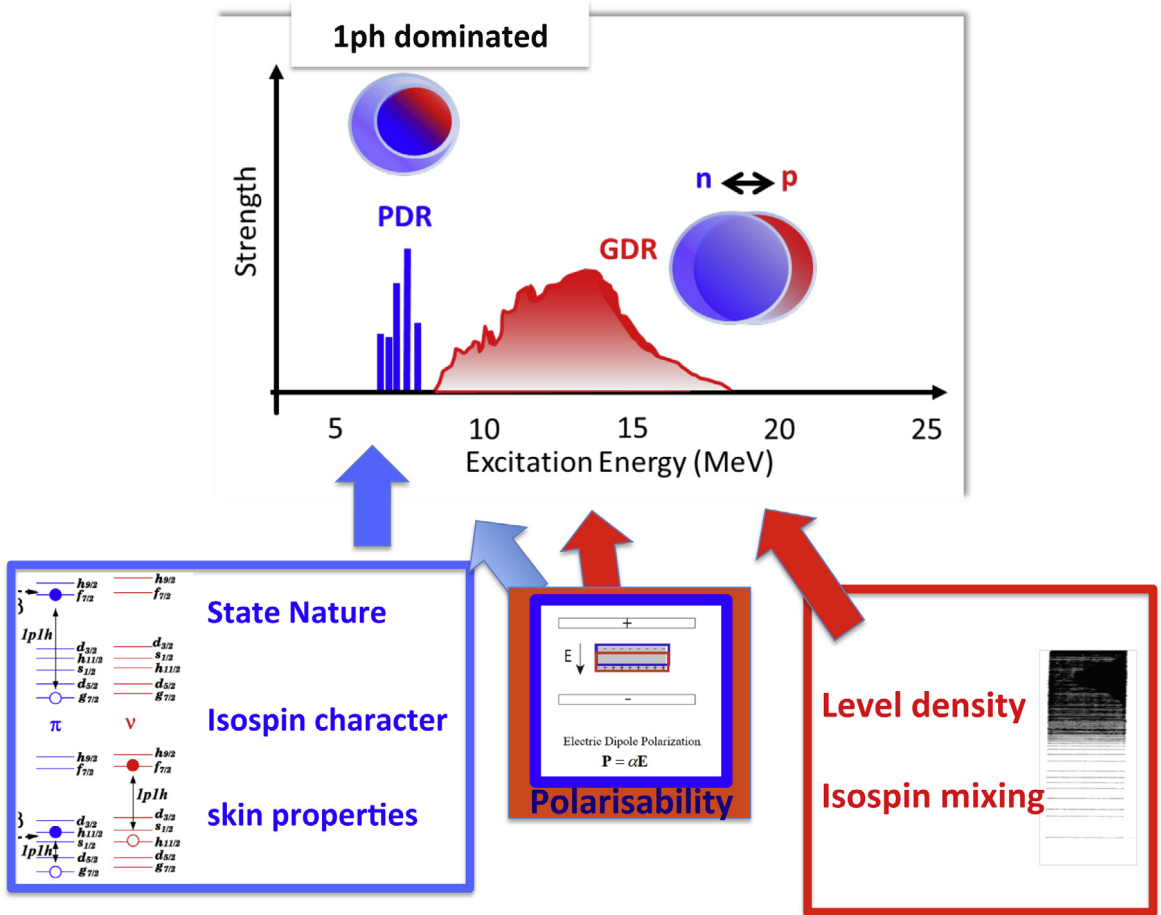


**Fig. 1.** Picture displaying schematically the electric dipole response of nuclei in which the Giant Dipole Resonance (GDR) is depicted as oscillation of all protons against all neutrons and the Pygmy Dipole Resonance (PDR) is depicted in neutron rich nuclei as a property of the neutron skin (neutron states of 1particle–1hole nature). In the three frames in the bottom part a simple illustration is given of the physical quantities addressed in this paper which are probed by the dipole response.

close to the energy of the neutron separation threshold is of paramount importance since it affects the abundances of elements formed via the r-process. Several models were developed to study the dipole response in nuclei. An important and common feature of the results (see Section 4 for their discussion) is that both at low and high energy there are dipole states having different isospin nature, namely of isoscalar and isovector characters. These predictions have stimulated a great deal of experimental efforts to identify and to characterize them. Concerning the isoscalar dipole state at excitation energy above the particle binding energy extensive experimental and theoretical work was made and the main results are reviewed in Ref. [9]. Indeed, in the high energy region the Isoscalar Giant Dipole Resonance (ISGDR) was found in a large number of nuclei and its centroid position was shown to be related to the nuclear compressibility providing information complementary to those obtained from the study of the Giant Monopole Resonance. On the other hand, the study the isoscalar dipole states at excitation energy around the particle binding energy is discussed in detail in this paper referring to experiments which measure not only the excitation cross section (as done in the high energy excitation region) but also the gamma decay from these states. In particular, for nuclei with neutron excess, these low-lying dipole states have been found to have a strong mixing of isoscalar and isovector character which makes these states a good laboratory for the study of the interplay between isoscalar and isovector modes. Within the extensive efforts made to deduce the nuclear structure properties of low-lying dipole states of particular relevance are the studies made using the beta decay. This method resulted to be very powerful although it has the draw-back of being selective to particular final states, due to the  $\beta$ -decay selection rules. In addition the amount of the Q-value in many cases is such that does not cover the entire region of the PDR.

Additionally, very interesting nuclear features that can be deduced using as a tool the giant dipole resonance are discussed in this review paper. They are: (i) the connection of the nuclear polarizability to the neutron skin and to the nuclear equation of state; (ii) the level density deduced from fine structures in the GDR; (iii) the isospin mixing and its connection with beta decay lifetimes. In Fig. 1 a schematic illustration of the subjects of this paper is given.

The paper is organized as follows: after a general overview in Section 2 of the experimental method used to investigate the low lying dipole states a more detailed description of Coulomb excitation by proton scattering and nuclear resonance fluorescence is presented in Section 3. The following Section 4 is dedicated to illustrate the theoretical studies regarding some of the most relevant aspects of the low-lying dipole states like the dipole strength distributions as well as the isovector and isoscalar transition densities which give important information about the low-lying dipole states. A subsection is dedicated to the radial form factors which are of paramount importance in the comparison between the experimental inelastic cross sections and the calculated ones for the PDR. Special attention is dedicated to the still unresolved question about the collectivity of the PDR and to the isospin content of the low-lying dipole states. This latter aspect is analyzed also from an experimental point of view in Section 5. In the next section, the use of isoscalar probes to study the isospin character of the dipole states is analyzed in more details for each mass region that has been investigated until now. The use of the beta decay which can improve the knowledge of the decay branchings of the PDR is illustrated in Section 7. Finally, the last Section 8 deals with two aspects apparently distant from the problem treated here but that have a strong relevance from the experimental point of view: the nuclear level density which can be inferred from the dipole response measuring the  $(p, p')$  cross section, and the isospin mixing deduced from the decay of the GDR at finite temperature. Due to the large use of acronyms in the paper, a list of them is provided in Table 2 at the end of the paper just before the bibliography.

## 2. Overview of the experimental methods

This section is intended to provide a brief overview of the experimental methods primarily used for the study of the electric dipole strengths in nuclei. The population mechanism and their decay modes (mostly, but not always detected) are summarized in Fig. 2. The main features, advantages and/or limitations are pointed out in a sketchy way below, while more details are given, when needed in connection with the discussion of the results.

### *The nuclear resonance fluorescence*

The nuclear resonance fluorescence (NRF) is the measurement technique, often called  $(\gamma, \gamma')$ , for which the target nuclei (denoted by  $A$  in Fig. 2) are irradiated by real photon beams. The target nucleus absorbs the photon in correspondence of specific states mainly with multipolarity 1 and 2 and this implies the formation of a resonance state, from which gamma-rays are emitted. Most work employing the NRF technique was done at energy below the particle separation energy and for the detection of the emitted  $\gamma$ -rays most of the time high-purity germanium (HPGe) detectors were employed (Fig. 2(a)–(c)). Concerning the NRF experiments it is important to point out that photon beams can be produced by two different methods giving in general a different energy resolution. One method uses the bremsstrahlung mechanism and the other employs the Laser Compton backward scattering (LCS) resulting from the collision of electron beams with a laser emitting mainly in the visible frequencies. In the former case (Fig. 2(a)), an electron beam and a radiator target are used for producing the “bremsstrahlung beam”. This beam has a continuous energy spectrum decreasing exponentially at higher energy. The photon intensity of the bremsstrahlung beams are usually higher than that obtained so far with LCS. The photon beam spectrum is known or calibrated but the photon energy is not known for each event. Therefore in usual analyses, it is assumed that the gamma-rays from the transition of the initially populated states to the ground states are observed by the detector. As a consequence the measured quantity is the product of the photo-absorption cross section and the branching ratio of the gamma-decay to the ground state and it neglects the feeding from higher lying state. The branching ratio and the feeding might be corrected by statistical decay simulations for reconstructing the spectrum of the photo-absorption cross sections. Improvements for the bremsstrahlung beams are obtained with the method of tagged-photon (Fig. 2(b)), consisting in the detection of coincidences between the energy of the electron that produced a photon by bremsstrahlung and gamma-rays emitted by the nucleus. In this way the photon beam energy is measured on the event by event basis from the energy difference between the beam and the detected electron. The typical energy resolution of the tagged-photon is 30 keV.

So far the LCS photon beam in the region of NRF (Fig. 2(b)) is produced by Compton scattering of laser photons scattered by accelerated electrons in a storage ring. Due to the high-energy of the electrons the photon energy is boosted to the energy region from MeV to several ten MeV that matches the NRF measurements. The photon beam is collimated at around the backward scattering angle close to  $180^\circ$  to have quasi-monoenergetic photons. The typical beam energy width is 3% (typical values at the H $\gamma$ S facility) [10]. The photon energy is tunable by adjusting the electron beam energy in the storage ring depending on the wavelength of the laser. Either conventional lasers or free-electron lasers are used for producing the laser beams. With the LCS technique the photon beam can be polarized close to 100% since the polarization of the laser beam is maintained in the Compton scattering process. A polarized photon beam is useful for identifying the parity of the resonance state. Pioneering work for the experimental determination of the parity of nuclear excited states in NRF measurements is in Ref. [11]. The ELI-NP facility [12,13] presently under construction and using a linear electron accelerator will provide intense polarized gamma beams with energy within a very narrow band.

Since the energy width or uncertainty of the photon beam is relatively small in the cases of the tagged-photon and the LCS, feeding effect from the states at higher excitation energies is negligibly small or can be corrected by using the data at higher photon-beam energies. The merit of this quasi-monoenergetic photon beam is exploited in the  $\gamma^3$  setup (Fig. 2(c)) [10] of the LCS photons at H $\gamma$ S. There, cascade decays are analyzed for the data in which the detector gamma-ray energy is different from the photon beam energy. Typically the ground decay from the several low-lying states are investigated but also  $\gamma$ - $\gamma$  coincidences events can be collected.

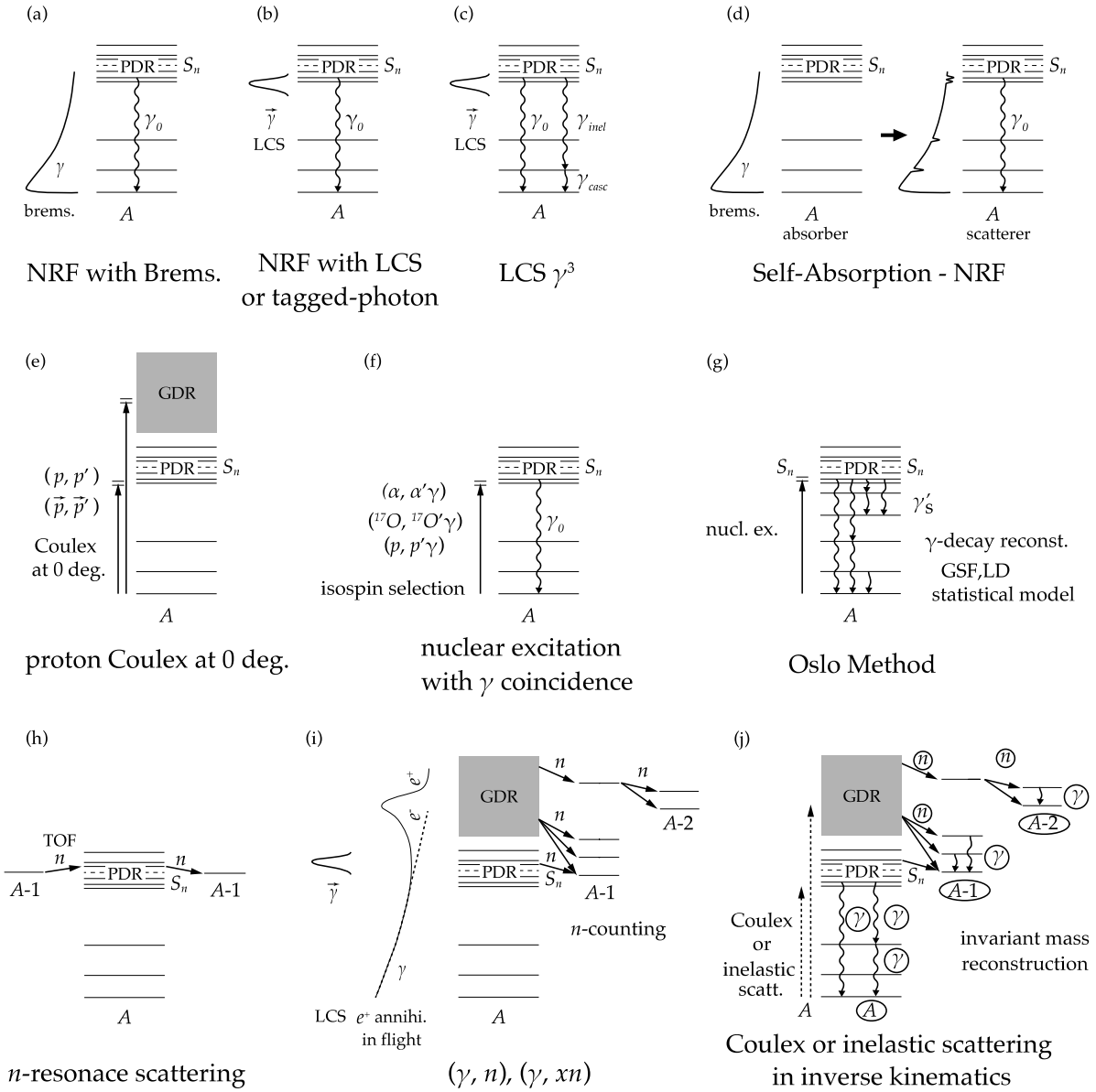


**Fig. 2.** Illustration of the major experimental methods used for the study of the electric dipole strengths and their decay modes.

A specific need of  $\gamma$  decay measurements with real-photons is the use of a large amount of target nuclei, typical of the order of grams, due to the limited intensity of the photon beams presently available. In addition the measurement is limited up to the neutron separation energy ( $S_n$ ) or just above it, since the neutron decay quickly dominates the decay branches that limits the statistics of the measurements of the gamma-decay channels. The newer generation facility for high-intensity LCS beams ELI-NP was designed to reduce those limitations [13]. In addition, since the well-separated individual photo-peaks of the gamma detectors are typically analyzed, unresolved small strengths in high level-density regions are unobserved. The effect is studied in a few cases by employing more advanced treatments for the data analysis.

#### The self-absorption method

The experiments performed using the self-absorption method (Fig. 2(d)) are essentially transmission type experiments which measure the reduction of photons in the absorber target to deduce the photo-absorption cross sections (see e.g. [14] and references therein). These measurements are often accompanied by another measurement using the NRF detection technique for the detection of individual photons after the absorber target which contains the same nuclides. The self-absorption measurement does not depend on the decay channels since the absorption, namely the excitation part of the target nucleus, is the origin of the reduction of the photon beam when passing in the absorber target. However, the

reduction of the photons by atomic processes needs to be corrected and this is done, for example, by using absorbers made of different isotopes or of different elements but with similar atomic number. The self-absorption measurements require significant amount of target material of the order of grams.

#### Coulomb excitation by proton scattering

The Coulomb excitation of dipole states by scattering of relativistic proton beams at very small angles (Fig. 2(e)) is a powerful method that was developed at the Research Center for Nuclear Physics, Osaka University [15], and was then also widely used at iThembaLABS [16]. Proton beams in the energy interval 300–400 MeV are used at RCNP while at iThemba LABS beams at 200 MeV are used.

The Coulomb excitation of electric dipole states dominates the total cross sections at scattering angles very close to zero degree while the nuclear excitation of the electric dipole states has its maximum at little larger angles, namely at of 2–5 degrees depending on the incident beam energy. Moreover, the grazing angle is also in the similar angular region of 2–3 degrees. Thus the realization of the measurement at zero degrees is essential if one wants to exploit the Coulomb excitation of dipole states and deduce the electric dipole strength. The experimental setups of the zero-degree measurement used for past measurements and also these days are shown in Fig. 3. There the schematic lay-outs of the magnetic spectrometers at RCNP and at iThemba Labs are given. The excitation energy and the cross section are measured only by detecting the scattered protons. It is important to point out that this type of measurements probes the excitation process independently from the possible decay channels. For the measurement of the scattered protons high energy-resolution spectrometers (resolution of  $\sim 20$  keV in the GDR region) are available in both facilities when the spectrometers are used in the dispersion matching mode. The contribution from the other multipolarities are separated out by applying the well established multipole decomposition analysis (MDA) technique of the angular distribution of the cross sections or by analyzing the polarization transfer information (PTA) [17,18]. The high resolution measurements at zero degree are, in general, sensitive to the full electric dipole strength including the small unresolved ones and can cover the excitation energies from  $\sim 5$  MeV up to the higher energy tail of GDR across the neutron separation energy. Another merit of this technique is that the required amount of the target material is of the order of 10 milligrams, a feature that makes much easier the preparation of isotopically enriched targets as compared with the case of the real-photon measurements, requiring instead targets of the order of grams. The high energy-resolution data enable the spectrum fluctuation analysis for extracting the level density up to the order of  $\sim 10^5$ /MeV. On the other hands, one needs to rely on the multipole separation as achieved by applying the MDA or the PTA method in particular for the experimental conditions at which the nuclear interaction also plays a role. The uncertainty of MDA is estimated typically to be approximately  $\sim 5\%$  [18]. The PTA analysis is instead usually dominated by the statistical uncertainties.

#### Inelastic scattering and gamma-decay

The measurements using inelastic scattering and gamma-decay have been extensively made in recent years to study the excitation of dipole states via nuclear interaction and to learn on their isospin character (Fig. 2(f)). The used excitation reactions,  $(\alpha, \alpha'\gamma)$  [1,19–23],  $(^{17}\text{O}, ^{17}\text{O}'\gamma)$  [24–29], and  $(p, p'\gamma)$  [30] have indicated that in the energy region of 4–7 MeV dipole states have predominantly isoscalar character (see e.g. [1] and [24]). In addition, it should be pointed out that, in contrast with the Coulomb excitation methods, the  $\alpha$  and  $^{17}\text{O}$  reactions, due to their strong absorption property in the target nuclei, dominantly probe the surface of the nucleus. Therefore with these reactions information on the transition strengths could be deduced. The spin-parity of the individual excited states is typically identified by the energy of the excited states exploiting the high energy resolution of the HPGe detectors and the information of known transitions obtained by NRF measurements. The excitation energy and the gamma-decay energies are matched to select the ground-state gamma-decay events excluding the cascade decays and possible background processes. More details on this method are given in Section 5 in conjunction with the discussion of the obtained results which are the main core of this review paper. Particular emphasis is given to the determination of the strengths which requires precise reaction-model calculations.

#### Inelastic scattering of alpha particles and $\gamma$ -decay

Several experimental results for the  $(\alpha, \alpha'\gamma)$  reaction are associated to an incident beam energy of 136 MeV and were obtained with the beam produced by the AGOR cyclotron of the KVI laboratory. The scattered  $\alpha$  particles were detected with the BIGBITE magnetic spectrometer denoted as BBS(QQD-type). It has a large angular acceptance of up to 13 msr and a K value of 430 MeV and provides the possibility of measuring at scattering angles close to  $0^\circ$ . The light-ion detection system includes two vertical drift chambers (VDCs) and two scintillator planes. The signals of the latter are used for the  $\alpha$ -trigger decision. To determine the position and angles of the scattered  $\alpha$  particles in the focal plane the intersection points in the two VDCs are used. This allows the calculation of scattering angle and energy of the scattered  $\alpha$  particles. The detection of the coincident  $\gamma$ -ray emission was performed with seven HPGe detectors, positioned with an entrance window distance of about 23 cm to the target. With respect to the beam axis the detectors were located at angles between  $90^\circ$  and  $150^\circ$  in the horizontal plane. Each detector has a relative efficiency of about 100% (at  $E_\gamma = 1.33$  MeV) compared to the NaI standard detector. Four detectors were surrounded with bismuth germanate (BGO) shields for active background suppression. The total photopeak efficiency of the array is determined with different radioactive sources with known activities and is about 0.45% at  $E_\gamma = 1.33$  MeV and 0.15% at  $E_\gamma = 6.0$  MeV. The efficiencies of the single detectors to energies of up to 9 MeV were deduced from GEANT simulations. The suppression of background events is another important issue in these experiments. Because the cross section for elastic scattering at forward scattering angles

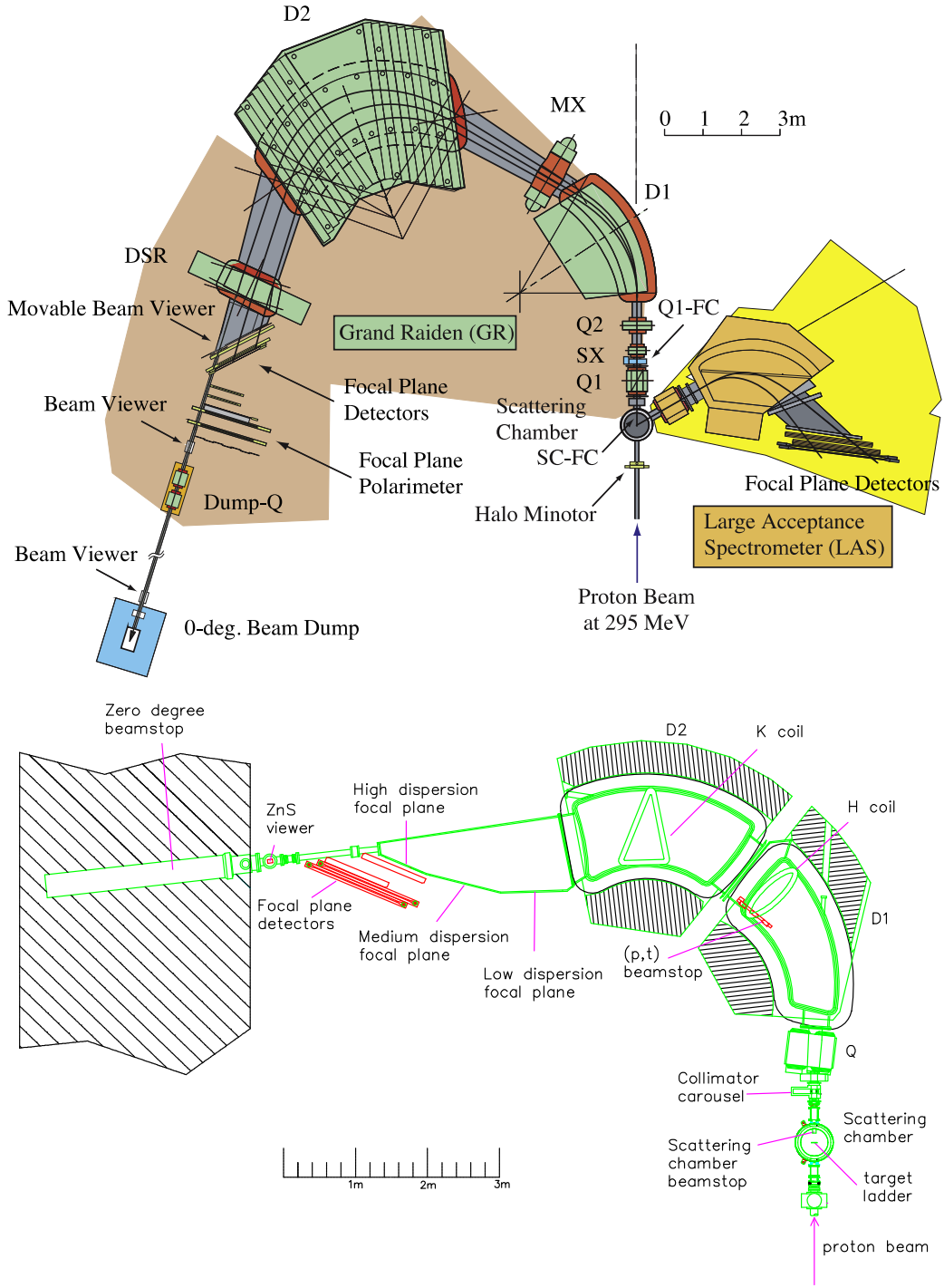


**Fig. 3.** The experimental setup of the Coulomb excitation by proton scattering at zero degrees with (upper panel) the high-resolution spectrometer Grand Raiden at RCNP [17] and (lower panel) the K600 spectrometer at iThemba LABS [16]. The beam passed through the target is transported in the spectrometer and is stopped in the beam dump after passing through the focal plane. Only the inelastically scattered protons are detected by the focal plane detectors.

is several orders of magnitude higher compared to inelastic scattering, the elastically scattered  $\alpha$  particles were blocked an aluminum plate in front of the first entrance detector. This reduces significantly the count rates due to elastic scattering and random coincidences. Due to used constraints, the energy resolution of the scattered  $\alpha$  particles was limited to about

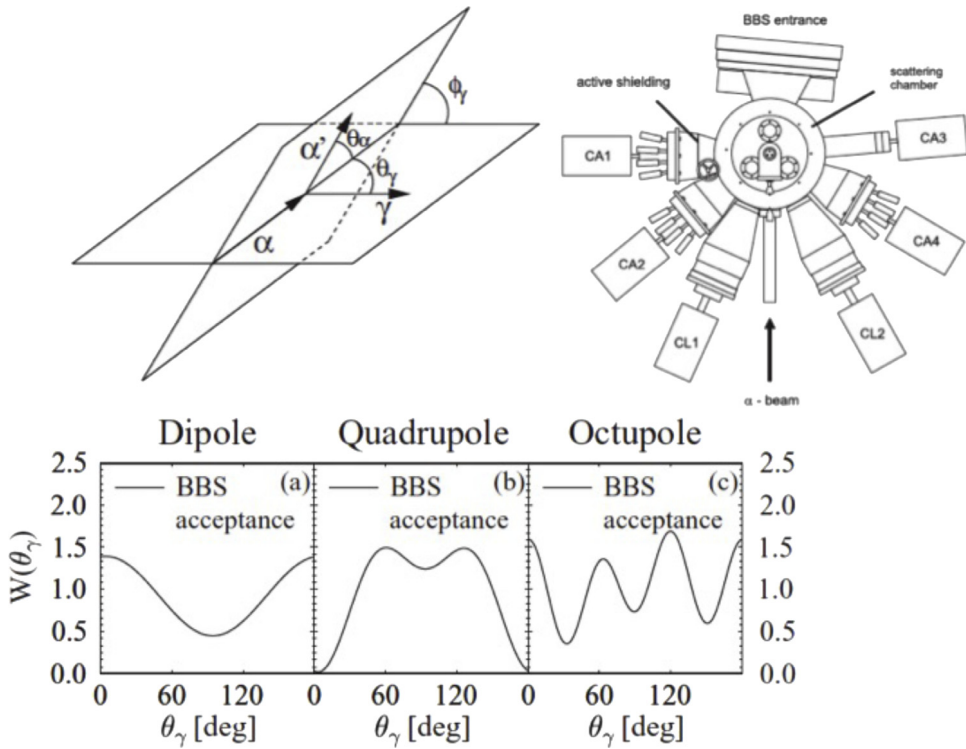


**Fig. 4.** The schematic of the set up used at the KVI laboratory for measurements of the  $(\alpha, \alpha'\gamma)$  reaction on various nuclei. The angular correlation signature taking into account the acceptance of the spectrometer can be seen in the bottom panels of the figure.  
Source: Adapted from [21].

200 keV. The high energy resolution of the germanium detectors can be kept at about 9 keV FWHM at  $E_\gamma = 5.5$  MeV in the region of interest. A schematic of the experimental arrangement is shown in Fig. 4 and the description of the technical details can be found in Ref. [31]. Depending on the angle of the germanium detector, the  $\alpha$ - $\gamma$  angular correlation produces different relative intensities for transitions of different multipolarities. This angular correlation, shown in Fig. 4, was calculated taking into account the m-state population amplitudes resulted from DWBA calculations and the acceptance of the spectrometer. To be noted that the  $\alpha$ - $\gamma$  angular correlation  $W(\Omega_\gamma)$  is also needed to determine the single  $\alpha$ -scattering cross section from the double-differential cross section. The relation is given by,

$$\frac{d\sigma^2}{d\Omega_\alpha d\Omega_\gamma} = \frac{1}{4\pi} \frac{\Gamma_0}{\Gamma} W(\Omega_\gamma) \frac{d\sigma}{d\Omega_\alpha} \quad (1)$$

where the branching ratio  $\Gamma_0/\Gamma$  refers to  $\gamma$  decay to the ground state and  $d\Omega_\alpha$   $d\Omega_\gamma$  are the solid angles for the detection of  $\alpha$  particles and  $\gamma$ -rays, respectively.

#### Inelastic scattering of $^{17}\text{O}$ and $\gamma$ -decay

For the experiments made using the  $^{17}\text{O}$  beam a set up consisting of Ge detectors and Si telescopes was used. The beam energy was 20 MeV/u. From the experimental point of view the use of  $^{17}\text{O}$  is preferable as compared with the most abundant isotope  $^{16}\text{O}$  (purer as isoscalar probe) because of its rather small neutron binding energy (4.1 MeV). In fact, for measurements using heavy ions as beam particles one has to deal with the excitation of both target and projectile and the separation of the two contributions is needed. The value of separation energy of 4.1 MeV in  $^{17}\text{O}$  assures that the  $\gamma$ -rays emitted in the region of interest 4–8 MeV originate from the target excitation since  $^{17}\text{O}$  is measured in coincidence.

In contrast with light ions, for  $^{17}\text{O}$  the pattern of the differential cross section for inelastic scattering as a function of the angles does not characterize well the multipolarity of the excited states. The measurements discussed in this paper were made around the grazing angle  $9.31^\circ$  ( $^{90}\text{Zr}$  target),  $10.72^\circ$  ( $^{124}\text{Sn}$  target),  $16.01^\circ$  ( $^{208}\text{Pb}$  target). With heavy ion beams, states with different multipolarity, also larger than 3, can be populated. However, the gamma decay selection rules suppress the decay to ground state for such high spin states. An important point is the measurement of the angular distribution of the emitted gamma-rays reflecting the spin of the populated states.

The set up for the  $(^{17}\text{O}, ^{17}\text{O}'\gamma)$  measurements consisted of two main detection systems, one for the measurement of the scattered ions and one for the measurement of the gamma decay. Fig. 5 shows in a schematic way the experimental set up. A system of telescopes of Si detectors was used for the identification and measurement of the kinetic energy

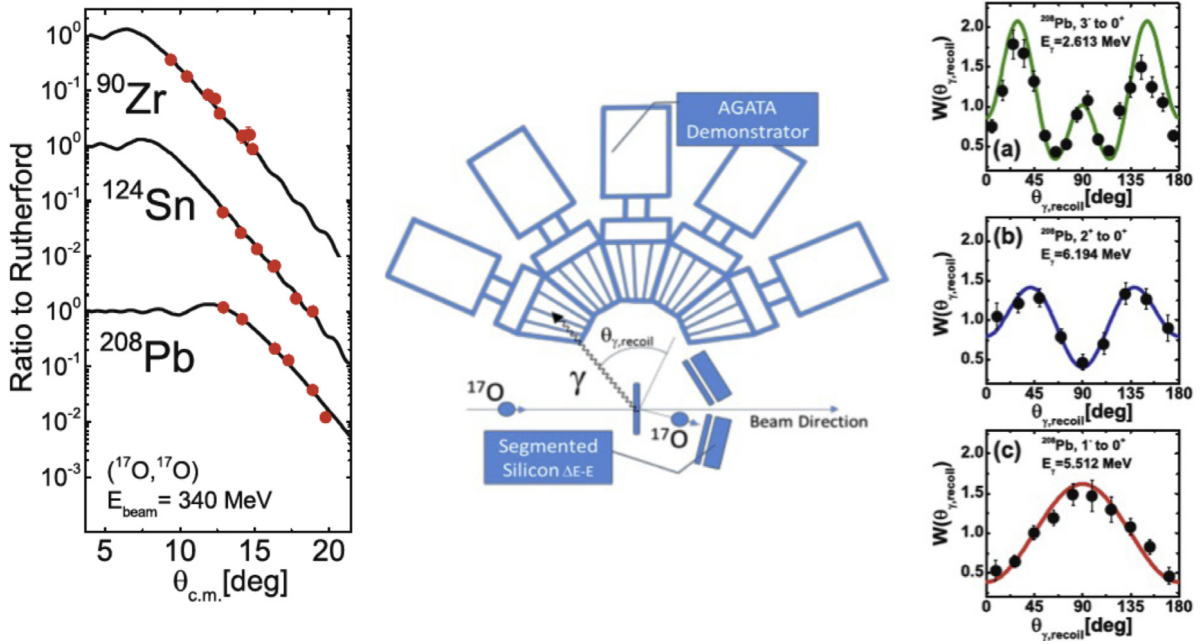


**Fig. 5.** The schematic of the set up used at the LNL INFN laboratory for measurements of the  $(^{17}\text{O}, ^{17}\text{O}'\gamma)$  reaction on various nuclei. The angular distribution of the  $\gamma$ -rays and the elastic scattering used to deduce the parameters of the optical potential are also shown.  
Source: Adapted from [24].

of the scattered ions. The segmented silicon telescopes (pixel type) were placed for each measured nucleus at around the grazing angle and symmetrically with respect to the beam direction. These telescopes are prototypes built for the TRACE project [32]. Each Si detector had an horizontal size of 20 mm, a vertical size of 50 mm and included 60 pixels each with an area of 4 mm  $\times$  4 mm. The front face surfaces formed approximately a disk in the plane perpendicular to the beam at a distance of 8 cm from the target center. The two  $\Delta E$ - $E$  silicon telescopes each consisted of a thin “ $\Delta E$ ” detector placed in front of a thick “ $E$ ” detector, the first giving an energy loss of about 70 MeV for  $^{17}\text{O}$  ions at 340 MeV and the second stopping the  $^{17}\text{O}$  ions completely. The thresholds of the Si detectors were such that a large fraction of events corresponding to protons and alpha particles were rejected. The overall energy resolution (as FWHM) was typically around 0.3% at 340 MeV.

The detection of gamma rays, emitted in coincidence with events measured in the Si telescopes, was performed with the AGATA (Advanced Gamma Tracking Array) Demonstrator. AGATA is a HPGe detector array of new generation allowing to use the techniques of pulse shape analysis and of gamma-ray tracking [33,34]. At the time of this experiment the AGATA Demonstrator consisted of three to five triple clusters of HPGe detectors and was placed 13.5 cm from the target covering an angular range in theta from 100° to 150° (relative to the beam direction). The segmentation of the HPGe detectors allowed the direction of the gamma-ray emission to be determined with a precision of 1 degree. The AGATA detection efficiency was deduced from measurements with radioactive gamma sources and by simulations performed with the computer code GEANT4 [35] including the geometrical configuration of these particular experiments.

To obtain the excitation cross section for specific nuclear states data from  $(^{17}\text{O}, ^{17}\text{O}'\gamma)$  were used. Indeed, if one measures, in addition to the energy transferred from the projectile to the target, the gamma-decay from the state with HPGe detectors the energy resolution is much improved and more states are in general identified. This requires the measurement of all the possible decay branches when the decay from an excited state does not involve only the direct decay to the ground state. In addition, since the yields were extracted from spectra for which the condition  $E^* = E_\gamma$  within a window of approximately  $\pm 1$  MeV, possible feeding was evaluated by shifting the gates at higher energy. The error bars in the experimental points include all these corrections, in general rather small and mainly concerning the region below 3 MeV.

Because of the feature of the set up used for the  $(^{17}\text{O}, ^{17}\text{O}'\gamma)$  reaction measurements, it was possible to obtain, for the most intense transition, an almost continuous angular distribution of the emitted gamma-rays relative to the direction of the recoiling nucleus. The direction of the recoiling nucleus was deduced from kinematics from the measured scattered particles. To give few examples the measured double differential cross section is shown in Fig. 5 for three excited states in  $^{208}\text{Pb}$ .

In addition to the cross section for excited states also the elastic cross section was measured with this set up and this allowed to deduce the parameter of the optical model, information needed for the analysis of the cross section of the

different excited states. In Fig. 5 the elastic scattering data for the  $^{90}\text{Zr}$ ,  $^{124}\text{Sn}$  and  $^{208}\text{Pb}$  are shown. From that figure one can see that the ratio of the measured cross section with that of Rutherford is well reproduced by calculations [24].

#### *Inelastic scattering of unstable nuclei on He and C targets and $\gamma$ -decay*

The experiments performed in inverse kinematics to measure the gamma-decay from E1 states populated either by Coulomb excitation or by scattering from a  $^4\text{He}$  target have so far been performed using radioactive beams generated from fragmentation reactions. The latest works were performed at the RIKEN laboratory and at LNS-INFN Catania and thus here we present in brief the main features of these two setups.

At the Radioactive Isotope Beam Factory (RIBF), operated by RIKEN Nishina Center, primary beams, accelerated up to an energy of 345 MeV/A (with an average intensity of 250 particle nA in case of  $^{48}\text{Ca}$  as for the  $^{20}\text{O}$  experiment), impinge on a 15-mm-thick beryllium target to produce secondary beams via a projectile fragmentation reaction. The secondary beams are analyzed and identified event-by-event by the fragment separator BigRIPS, using the TOF- $\Delta E$ - $B\rho$  method [36]. The reaction products were analyzed by the ZeroDegree spectrometer [36] using the same TOF- $B\rho$   $\Delta E$  method. Decay  $\gamma$ -rays from the reaction products are detected by a large-volume  $\text{LaBr}_3:\text{Ce}$  scintillator array [37] located at a laboratory angle of  $30^\circ$ . The energy resolution in FWHM was 1.60% at 6.31 MeV with a source at rest. The efficiency was 0.90% for the full-energy peak of 1.84-MeV 3rays emitted from a  $^{88}\text{Y}$  calibration source. The efficiency was reproduced within 2.0% precision by a Monte Carlo simulation code built with the code GEANT4.

In the experiment performed at LNS-Catania medium mass primary beams, accelerated up to an energy of 40 AMeV using the Superconducting Cyclotron (CS), impinge on a 250  $\mu\text{m}$  thick  $^9\text{Be}$  target to produce, with a projectile fragmentation reaction, the  $^{68}\text{Ni}$  beam, delivered via the FRIBs@LNS fragment separator of the INFN-LNS (see [38] and references therein). In such a facility, a tagging system was used in order to characterize the cocktail beam event by event [39]. A large surface Micro-Channel Plate (MCP) gives the start of the Time of Flight (ToF) measurement of the beam. The stop of the ToF is delivered by a Double-Sided Silicon Strip Detector (DSSSD), with  $32 \times 32$  strips 2 mm width, and 156  $\mu\text{m}$  thick, placed at about 12.9 m from the MCP, along the transport beam line, approximately 2 m before the reaction target. The DSSSD provides also the energy loss information for the identification with the method  $\Delta E$ ToF and produces also the first information on the beam position to measure the trajectory. The second position information is given by a Parallel Plate Avalanche Counter (PPAC) detector, mounted at about 80 cm from the target, and having 1 mm spatial resolution. The inelastically scattered particles are measured in Si-CsI(Tl) telescopes [39].

To obtain energy resolution for the measurement of gamma transitions of the same order of those obtained with direct kinematics, where the emitting nucleus is almost at rest, one needs to have segmentation also in the detectors and therefore arrays such as AGATA or GRETA will be ideal for future studies in unstable nuclei. This is the only way one has because the energy resolution in inverse kinematic measurements is dominated by the uncertainty in the Doppler correction.

#### *The Oslo method*

This method was developed in Oslo to deduce the gamma strength function (GSF) (strongly affected by the E1 dipole response) and the level density (Fig. 2(g), [40] and references therein) for excitation energy up to the particle separation energy. It was applied to several nuclei in different mass regions.

Excited nuclear states are populated by nuclear reactions, either transfer or inelastic scattering, at low bombarding energy (15–20 MeV). The emitted gamma-rays are measured with a tag on the initial excitation energies. Difference spectra are constructed and used with the purpose to extract simultaneously the dipole transition probability and the density of nuclear states. The overall gamma spectra corresponding to different bins in excitation energies are reconstructed by using the statistical decay model and this allows to determine phenomenologically the gamma-ray strength function at excitation up to the particle separation energy. The gamma-ray strength function is assumed to represent the transition strength between the states with the fixed multipolarity (usually electric dipole) that depends on the target nuclei and the transition energy but not on the internal structure of the individual states (generalized Brink-Axel hypothesis [2,41,42]). The nuclear level density is calculated theoretically or determined phenomenologically as an additional fitting function.

This technique has allowed to identify the presence of small deviations from the expected tail of the Lorentzian shape in the region 3–7 MeV in several nuclei.

#### *The neutron resonance scattering*

The neutron resonance scattering experiments (Fig. 2(h)) were systematically performed for the nuclear application purposes. Especially the lower-energy neutron resonance scattering has very good energy resolution of the order of eV measured by the neutron time of flight. Thus the nuclear level densities are measured precisely by counting the number of the individual states at the neutron separation energy.

The electric dipole response in the GDR energy region was extensively studied by ( $\gamma$ ,  $xn$ ) measurements (Fig. 2(i)) in 1970's [43,44], where  $x$  denotes the number of detected neutrons. The gamma-ray beams were produced by the positron annihilation in flight method [43]. The low energy tail of the beam produced by the bremsstrahlung and atomic processes were subtracted with the spectrum taken with an electron beam for extracting the response to quasi-monoenergetic gamma beam. The number of emitted neutrons was measured after thermalization without detecting their energies. Consequently, ( $\gamma$ ,  $n$ ), ( $\gamma$ ,  $2n$ ), ( $\gamma$ ,  $3n$ ) cross sections were measured as a function of the gamma beam energy. The summed cross sections essentially represent the electric dipole response of nuclei above the neutron separation energy since

the electric dipole excitation is the dominant excitation process by the gamma-beam and the neutron emission is the dominant decay process. To be noted that there is a systematic difference in the cross sections between the data from the two major facilities of Lawrence Livermore and Saclay. The typical energy resolution was 500 keV. Several measurements using similar techniques were performed using the quasi-monoenergetic gamma-beam by LCS at the laboratories AIST, New-Subaru, and HI $\gamma$ S.

#### *Coulomb excitation and inelastic scattering in inverse kinematics*

The Coulomb excitation in inverse kinematics is the technique used at Radioactive Ion beam facilities (GSI and RIKEN) when using beam of few hundred MeV/A to study dipole excitations in unstable nuclei [45–47]. The beam nuclei produced with fragmentation technique hit a heavy nucleus target, like lead or gold, and are excited by Coulomb interaction. The emitted gamma-rays and neutrons are detected as well as the residual nuclei. In the case of neutron dissociation the initial excitation energy is reconstructed from the detected particles and gamma by the invariant mass method. This is a powerful method for studying the electric dipole excitation with low-intensity secondary RI beams at energy above the separation energy. It requires a large coverage of the solid angle and a large efficiency of the detectors for the emitted neutron and  $\gamma$ -rays, and thus the measurement at higher excitation energies is more difficult due to the increase of the open channels. The typical energy resolution is 1 MeV.

Measurements were also made using the inelastic scattering method at zero degree (dominated by Coulomb interaction) and detecting the emitted  $\gamma$ -rays in coincidence to investigate the details of the response function at energies around the binding energy.

#### *Gamma decays from GDR from fusion evaporation*

Measurements of the high energy  $\gamma$ -decay of the GDR from fusion evaporation reactions (induced by collisions of ions leading to compound nuclei) were carried out extensively to investigate nuclear shapes and their fluctuations, viscosity in fission ([2,48] and references therein). In addition, as discussed in Section 8.2, the  $\gamma$ -decay of the GDR was used to investigate the effects of the isospin mixing induced by the Coulomb interaction. General stringent experimental requirements for these studies are detection systems allowing efficient measurement of high energy  $\gamma$ -rays, the  $\gamma$ -neutron separation, and providing information of the excitation and decay processes of compound nuclei by measuring quantities such as multiplicity of the  $\gamma$ -rays, the emitted particles and low energy  $\gamma$ -rays from residual nuclei. This information is used in order to control in the best possible way the parameters entering in the statistical model calculations, needed to analyze the data and to deduce the GDR strength from the high energy  $\gamma$ -ray spectra.

### **3. Overview of the total dipole response**

#### *3.1. Coulomb excitation by proton scattering*

The electric dipole response of nuclei has been extensively studied by NRF below the neutron separation energy and by ( $\gamma$ ,  $xn$ ) above it. Here,  $x$  denotes the number of detected neutrons with its typical value in the interval 1–3. In particular, the systematic data were taken for a broad range of stable nuclei from helium to uranium isotope by the ( $\gamma$ ,  $xn$ ) measurements [43,44].

A new experimental approach, namely that of proton scattering measurement at extreme forward angles including zero degree, brought a break-through for the determination of the total electric dipole response [15,16]. One of the features of the measurement is that only the excitation part is probed by detecting the inelastically scattered protons, and thus it probes the full excitation strengths for all the decay channels. This is in contrast with experiments using the NRF technique or the ( $\gamma$ ,  $xn$ ) reaction, with which partial strengths of each decay channel are measured. At the laboratory RCNP, the measurements cover the excitation energy interval from low energy,  $\sim$ 5 (7) MeV, to high excitation energy up to  $\sim$ 23 (32) MeV at the incident proton energy of 295 (392) MeV. Therefore the measured cross section is for an excitation energy region across the neutron separation energy and reaches the higher energy tail of the GDR, with the exception of the case of light nuclei.

Electric dipole excitation by Coulomb interaction has the strong maximum and dominates the cross section at the scattering angle of zero degrees.

The spin-M1 excitation by nuclear interaction contributes to a smaller extent. The dominance of the electric dipole excitation in the cross sections was experimentally demonstrated by polarization transfer data (Fig. 6) as well as with the multipole decomposition analysis of the angular distribution of the cross sections. The separation of the electric dipole and the spin-magnetic dipole strengths in the PDR energy region of  $^{208}\text{Pb}$  is reported in more detail in Ref. [18]. The angular distribution of the proton inelastic scattering is predicted to be dependent on the shape of the transition densities between GDR and PDR calculated by the quasi-particle–phonon model (QPM) at around the forward angles of 0–5 degrees through the difference of Coulomb nuclear interference. The electric dipole strengths below 8.23 MeV have a chi-square fit for the PDR transition density consistently superior to the one with the GDR transition density, while the opposite is observed at higher energies. The finding implicates the sensitivity of the proton scattering data to the internal structure of the electric dipole strengths.

The measured differential cross sections at the most forward angular cut (typically 0.4° on the average in the solid angle) were converted to the reduced transition strength  $B(E1)$  by using the semi-classical theory of Coulomb

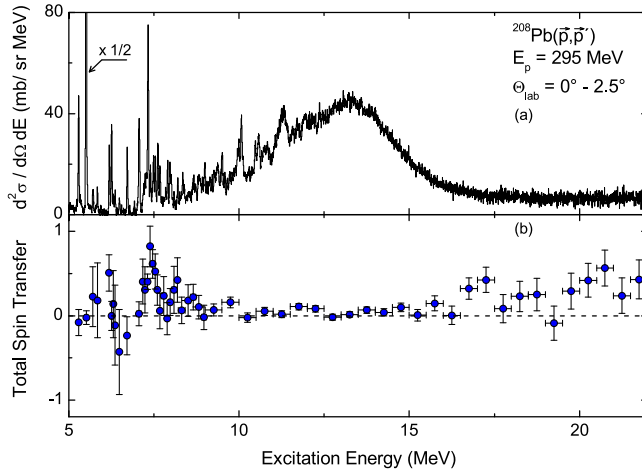


**Fig. 6.** (a) Spectrum of the  $^{208}\text{Pb}(p, p')$  reaction at  $E_p = 295$  MeV with the spectrometer placed at 0 degree. (b) Total spin transfer representing the ratio of the non-spin-flip part to the total cross sections.

Source: The figure was taken from [17].

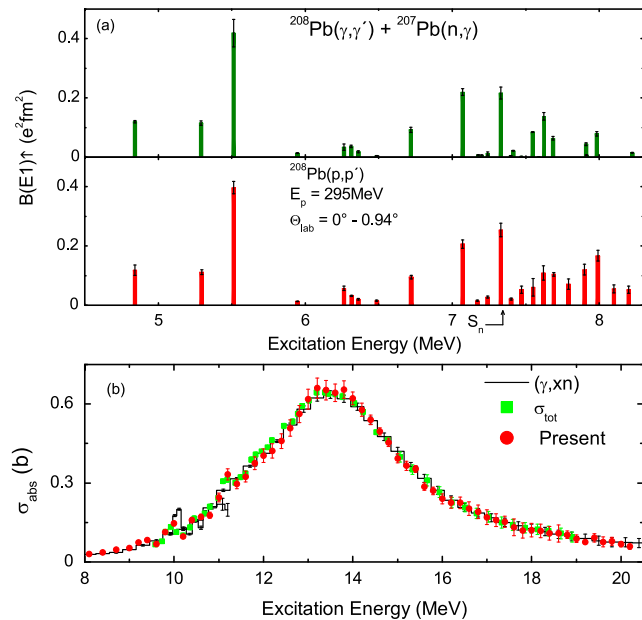


**Fig. 7.** (a)  $B(E1)$  strengths in  $^{208}\text{Pb}$  in the energy region  $E_x = 4.8–8.2$  MeV as deduced in Ref. [17] in comparison with  $(\gamma, \gamma')$  and  $(n, \gamma)$  experiments (references 26 and 29–31 in [17]). (b) Photoabsorption cross sections in the GDR region from the work [17] (shown as present) compared to  $(\gamma, xn)$  and total photoabsorption (references 33 in [17]) measurements.

Source: The figures were taken from [17].

excitation [49] or by eikonal theory [50]. The extracted electric dipole strengths in  $^{208}\text{Pb}$  by the MDA are shown to be in the remarkable agreement with the other experimental data where the data exist (Fig. 7). The high energy-resolution of 20–30 keV for the proton detection helps the identification of each discrete state and of the fluctuation of the strengths giving rise to the presence of fine structures superimposed to the broad GDR resonance structure. The decomposition analyses of the measured cross sections include the contribution of unresolved strengths that may correspond to a significant part of the strength not identified in the analysis of NRF data (see the discussion in Section 3.2). This aspect was pointed out in the case of the  $^{120}\text{Sn}$  nucleus. The data obtained for this nucleus are shown in Fig. 8. Indeed it was found that the  $B(E1)$  strength distribution determined by the MDA of the  $^{120}\text{Sn}(p, p')$  data is significantly larger than the one by NRF data, even if the cascade decays are corrected by a statistical model calculation. The disagreement is especially sizable at the excitation energy larger than 6.5 MeV. This finding from the  $(p, p')$  data shows the importance of the contribution from the unresolved strengths that are not always well accounted in the NRF data.

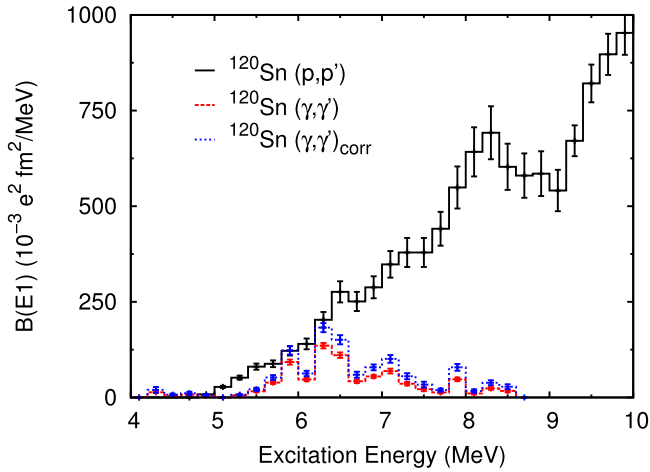


**Fig. 8.**  $B(E1)$  strength distribution in  $^{120}\text{Sn}$  determined by the multipole decomposition analysis of the  $^{120}\text{Sn}(p, p')$  data in comparison with the  $(\gamma, \gamma')$  data without and with the correction of the cascade decays with a statistical model analysis.  
Source: The figure was taken from [54].

Experiments on the Coulomb excitation by high energy proton scattering at zero degree were performed for the representative nuclei  $^{208}\text{Pb}$  [17],  $^{120}\text{Sn}$  [51],  $^{96}\text{Mo}$  [52], and  $^{48}\text{Ca}$  [53] for which the full electric-dipole strength-distribution was deduced. The low-energy electric dipole strengths were extracted for  $^{208}\text{Pb}$  [18],  $^{120}\text{Sn}$  [54], and  $^{90}\text{Zr}$  [55]. The GDR line shape in the region of deformed nuclei was also extracted [56].

From the determined full-strength distributions, sum-rules were verified. For that purpose the used equations follow the approach of Ref. [43] using the photo-absorption cross sections, related to the  $B(E1)$ . The cross section integrated over the whole energy interval from 0 to infinity is equal to the energy weighted sum-rule for the electric dipole operator, or to the Thomas-Reiche-Kuhn (TRK) sum-rule

$$\int_0^\infty \sigma(E)dE = \frac{2\pi^2 e^2 \hbar}{Mc} \frac{NZ}{A} = 60 \frac{NZ}{A} \text{ MeV mb}, \quad (2)$$

and the inversely energy weighted sum-rule or the nuclear polarizability sum-rule

$$\alpha_D = \int_0^\infty \frac{\sigma(E)}{E^2} dE \quad (3)$$

In addition, the static electric dipole polarizability (EDP), ( $\alpha_D$ ), can be extracted by using the polarizability sum-rule. The EDP in heavy nuclei is predicted to be sensitive to isovector properties of the nuclear system, especially to the symmetry energy of the nuclear equation of state at around the saturation density and to the neutron skin thickness [7,57,58]. The EDP is much more sensitive to the amount of the low-lying dipole strengths than the TRK sum-rule due to the inverse energy weight. Also as shown in Fig. 9 the EDP tends to converge well at around the higher energy tail of the GDR, in contrast to the continuous increase of the TRK sum-rule, that makes possible the experimental determination of the sum-rule value.

The electric dipole transition strength in  $^{208}\text{Pb}$  is plotted as a function of the excitation energy in a log scale in Fig. 10. The area in the figure is proportional to the relative contribution to the electric dipole polarizability. As it can be seen from the figure, the relative contribution at the low energy is enhanced and the contribution above  $\sim 35$  MeV is negligible. The strength starting from around 40 MeV and peaking at 60 MeV is considered to be the quasi-deuteron excitations, that represents the photon-absorption by the correlated proton-neutron pairs in the target nucleus. The quasi-deuteron strength was analyzed systematically [59,60], and later with a context of  $p$ - $n$  contact [61]. The relative contribution of the quasi-deuteron excitation to the electric dipole polarizability is rather small.

The electric dipole polarizability of  $^{208}\text{Pb}$  was deduced by integrating Eq. (3) using data up to excitation energy of 23 MeV from proton scattering together with the other experimental data [62,63] covering the region from 23 MeV up to 130 MeV. The dipole polarizability was found to be  $\alpha_D(^{208}\text{Pb}) = 20.1 \pm 0.6 \text{ fm}^3$ .

A strong correlation between the electric dipole polarizability and the neutron skin thickness is predicted for heavy nuclei, e.g.  $^{208}\text{Pb}$ . P.-G. Reinhard and W. Nazarewicz [7] found this correlation in  $^{208}\text{Pb}$  using the self-consistent mean-field theory in the nuclear energy density functional (EDF) formulation employing the Skyrme functional SV-min. The comparison of the measured dipole polarizability with this correlation provides an estimate of the neutron skin thickness which resulted to be  $\delta R_{np} = 0.156^{+0.025}_{-0.021}(^{208}\text{Pb}) \text{ fm}$  [17]. The determination of the neutron-skin thickness from the electric dipole polarizability data was further discussed in other theoretical calculations using various sets of effective interactions [57,58].

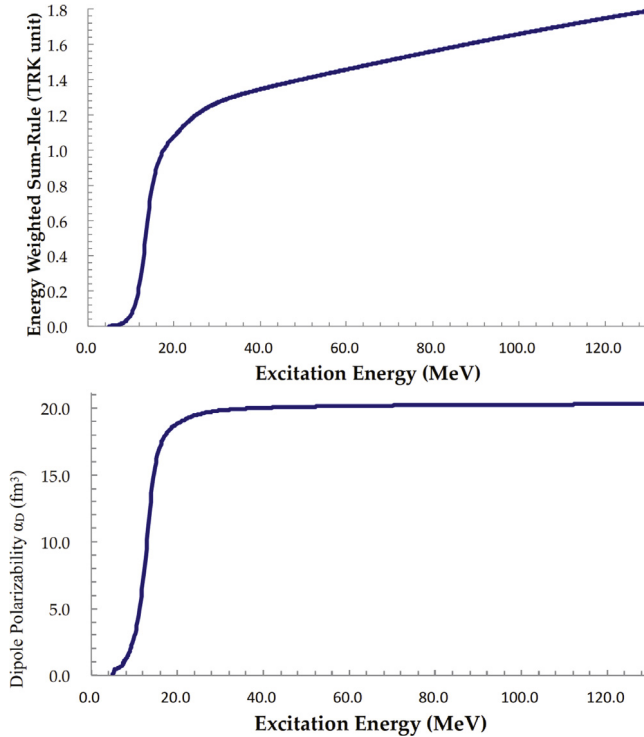


**Fig. 9.** The running sum of the energy weighted (TRK, upper panel) and the inversely energy weighted (electric dipole polarizability, lower panel)  $B(E1)$  strength distribution in  $^{208}\text{Pb}$ .

Source: Replot of the data in [17].

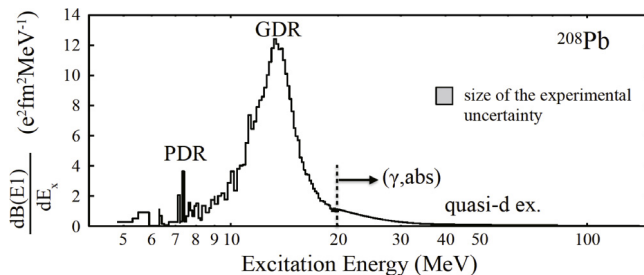


**Fig. 10.** The  $B(E1)$  strength distribution in  $^{208}\text{Pb}$  as a function of the excitation energy in the log-scale. In this plot, each area of the  $B(E1)$  strengths is proportional to the relative contribution to the electric dipole polarizability.

Source: Replot of the data in [17] and [62].

In a following work X. Roca-Maza et al. [57] showed that the correlation is model-dependent and rather the product of the electric dipole polarizability and the symmetry energy at the saturation density,  $J$ , has better correlation with the neutron skin thickness in the various set of relativistic and non-relativistic interactions. The correlation is suggested by the macroscopic droplet model. It was then found that the measured electric dipole polarizability in  $^{208}\text{Pb}$  in combination with the range of  $J = 31 \pm (2)_{\text{est}}$  MeV provides a neutron skin thickness in  $^{208}\text{Pb}$  of  $\Delta r_{np} = 0.165 \pm (0.009)_{\text{exp}} \pm (0.013)_{\text{theo}} \pm (0.021)_{\text{est}}$  fm [57]. With the context of the subtraction of the quasi-deuteron excitation contribution, as discussed above, the extracted neutron skin thickness from the electric dipole polarizability  $^{208}\text{Pb}$  slightly changed to  $\Delta r_{np} = 0.16 \pm (0.02)$  or  $\Delta r_{np} = 0.16 \pm (0.03)$ , where the uncertainty depends on the way of the estimation of the theoretical uncertainty [58].

Similarly the electric dipole polarizability was obtained also for the nucleus  $^{120}\text{Sn}$  and was found to be  $\alpha_D(^{120}\text{Sn}) = 8.93 \pm 0.36 \text{ fm}^3$  [51] as deduced from the analysis of the polarization transfer data of the  $^{120}\text{Sn}(p, p')$  reaction together with the available  $(\gamma, xn)$  data [64–66] integrated up to 135 MeV.

Another datum on neutron skin thickness was deduced for the unstable  $^{68}\text{Ni}$  and found to be  $0.12 - 0.16 \text{ fm}$  [46] (see Fig. 11). For the lighter  $^{48}\text{Ca}$  nucleus the neutron skin thickness was found to be  $0.14 - 0.20 \text{ fm}$  from the measured electric dipole polarizability in comparison with the EDF predictions and the *ab initio* coupled-cluster calculation employing the chiral effective interactions [53] (see Fig. 12). They found that the agreement between the experimental and theoretical

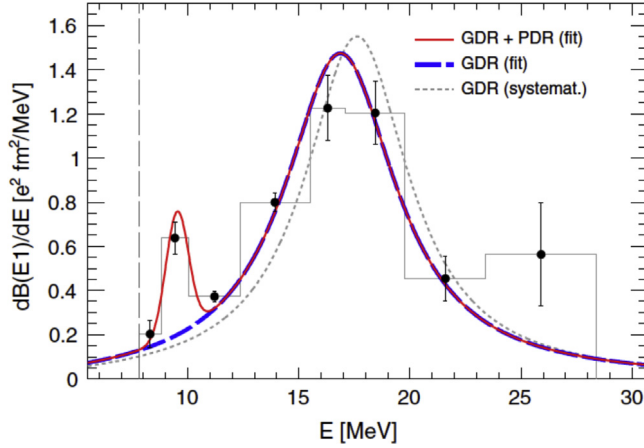


**Fig. 11.** Electric dipole strength distribution in  $^{68}\text{Ni}$  measured by Coulomb excitation at GSI [46].  
Source: The figure was taken from [46].

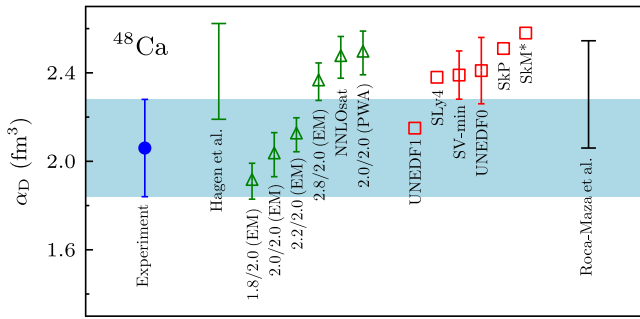


**Fig. 12.** The experimental results on the electric dipole polarizability ( $\alpha_D$ ) of  $^{48}\text{Ca}$  (blue bar) and theoretical predictions using coupled-cluster calculations with chiral effective interactions (green bar and the triangles) and the predictions of EDF calculations (red squares).  
Source: The figure was taken from [53].

results is better for excitation energies higher than the GDR one. A more satisfactory description of the dipole polarizability for  $^{48}\text{Ca}$  is obtained, in the GDR energy region, by using the subtraction procedure recently implemented in the subtracted second random phase approximation (SSRPA) model [67]. However, the computation of the electric dipole polarizability of  $^{48}\text{Ca}$  with an increased precision obtained by including leading-order three-particle-three-hole (3p-3h) excitation for the ground state, in the *ab initio* coupled-cluster calculation [68], improves the agreement with the data leaving unaffected the results for the charge radius of  $^{48}\text{Ca}$ .

The ensemble of the experimental results on the EDP allows to put constraints on the symmetry energy parameters. This is done by using the strong correlations between them as predicted by theoretical models. The nuclear equation of state in infinite nuclear matter at zero temperature is written conventionally as the equation of energy per particle  $E/A$  as a function of the nucleon density ( $\rho$ ) and the asymmetry parameter ( $\delta$ ) neglecting the Coulomb interaction as [69]

$$\frac{E}{A}(\rho, \delta) = \frac{E}{A}(\rho, 0) + S(\rho)\delta^2 + O\{\delta^4\} \quad (4)$$

$$\rho \equiv \rho_n + \rho_p \quad (5)$$

$$\delta \equiv \frac{\rho_n - \rho_p}{\rho_n + \rho_p} \quad (6)$$

where  $\rho_n$  ( $\rho_p$ ) is the neutron (proton) density. The coefficient of  $\delta^2$ ,  $S(\rho)$ , is called the symmetry energy, and is further expanded at around the nuclear saturation density ( $\rho_0$ ) as

$$S(\rho) = J + \frac{L}{3\rho_0}(\rho - \rho_0) + O\{(\rho - \rho_0)^2\}, \quad (7)$$

here  $J$ , often denoted as  $S_0$ , and  $L$  are the symmetry energy and the slope parameter at the saturation point. Those parameters are important to understand the equation of state of neutron-rich matter, and eventually the neutron matter. The experimental constraints on the symmetry parameters  $J$  and  $L$  from the electric dipole polarizability in  $^{208}\text{Pb}$  was first

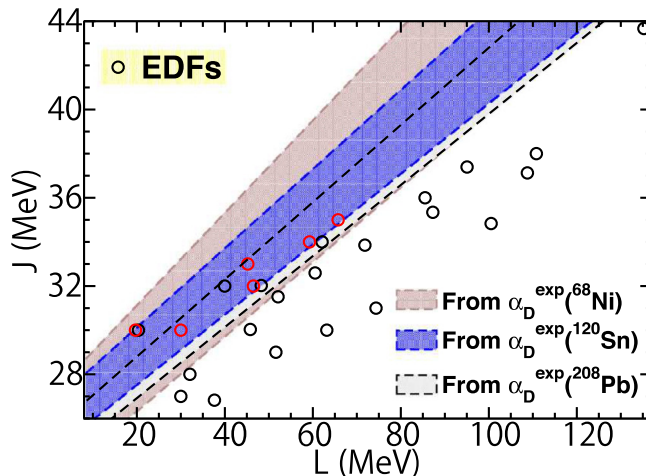


**Fig. 13.** Constraint on the symmetry energy parameters,  $J$  and  $L$ , extracted from the electric dipole polarizability data on  $^{208}\text{Pb}$  [17],  $^{120}\text{Sn}$  [51] and  $^{68}\text{Ni}$  [46]. The circles show the predictions of the random-phase approximation using nuclear energy density functionals.

Source: The figure was taken from [58].

shown in [70], then later revised in [58] as shown in Fig. 13. In the latter result, the quasi-deuteron excitation contribution in the experimental data was subtracted from the total electric dipole polarizability, resulted in  $\alpha_D(^{208}\text{Pb} - q.d.) = 19.6 \pm 0.6 \text{ fm}^3$ , since the quasi-deuteron excitation mechanism is not implemented in the used theoretical models. Mean-field calculations of nuclear energy density functional approach were employed to extract the theoretical correlations between the electric dipole polarizability and the symmetry energy parameters [58]. It is interesting to plot together the constraints on the symmetry parameters  $L$  and  $J$  from the electric dipole polarizability data of  $^{120}\text{Sn}$  after subtraction of the quasi-deuteron excitation contribution,  $\alpha_D(^{120}\text{Sn} - q.d.) = 8.59 \pm 0.37 \text{ fm}^3$ , and from the Coulomb excitation data of unstable  $^{68}\text{Ni}$  integrated up to 28.4 MeV [46],  $\alpha_D(^{68}\text{Ni}) = 3.88 \pm 0.31 \text{ fm}^3$ . This is done in Fig. 13 showing that the constraints from the three experimental data are essentially carrying the same information and are in a good agreement with each other.

### 3.2. Nuclear resonance fluorescence for low-lying dipole states

The nuclear resonance fluorescence (NRF) method using photon beams has been widely employed to study the electric dipole strength distribution in nuclei below the particle emission threshold. The study of the low-lying electric dipole strength or the pygmy dipole resonance by high-resolution NRF experiments started around the end of last century with works at Gent and at the S-DALINAC laboratories. At Gent the first experiments were aimed to investigate the nuclei  $^{116,124}\text{Sn}$  [71],  $^{56}\text{Fe}$ , and  $^{58}\text{Ni}$  [72] and used unpolarized and partially linearly polarized real photon beams produced by bremsstrahlung of electrons. At S-DALINAC the experiments were devoted to the study of the  $^{89}\text{Y}$  [73] nucleus, to the N=82 nuclei  $^{138}\text{Ba}$ ,  $^{140}\text{Ce}$ ,  $^{142}\text{Nd}$  and  $^{144}\text{Sm}$  [74–77] and to  $^{204,206,207,208}\text{Pb}$  [78–80]. The other laboratories involved in this type of experiments are ELBE, and more recently HIγS, and AIST.

While detailed history and results of the NRF experiments is summarized in the reviews [1,81,82], here we report a table containing the references, the main features of the experimental conditions and the obtained results. In addition, some brief discussions are reported in this section. To be noted that we limit our discussions for the case of gamma-decays for which one or more photons are emitted in the de-excitation process of the resonant nucleus. The gamma-ray emitted from the initial resonant state is called the *primary gamma-ray*. It is reminded that a photon scattering process is called *elastic* when the energy of the emitted primary gamma-ray is the same as the energy of the absorbed photon leaving the residual nucleus in the ground state. On the other hand, a photon scattering process is called *inelastic* when the energy of the primary gamma-ray is less than the energy of the absorbed photon leaving the residual nucleus in an excited state. The residual nucleus emits further gamma-rays, and these are called *cascade gamma-rays*.

Concerning the terminology for the detection of the emitted gamma-rays and for the analysis of the data we recall here that the full-energy peak corresponds to the energy of the incident gamma-ray and that the continuous component is originated from the Compton-scattering of incident gamma-ray in the detector. Also single and double escape peaks appear in the measured spectra when the incident gamma-ray energy is higher than the double of the electron mass. In the conventional NRF method, only the full energy peaks are analyzed and this is called *peak-by-peak* analysis. The method has a detection *sensitivity limit* on the *resolved* peaks. Below the limit, the peaks are not recognized in the analysis. They are called *unresolved peaks* or *unresolved strengths*. The limit originates from the photo-absorption cross section of the individual peaks, statistical fluctuation, signal to noise ratio, and the level density at the measured excitation energy

**Table 1**

A list of the experimental works on the pygmy dipole resonance with the NRF method ordered with increasing year of the publications. The figures and table listed in column 7 refers to the ones present in the quoted references.

Target	Exp. method	Device or facility	Measured $E_x$ MeV	Analysis method	Claimed PDR $E_x$ MeV	Strength $e^2 \text{fm}^2$ or % TRK	References
$^{140}\text{Ce}$	NRF	SD	−6.7	res.	~6	(Fig. 3)	[74]
$^{89}\text{Y}$	NRF	SD	−7	res.	~6.3	(Table 1,2)	[73]
$^{116}\text{Sn}$	NRF, $\vec{\gamma}$	Gent	−10	res.	~6.5	0.233(28) in 4–8.5	[71,83]
$^{124}\text{Sn}$	NRF, $\vec{\gamma}$	Gent	−10	res.	~6.5	0.379(45) in 4–8.5	[71,83]
$^{138}\text{Ba}$	NRF, $\vec{\gamma}'$	SD	−6.7	res.	5–6.7	(Table 1)	[75]
$^{204}\text{Pb}$	NRF	SD	−6.7	res.	–	0.235(73), 0.193(59)% <sup>g</sup>	[78,80]
$^{206}\text{Pb}$	NRF	SD	−6.7	res.	–	0.391(67), 0.300(52)% <sup>g</sup>	[78,80]
$^{208}\text{Pb}$	NRF	SD	−6.7	res.	–	0.944(76), 0.705(58)% <sup>g</sup>	[78,80]
$^{56}\text{Fe}$	NRF, $\vec{\gamma}$	Gent	−10	res.	~8.2	0.127 in 5–10	[72]
$^{58}\text{Ni}$	NRF, $\vec{\gamma}$	Gent	−10	res.	~8.2	0.110 in 5–10	[72]
$^{40}\text{Ca}$	NRF	SD	−10	res.	–	0.0051(8), 0.023(4)% in 5–10	[84,85]
$^{48}\text{Ca}$	NRF	SD	−10	res.	–	0.0557(41), 0.27(2)% in 5–10	[84,85]
$^{208}\text{Pb}$	NRF	SD	−8	res.	~7.4 ( $S_n$ )	2% in <8	[79]
$^{207}\text{Pb}$	NRF	SD	−6.7	res.	–	(Table 7)	[80]
$N = 82^h$	NRF	SD	...	stat. prop.	–	...	[77]
$^{92}\text{Mo}$	NRF	ELBE	4–12.7( $S_n$ )	unres.	~6.5 and ~9	28 <sup>b</sup> in 6–10	[86,87]
$^{98}\text{Mo}$	NRF	ELBE	4–8.6( $S_n$ )	unres.	~6.5 and ~9	(Fig. 5)	[86]
$^{100}\text{Mo}$	NRF	ELBE	4–8.3( $S_n$ )	unres.	~6.5 and ~9	(Fig. 5)	[86]
$^{138}\text{Ba}$	NRF	SD/DHIPS	4.0–8.6	res.	~6.5	0.681(119) <sup>e,f</sup>	[76,88,89]
$^{140}\text{Ce}$	NRF	SD	3.6–7.7	res.	~6.3	0.308(59) <sup>e,f</sup>	[76,88]
$^{142}\text{Nd}$	NRF	SD	3.4–7.1	res.	~6.1	0.184(31) <sup>e</sup>	[88]
$^{144}\text{Sm}$	NRF	SD	3.2–7.0	res.	~5.7	0.208(35) <sup>e,f</sup>	[76,88]
$^{88}\text{Sr}$	NRF, $\vec{\gamma}$	ELBE	−12	stat.	6–11	45 <sup>b</sup> in 6–10	[87,90]
$^{112}\text{Sn}$	NRF	SD	4–9.5	res.	5–8	0.174(26), 0.29% <sup>c</sup>	[83]
$^{90}\text{Zr}$	NRF	ELBE	−12.9	stat./unres.	6–11	42 <sup>b</sup> in 6–10	[87,91]
$^{140}\text{Ce}$	NRF, $\vec{\gamma}'$	DHIPS	6.1–6.9	$\pi$ -det.	–	–	[92]
$^{139}\text{La}$	NRF	ELBE	5.4–9.0	stat./unres.	6–10	(Table I, Fig. 8)	[93]
$^{208}\text{Pb}$	NRF	ELBE	4.8–7.5	stat./unres.	–	(Table I)	[94]
$^{136}\text{Xe}$	NRF	DHIPS	3.6–8.1	res./frag.	5–8	0.65 <8.02	[95]
$^{142}\text{Nd}$	NRF	H $\gamma$ S	4.2–9.7	res.	~6.5 and ~7.8	(Fig. 2)	[96]
$^{238}\text{U}$	NRF-LCS, $\vec{\gamma}$	H $\gamma$ S	2.0–4.2 (6.2 <sup>d</sup> )	res./unres.	no PDR	(Table II, Fig. 9)	[97]
$^{130}\text{Te}$	NRF-LCS	DHIPS/H $\gamma$ S	5.50–8.15	casc./unres./inel.	6–8.5 (6.82, 7.85)	1.82(5)% (0.83(6))% <sup>a</sup>	[98]
$^{76}\text{Se}$	NRF-LCS	H $\gamma$ S	4–9	res.	6–8	0.132(29) at 4–9	[99]
$^{92}\text{Mo}$	NRF-LCS	DHIPS/H $\gamma$ S	1–8.7	res., casc.	5.5–7.5	Table II	[100]
$^{60}\text{Ni}$	NRF-LCS	DHIPS/H $\gamma$ S	−10	res., casc.	~8	0.1538(95), 0.5% <sup>c,e</sup>	[101,102]
$^{86}\text{Kr}$	NR-LCS F	ELBE and H $\gamma$ S	4.7–9.3	unres/casc/stat.	6–11	35 <sup>b</sup> in 6–10	[87]
$^{181}\text{Ta}$	NRF	ELBE	5.0–7.6	quasi-cont, stat.	6–8	(Fig. 6)	[103]
$^{140}\text{Ce}$	self-abs	DHIPS	3.5–7.5	res.	–	(Fig. 3)	[14]
$^{205}\text{Tl}$	NRF-LCS	DHIPS/H $\gamma$ S	4.0–6.4	reso.	~4.9 and ~5.5	(Table 1)	[104]
$^{140}\text{Ce}$	NRF-LCS	$\gamma^3$ -H $\gamma$ S	5.2–8.3	unres., cascade	–	(Fig. 3)	[105]

<sup>a</sup>GDR tail subtracted.

<sup>b</sup>In the unit of MeV mb.

<sup>c</sup>0.2509(311), 0.8% if branching to the low-lying levels are considered.

<sup>d</sup>Including the analysis of the unresolved strengths.

<sup>e</sup>In the measured excitation energy region.

<sup>f</sup>The values in [88].

<sup>g</sup>The values in [88].

<sup>h</sup> $^{138}\text{Ba}$ ,  $^{140}\text{Ce}$ ,  $^{142}\text{Nd}$  and  $^{144}\text{Sm}$ .

region. In the following the main results of the extensive experimental work carried out using the NRF technique during the years are summarized.

It is anticipated that in all nuclei it was found that there is an E1 strength in excess as compared to the tail of the Lorentzian function describing the giant dipole resonance state (GDR). The position of this extra strength, its intensity, and also the decay from these states has some mild variation with the mass number and moreover with the nuclear level density. In describing the main results special attention is given to the more recent works for which efforts were made to increase the sensitivity to weak transitions.

In the following the main results of the extensive experimental work made using the NRF and self absorption techniques are briefly described. The presentation of these results is organized in mass regions. In fact, because of the existence of several results, a good fraction of them rather recent, an organization of their presentation is needed. This presentation points out that the studies of the low lying dipole response have addressed different mass regions in order to find out whether or not there are similarities and/or differences and in order to identify possible effects related to shell closures, to neutron excess and to level densities. Table 1 reports, in a compact form, data concerning the pygmy dipole

resonance obtained with the NRF and self absorption techniques together with the references to corresponding papers. To be noted that in most cases the energy of the used gamma beams, also reported in Table 1, is below the particle separation energy. In fact, the low-lying dipole strength just above the particle separation energy was not yet measured with these techniques.

#### The mass region 40–50

Three isotopes of Ca with N=20, 24 and 28 were studied at high resolution and the results show that the number of states of  $1^-$  type is increasing in  $^{48}\text{Ca}$  as compared with  $^{40}\text{Ca}$  [84,85]. Discussion on the results in this mass region can be found in Section 5 where excitation cross sections with gamma scattering are compared with those obtained using inelastic scattering of alpha particles.

#### The mass region 60–80

In this mass region special attention was given to the study of the dipole response in different isotopes of Fe and Ni. Several experiments of NRF type were made at Gent for the nuclei  $^{56}\text{Fe}$  and  $^{58}\text{Ni}$  using unpolarized and partially linearly polarized photons produced as bremsstrahlung radiation. The end point energies of the used photon beams were 6.5, 10, and 12 MeV. The relevant result was the observation of more than 60 levels in the excitation energy region between 2 and 10 MeV including many of E1 type. The E1 strength distribution was found to show a narrow concentration at around 8.2 MeV [72].

For the more neutron rich  $^{60}\text{Ni}$  nucleus the E1 strength distribution exhibits a similar pattern as in  $^{58}\text{Ni}$  and  $^{56}\text{Fe}$  nuclei. All three isotopes are characterized by the presence of a structure of levels strongly excited lying at an excitation energy near to 8 MeV. However, it should be noted that in  $^{60}\text{Ni}$  this structure is found approximately 700 keV lower than in  $^{58}\text{Ni}$ . The M1 strength distributions of the three isotopes are also quite similar to each other.

The interpretation of the presence of spin 1 states below the neutron binding energy in these nuclei was made using predictions obtained within the QPM model (see Section 4.1). It was found, as a main result, that with increasing excitation energy the structure of the excited states is characterized by a complex admixture of different components and exhibits rather large inelastic branching ratios leading higher-lying excited levels.

More recently further experimental investigation was carried out for  $^{60}\text{Ni}$  (as well as  $^{58}\text{Ni}$ ) in order to provide more detail information on the character of the states and to detect the decay cascades [101,102]. The E1 and M1 excitations in  $^{60}\text{Ni}$  (as well as  $^{58}\text{Ni}$ ) were studied. For this purpose the two facilities DHIPS and HI $\gamma$ S were used, the first providing unpolarized gamma beams and the second providing quasi monoenergetic polarized gamma beams. From these experiments it was possible to identify 48  $1^-$  states, 32  $1^+$  states, and 5 spin-1 states (undetermined parity). At HI $\gamma$ S, cascade decays were also observed by detecting the gamma-transitions from low-lying states (Fig. 14). The ground state branching ratios were extracted for each of the spins as a function of the excitation energy (beam energy). For the specific results the reader is referred to Refs. [101,102]. It is found that for the  $1^-$  states, the ground state branching ratio decreases as the excitation energy increases and it goes from 75% (7.65 MeV) to 50% (9.66 MeV).

To study the  $1^-$  states at around the neutron binding energy in deformed nuclei, the nucleus  $^{76}\text{Se}$  with a sizable deformation ( $\beta = 0.309(4)$ ) was investigated at HI $\gamma$ S with polarized gamma-ray beams. This work complemented a previous work with unpolarized photons [99]. Excited states of E1 and M1 types were identified by the azimuthal angle asymmetry with the angle defined as that one between the direction of emitted photon with respect to the linear polarization plane of the photon beam. The self-absorption contribution in the relatively large target (consisting in 12g contained in  $1.4 \text{ cm} \phi \times 2.6\text{cm-L}$ ) was taken into account. The corresponding correction was found to be of the order of 1%–10% for the states with a width for a ground state decay in the interval  $\Gamma_0 > 0.3$  eV. Due to the limited statistics of that experiment it was possible to analyze only the discrete peaks corresponding to the direct ground state decay except for a few decays corresponding to branching ratios to the first  $2_1^+$  state at 559.1 keV (for this point see the detailed data in Table I of [99]). An enhancement of the photo-absorption cross section was observed in spectral distribution in the region between 6 and 8 MeV. The inclusion of cascade decays (inelastic channel) appears to be important. The number of cascade gamma decays through excited states are in this case a few times higher than those populating directly the ground state. This is interpreted as due to the fact that the level density is rather large. This implies the presence in the measured spectra of a sizable contribution from unresolved strengths and this affects to large extent the determination of the relative intensity between the direct g.s. decay and the cascade decays. The size of the unresolved strength is excitation energy (level density) dependent. These two decays, the direct g.s. decay and the cascade decays were somehow separated in later works of [98] and [105].

The electric dipole strength in  $^{86}\text{Kr}$  has been deduced with an experiment using the unpolarized gamma beam produced by bremsstrahlung at ELBE [87]. Parity assignment of each state was done by polarized gamma beam experiment at HI $\gamma$ S. The experiment allows to identify 39  $1^-$  states with energy up to 10.1 MeV.

The data including continuum (unresolved strengths) were deconvoluted by the detector response. After subtracting the atomic backgrounds, cascade branches were subtracted by using the ground state branching ratios simulated by a statistical model. Then the spectrum was divided by the ground state branching ratio to present the photo-absorption cross section including the elastic and inelastic channels. The comparison between data at the beam energies of 11.2 and 7.9 MeV was used to deduce the feeding from higher lying states which looks non-negligible below the gamma energy of 6 MeV and increases much below 4 MeV. The contribution from the continuum is stressed to be important. The amount of the continuum strength increases from similar amount to reach a factor of 5 (84% in the continuum) of the strength in the resolved peaks from 5.5 to 10 MeV.

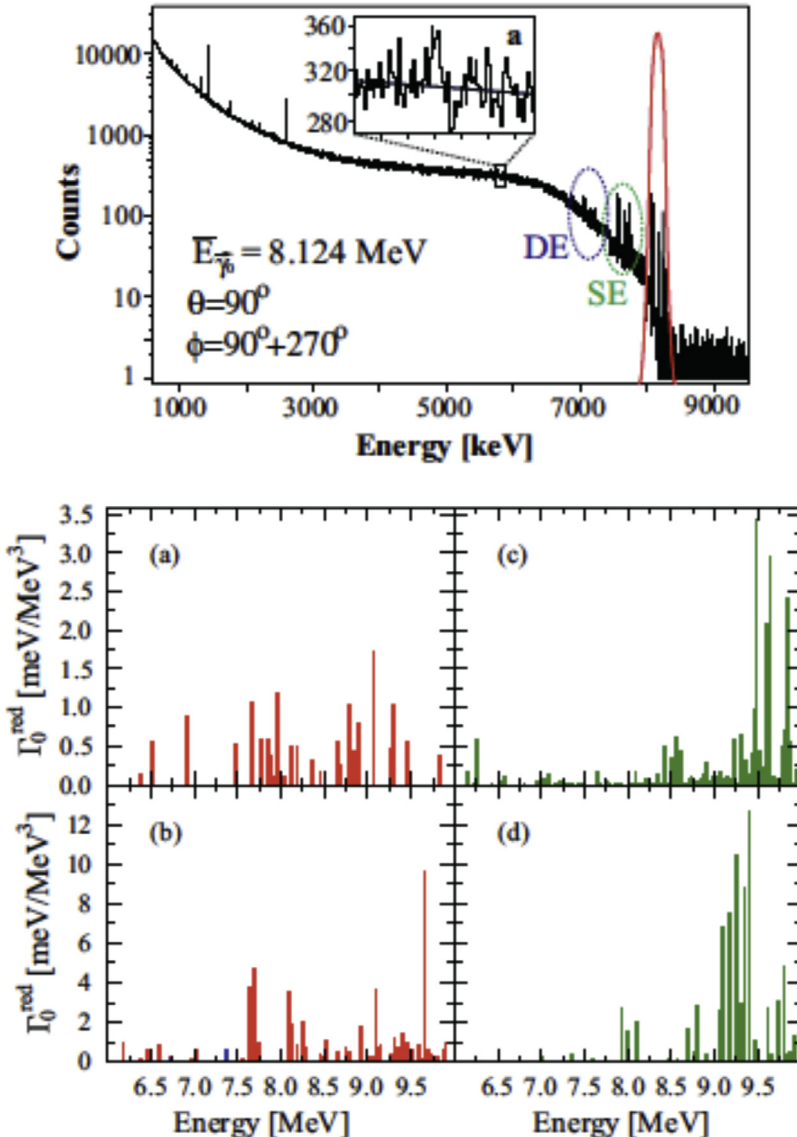


**Fig. 14.** Top panel: spectrum of  $\gamma$ -decay from the nucleus  $^{60}\text{Ni}$  recorded with detectors perpendicular to the polarization plane at the incident photon beam 8.124 MeV. The inset shows a peak at 5800.2 keV belonging to a transition from the  $1^-$  state at 8086 keV to the first excited  $0^+$  state at 2285 keV. Labels denote the energy of the single-escape peaks (SE) and double-escape peaks (DE). Bottom panel: Partial experimental transitions of M1 type – (a) and E1 type – (b) for  $^{60}\text{Ni}$ . The corresponding predictions within the QPM model are in (c) and (d).  
Source: Adapted from [102].

It is important to point out that the contribution from the continuum is found to depend on the nucleus and thus on the nuclear structure. For more details on this point see [90,96,98]

It is found that the photon strength functions calculated using the standard Lorentzian parametrizations do not fit the NRF data below particle binding energy. The procedure for calculations was then modified in later work on  $^{181}\text{Ta}$  [103].

The data after statistical corrections are connected well with the data above the neutron separation energy measured by  $(\gamma, n)$  at H1 $\gamma$ S [106]. A peak at 6 MeV and a resonance-like structure in the energy interval from about 7–11 MeV were found in the photo-absorption cross section spectrum. The sum of the measured absorption cross sections weighted with the corresponding energy bins in the energy interval from 6 to 10 MeV was constructed in order to examine the behavior of the strength with the increase of  $N/Z$  value. It was concluded that the strength of the  $N = 50$  isotones did not show a clear increasing trend by making the value of  $N/Z$  larger [88].

The experimental work on the nucleus  $^{88}\text{Sr}$  [90] provided interesting data since 160 levels up to an excitation energy of 12 MeV were identified. The work was carried out at the electron linear accelerator ELBE using bremsstrahlung radiation produced at kinetic electron energies of 9.0, 13.2 and 16.0 MeV. By using polarized photons linear polarization of about

50 gamma transitions were measured which enabled parity assignments. Statistical methods were used in the analyses of the data in order to deduce the intensities of inelastic transitions and to correct the intensities of the ground-state transitions for their branching ratios. An enhancement of E1 strength in the region at 6–11 MeV may be considered as an indication of the presence of a pygmy dipole resonance.

#### *The mass region 90–100*

Among the results obtained in this mass region it is important to stress the work on the even–odd nucleus  $^{89}\text{Y}$  and its results in comparison with the neighboring even–even nuclei. The experiment on the nucleus  $^{89}\text{Y}$  was performed at the S-DALINAC laboratory with bremsstrahlung beams and using the HpGe cluster detectors of the EUROBALL array [73] to measure the gamma-rays emitted by the nucleus after its excitation. An unusually large concentration of E1 strength was found at around 6.3 MeV which was interpreted in terms of a constructive interference of a strong two-phonon amplitude with weak admixtures of states belonging to the low-energy tail of the GDR. To be noted that at about 6.3 MeV, very strong electric dipole transitions were identified in the  $^{88}\text{Sr}$  nucleus and in  $^{90}\text{Zr}$  nucleus. In the odd  $^{89}\text{Y}$  nucleus, the whole strength amounts to about 60% of the value found in the neighboring even nuclei, and in contrast to the even nuclei having the strength well concentrated in a very narrow energy interval, for the  $^{89}\text{Y}$  nucleus the E1 strength was found to be fragmented. This could point out to effects due to couplings of the core excitation to single particle excitation.

The nucleus  $^{90}\text{Zr}$  magic in neutron number was investigated via photon-scattering experiments performed at the ELBE laboratory by employing beams produced with electron bremsstrahlung at kinetic electron energies of 7.9, 9.0 and 13.2 MeV [91]. Statistical methods were applied to estimate intensities of inelastic transitions and to correct the intensities of the ground state transitions for their branching ratios. This cross section was found to match well the photo-absorption cross section obtained from  $(\gamma, n)$  data. An enhancement of E1 strength was found in the range of 6 to 11 MeV. Furthermore the model predictions for these states within the QPM model indicate a peculiar feature of this E1 strength. In fact, it was deduced that the shape and radial distribution of the transition densities of the states at 6 to 11 MeV are different than those of the giant dipole resonance. The experimental work together with the theoretical calculations, showed that these states, denoted as PDR modes, are clearly distinguishable in their microscopic features than those from the GDR. This point is discussed further in Section 5 where the present results are compared with those obtained with inelastic scattering of ions. In addition, the analysis presented in [91] shows that standard strength functions currently used for the calculation of reaction data do not describe the dipole-strength distribution below the  $(\gamma, n)$  threshold correctly. Therefore below the neutron binding energy the description of the shape of the E1 strength function should take into account the presence of the observed extra strength.

The study of the three isotopes  $^{92,98,100}\text{Mo}$  (performed at ELBE) shows that the gamma strength follows a Porter–Thomas distribution and most of the dipole strength is found in weak and unresolved resonances appearing as fluctuating cross section [86]. Therefore an analysis of the quasi-continuum was made, combining smoothly the obtained results of  $(\gamma, \gamma')$  data with those obtained from  $(\gamma, n)$  reaction. In this case it was pointed out that for a reasonable extraction of the gamma strength information one should not ignore the fluctuating quasi-continuum part of the cross section. Enhancements at 6.5 MeV and at 9 MeV were found and were interpreted as due to the pygmy dipole resonances.

In a more recent work the nucleus  $^{94}\text{Mo}$  was investigated at the S-DALINAC and at the HIyS facilities up to an excitation energy of 8.7 MeV. In total 83 excited states were identified. Parity quantum numbers were assigned to 41 states. Fig. 15 shows the measured  $B(E1) \uparrow$  strength distribution as a function of excitation energy. The sensitivity limit of the used experimental setup is also shown in the figure to indicate that transitions weaker than the shown sensitivity limit cannot be observed. The states in the region from 5.5 to 7.5 MeV have an enhanced decay to ground state. In particular, the experimentally deduced mean branching ratios exhibit a resonance-like structure at 6.4 MeV and this cannot be reproduced within the statistical model. This indicates a nonstatistical structure in the energy range between 5.5 and 7.5 MeV.

The measured  $B(E1) \uparrow$  strength in  $^{94}\text{Mo}$  is compared with predictions in Fig. 15. The predictions were obtained in the framework of the quasiparticle–phonon model using a basis which includes one-, two-, and three-phonon configurations. Up to the end point of 8.7 MeV the calculated distribution shows a rather good agreement with the calculations. Also the fragmentation of the strength is well reproduced. This seems to imply that the QPM model seems to properly treat the damping mechanism of the PDR which is included in the model as coupling to complex configurations.

#### *The mass region 120–130*

In this mass region the Sn isotopes attract particular interest both for experiment and for theory having as number of protons a magic number and having several isotopes for which neutron excitations could be identified. The low lying E1 strength was investigated using the gamma beams at Gent [107]. In particular, the experiments devoted to the investigation of the  $^{116}\text{Sn}$  and  $^{124}\text{Sn}$  nuclei were carried out using linearly polarized bremsstrahlung photons and unpolarized bremsstrahlung photons with three different end point energies (4.1, 7.5, and 10 MeV) [71]. More than 150 new dipole ground state transitions were identified. The E1 strength distribution of both isotopes showed a clear concentration of the E1 strength at excitation energy around 6.5 MeV. The measurements were performed up to 9 MeV and in that region another bump is visible. The feedings from higher lying states were deduced by using three different end-point energies for the bremsstrahlung radiation.

Two other isotopes of Sn, namely  $^{112,120}\text{Sn}$  were studied at the laboratory S-DALINAC using different endpoint energies of the incident bremsstrahlung spectrum below the neutron separation energy. For these two Sn isotopes a concentration of dipole strength is observed between 5 and 8 MeV.

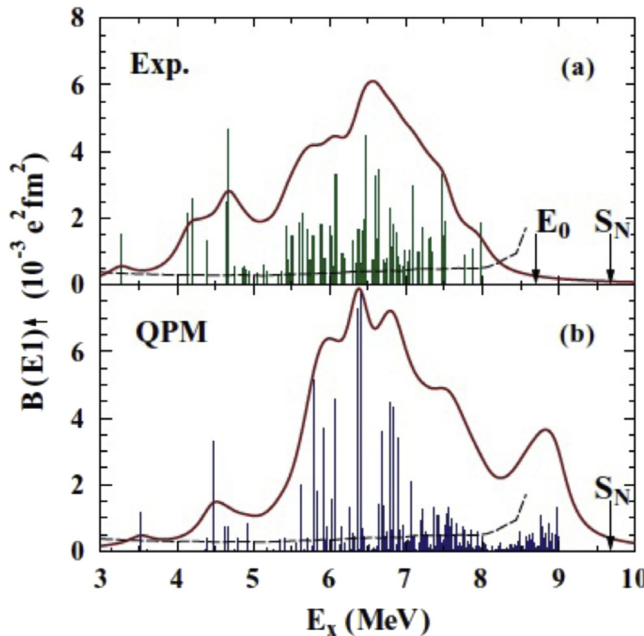


**Fig. 15.** Measured (top panel) and predicted (bottom panel) electric dipole strength distribution for the nucleus  $^{94}\text{Mo}$ . The endpoint energy of the experiment is marked by  $E_0$  and the neutron separation energy by  $S_N$ . The experimental sensitivity limit is given by the gray curve in the top panel.

Source: From [100].

More recently, the electric dipole response of  $^{130}\text{Te}$  was investigated using an unpolarized gamma beam produced by bremsstrahlung with the DHIPS facility at S-DALINAC laboratory, and by quasi-monochromatic polarized gamma-rays at HgS [98]. The gamma emission by the direct decay to the ground state and by the cascade decay from several low-lying excited states to the ground state were observed. To deduce the unresolved strengths, the peak counts corresponding to the direct ground-state decay was taken as the lower-limit, and the continuum part of the spectrum to the ground-state was taken as the upper limit (without correction of the non-nuclear excitation and detector responses, in contrast to [105]). The obtained result (see Fig. 16) showed that the contribution from the unresolved strengths is important at the excitation energy above 7 MeV. In the experiment the total photoabsorption cross sections, the elastic and inelastic cross sections were measured. In addition, the average ground state branching ratio  $\langle b_0 \rangle$  was extracted assuming that the first excited state ( $2^+$ ) collects all the cascade decays from the initial excited states. The value of  $\langle b_0 \rangle$  tends to decrease from 0.9 at 6 MeV to 0.4 at 8 MeV.

In the work on  $^{130}\text{Te}$  a new quantity  $\lambda$  was also defined, representing a parameter giving the exponential decrease of the relative intensity of the decays from each  $2^+$  excited states to the ground state comparing with the decay from the first  $2^+$  excited state to the ground state as a function of the excitation energy of  $2^+$ . The deduced  $\lambda$  looked constant with the value of the initial excitation energy (this is shown and discussed in [105]). The result indicates that the cascade decay patterns (namely the intensity as a function of the excitation energy) through the low-lying first  $2^+$  states are similar among them, but they are different from the direct decay to the ground state.

The result was compared with calculation of the decay assuming to be of statistical nature. For this calculation experimental inputs of known levels were used for the low-lying states below an energy of 2.62 MeV and above that energy calculated levels were used. The used level-density is an empirical one [108]. The theoretical predictions for the photon-strength function were made assuming a few kinds of shapes for this  $^{130}\text{Te}$  nucleus. It was found that no statistical calculations could reasonably reproduce the ground state branching  $\langle b_0 \rangle$  and the average population of the quantity  $\lambda$  and their excitation energy dependence. It was then concluded that statistical models or concepts derived from them seem to be inadequate tools for extracting the dipole photon strength function or for estimating decay properties in that energy region. Moreover, by using the simple ansatz to separate the total photoabsorption cross section ( $\sigma_{\gamma}^c$ ) into a part which decays into the ground state ( $\sigma_{\gamma}^{gs}$ ) and a part which decays according to the statistical model, it is found that the ratio  $\frac{\sigma_{\gamma}^{gs}}{\sigma_{\gamma}^c} \sim 0.42$ . Therefore, at this low excitation energy region, a large fraction of the E1 strength does not decay according to the statistical model; other mechanisms depending on the nuclear structure may be present.

#### The mass region 140–150

In this mass region several works were made on the nuclei with  $N = 82$ .

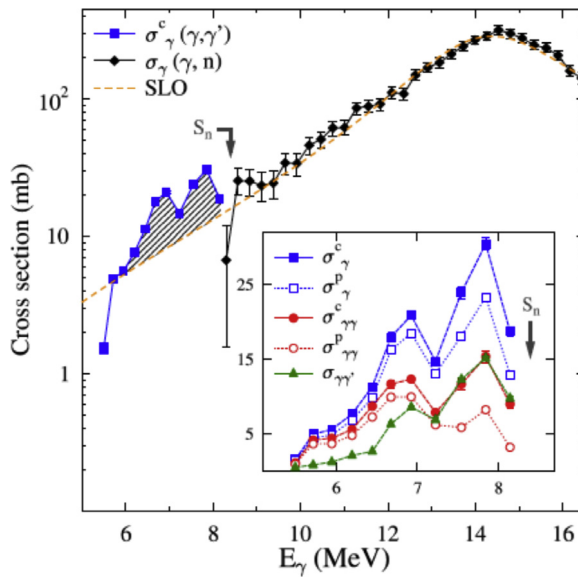


**Fig. 16.** Total photoabsorption cross sections ( $\sigma_{\gamma}^i$ ) as well as elastic ( $\sigma_{\gamma\gamma}^i$ ) and inelastic ( $\sigma_{\gamma\gamma\gamma}^i$ ) cross section from ( $\gamma, \gamma'$ ) and ( $\gamma, n$ ) experiments for the nucleus  $^{130}\text{Te}$ . The superscript  $i$  indicates whether the cross section is extract from the resolved peaks (p) or takes into account the contribution of the continuum (c). Blue squares: total photoabsorption cross section; red dots: elastic cross section; green triangles: inelastic cross section. The hatched area corresponds to 0.83(6)% of the TRK sum rule.

Source: Figure taken from [98].

The low-lying E1 response of the  $^{140}\text{Ce}$  nucleus was measured at the laboratory S-DALINAC using the HpGe cluster detectors of the EUROBALL array [74]. The data, found to be in good agreement with previous low-resolution results obtained in Illinois with tagged photons, allowed to identify 54 individual transitions. Enhancement of the strength has been observed from around 6 MeV, but the experiment used gamma beams with energy only up to 6.7 MeV, in contrast with the tagged photon result showing a sizable strength up to around 9 MeV.

After that work other  $N = 82$  nuclei, namely  $^{138}\text{Ba}$ ,  $^{140}\text{Ce}$  and  $^{144}\text{Sm}$ , were investigated with photon scattering experiments up to an excitation energy of about 10 MeV using the S-DALINAC facility. The measured E1 strength distribution showed a resonance like structure covering the energy region between 5.5 and 8 MeV [76].

It is interesting to note that in the case of the  $^{138}\text{Ba}$  nucleus the measurement at the S-DALINAC with two EUROBALL cluster detectors showed a concentration of the E1 strength at around 6 MeV, but in that experiment the strength was measured only up to 6.5 MeV [75]. In contrast, later on, other tagged photon results showed continuous strengths up to around 8 MeV [76] and [89].

Statistical properties of the electric pygmy resonances in  $N = 82$  nuclei,  $^{138}\text{Ba}$ ,  $^{140}\text{Ce}$ ,  $^{142}\text{Nd}$  and  $^{144}\text{Sm}$ , were also studied. Statistics are found to be mixed, i.e. in between the predictions of random matrix theory for correlated and uncorrelated spectra [77].

The nucleus  $^{140}\text{Ce}$  was also investigated with unpolarized photons at the S-DALINAC laboratory with the Compton polarimetry method to deduce the parity quantum number of spin 1 states at energy up to 7 MeV. Those measurements used the fourfold segmented HPGe clover detector. For all investigated dipole transitions asymmetries are found which correspond to negative parity of the excited states [92].

More recently other experiments were made for the nucleus  $^{140}\text{Ce}$  (see e.g. [10,14,105]). In particular in [105] the decay properties from the pygmy resonance were investigated using the NRF technique combined with  $\gamma$ - $\gamma$  coincidence techniques. In this way branching ratios for transitions to low-lying excited states were deduced in a direct and model-independent way. The branching ratios were obtained for individual excited states and for specific intervals in excitation energy. The measurement of the decay pattern of pygmy states is of particular relevance since it provides additional insight into the nature of the decay mechanism of the PDR and it thus poses a new challenge for nuclear theory. The role of many complex 2p-2h and 3p-3h configurations in the fragmentation of the 1p-1h doorway  $1^-$  states has been already studied via ground-state transitions, and good agreement to data has been reported [105]. The investigation of direct decays of the PDR to low-lying states allows to draw conclusions on how some particular 2p-2h configurations, namely the PDR built on top of these low-lying states, are mixed with the PDR itself.

Experimentally, the direct observation of transitions to excited states is known to be challenging, since existing works show that branching ratios  $\Gamma_i/\Gamma$  to states other than the ground state are small in comparison to the decay to the ground state. Therefore, most experiments were limited by their experimental sensitivity to the observation of direct decays to the ground state, and only indirect measurements of the decay pattern via the decay of low-lying states [10] were

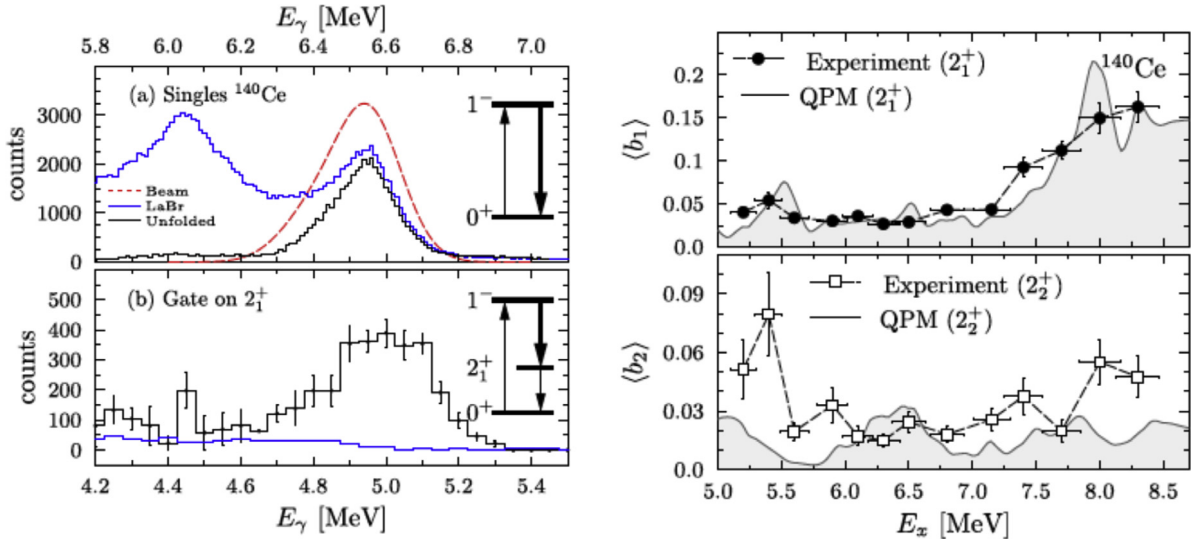


**Fig. 17.** Experimental data for  $(\gamma, \gamma')$  and theoretical predictions for the nucleus  $^{140}\text{Ce}$ . Single and coincidence spectra are shown on the left-hand side. Data for the decay branchings from  $1^-$  states to the first and second  $2^+$  states are shown in comparison with the corresponding predictions within the QPM model.

Source: Figure taken from [105].

possible. A recent alternative approach to determine  $\Gamma_0/\Gamma$  used the nuclear self-absorption method [14]. In that work the experimental averaged branching ratio to the ground state is compared with results from statistical model calculations. The comparison revealed that the ground state decay is larger than estimated by the statistical model, supporting the interpretation of the PDR as a non-statistical structure from the previous literature. While statistical decays dominate the high-energy part of the PDR, the direct decays to low-lying states strongly depend on the nuclear structure and may play an important role for the low-energy part of the PDR. The main limitation of that work is the low sensitivity to weakly excited states.

In a subsequent experimental work on the same nucleus the first direct determination of the branching intensity to two different excited states was obtained, using a set up allowing to measure  $\gamma - \gamma$  coincidence with the  $(\gamma, \gamma')$  reaction [105]. The experiment allowed for the determination of the contribution from unresolved transitions to the measured cross sections. Averaged “branching ratio” were extracted from the data defined as the ratio of the averaged branching ratios between the decays to an excited state and that to the ground state. The averaging is taken with the experimental weight, that contains the photo-absorption cross sections of the states in the energy bin and the beam profile. It was possible with these data to get insight into the mixing of the pygmy resonance and of the pygmy resonance built on top of low-lying states. It was concluded that the PDR is mixed with the first  $2^+$  state at the level of approximately 10% and that this mixing is weaker for the other excited states at higher energy. This finding is shown in Fig. 17 together with the predictions within the QPM model, that were extended to provide transition widths to low lying excited states. One can see that the model prediction for the decay to the first excited  $2^+$  state is in very good agreement with the experimental data. These data provide an important test of the model because they lead to a clear indication that the coupling to complex configurations not only explains the fragmentation of the E1 strength but also describes with rather good accuracy transition probabilities to excited states.

The other investigated nuclei belonging to this mass region (such as  $^{139}\text{La}$  [93] and Xe isotopes) also show a significant enhancement of E1 strength in the energy range of 6 to 10 MeV. In the case of the  $^{139}\text{La}$  nucleus, measured at the ELBE laboratory, statistical (Monte-Carlo) simulations could not reproduce the data. The experiment for the  $^{136}\text{Xe}$  nucleus, the experiment used the High-Intensity Photon Setup DHIPS at the D-DALINAC laboratory [1,109]. As in all  $N = 82$  cases a fragmented resonance-like structure of E1 strength is observed in the energy region 5–8 MeV. In particular, it was observed that the degree of fragmentation decreases towards the proton-deficient isotones, while the total integrated strength increases, indicating a dependence of the total strength on the neutron-to-proton ratio. The prediction within the QPM model reproduced the fragmentation of the E1 strength and this has implications on the damping of the pygmy resonance. It has also to be underlined that the sensitivity limit of the existing experiments did not allow to observe the weak transitions produced by the high fragmentation of the strength and thus the integrated strength has to be considered and only in this way one could see the effect of an enhancement at larger neutron-to-proton ratio.

Interesting results concerning the role of deformation were found in the study of the electric dipole excitation in the  $^{142}\text{Nd}$  nucleus (see Ref. [96] with the experiment carried out using quasi-monoenergetic polarized gamma-beams at Hl $\gamma$ S). The direct ground state decay and the decay from seven low-lying excited states were detected and the reconstructed

photo-absorption cross section (including cascade decays but not including continuum) exhibits two bump structures peaking at 6.5 and 7.8 MeV, in the region where the pygmy dipole resonance is expected to exist. The two bump structure might be originated from the coupling of PDR to the deformation of the nucleus. For the  $^{142}\text{Nd}$  nucleus the photo-absorption cross section above the neutron separation energy was measured using the  $(\gamma, n)$  reaction at AIST, Tshukuba. The data were smoothly connected with the NRF data below the neutron separation energy. The  $(\gamma, n)$  data were found to be consistent with previous data from Saclay [110] only if the latter was scaled by a factor of 0.86 as recommended in B. L. Berman et al. [111]. In that work the ground-state branching ratio  $\langle b_0 \rangle$  as a function of the excitation energy was also deduced. It is important to stress that within the statistical model, the branching ratio for the excitation energy interval of 6–8 MeV could not be reproduced neither by modifying the level density assumptions nor the radiative strength function. The only way they found to reproduce the data is to assume the existence of a strength at around the 6–8 MeV that only couples to a state at 2–3 MeV, and does not have corresponding coupling to the ground state as suggested by the Brink hypothesis. This surprising result lead the authors to claim that the Brink hypothesis is violated for the radiative decay of the state in the energy region of pygmy resonance. However this could be due to structure effect. On the other hand, R. Schwengner et al. [101] claimed that this unusual observation might be due to the exclusion, in their analysis, of the continuum (unresolved strengths).

From the existing information it is clear that the problem on the origin of the coupling of pygmy states to specific low lying states needs further investigation and exclusive data are expected to be very useful.

### The mass region 180–210

The photo-absorption cross section of  $^{181}\text{Ta}$  was measured up to the neutron separation energy and the gamma-ray spectra were analyzed via statistical model calculations including levels in the quasicontinuum. The gamma strength function, the branching ratios, and the photo-absorption cross sections were deduced by fitting with an iterative procedure the observed gamma-ray spectrum (see [103] for details). The found strong decrease of the ground state decay branching ratio, going from 50% at 2 MeV to 3% at 7 MeV, was interpreted as due to the high level density for this odd  $A = 181$  nucleus.

The connection between the deduced photo-absorption cross sections, after correction by the branching ratio, and the existing  $(\gamma, n)$  data has a large gap at the neutron separation energy. The summed spectrum exhibits a peak at an excitation energy region of 7–8.5 MeV, that is speculated as PDR. However, because of the discontinuous connection between the  $(\gamma, \gamma')$  and  $(\gamma, n)$  data, one could not exclude that this is producing the bump-like shape around the “PDR” peak [78,104].

For the nucleus  $^{205}\text{Tl}$ , investigated by NRF at the DHIPS facility at S-DALINAC [109], the main result is the difference in the E1 strength below binding energy between even-even and even-odd isotopes. In addition, the QPM calculations failed to reproduce the group of  $1^-$  states at 4.9 MeV and reproduced instead the group of states at 5.5 MeV. Complementing measurement at HIγS shows that measurements with monoenergetic photon beams are needed in order to distinguish decays via intermediate states.

Extensive work was done for the  $^{204,206,208}\text{Pb}$  nuclei. The measurements at S-DALINAC (see [78] and [80]) found a resonance-like clustering of strength between 4 and 6.5 MeV. The fragmentation of the E1 strength was found to be increasing with the opening the neutron shell, and the strength was seen to be shifted to higher energies in the doubly magic  $^{208}\text{Pb}$ .

For the  $^{208}\text{Pb}$  nucleus a resonance structure centered around the neutron emission threshold was found. The complete E1 response could be extracted up to an excitation energy of 8 MeV by combining the available information on partial neutron and total decay widths. The comparison of the data with the QPM predictions indicates that the resonance could result from surface density oscillations of the neutron skin relative to the approximately isospin-saturated core. Another model was also proposed to explain these states as due to configurations in which the motion of the nucleons has a velocity distribution of toroidal type.

An interesting NRF measurement was made for the nucleus  $^{207}\text{Pb}$  [112]. The photon scattering reaction was used to understand the description of excitations in term particle–core coupled wave functions. This type of investigation was performed in several nuclei and in many cases the coupling of single particles to  $2^+$  and  $3^-$  states was identified by measuring energy splitting of the levels and lifetimes (see e.g. Ref. [113]). The presence of these states depends on how the core is robust against small perturbations (as in the case of nuclei with magic numbers). In the case of  $^{207}\text{Pb}$  one can test the competition between excited core states of  $1^-$  type and  $1\hbar\omega$  single-particle excitations at comparable energy. The result of the experiment performed to study core excitation of  $1^-$  type is shown in Fig. 18. The data show the presence of a doublet of energy levels of  $^{207}\text{Pb}$  that predominantly originates in the weak coupling of a  $\nu(3p_{1/2}^{-1})$  neutron hole to the strongest neutron-bound electric dipole excitation of the doubly closed shell  $^{208}\text{Pb}$  at 5.51 MeV. The energy splitting that was observed of the states in  $^{207}\text{Pb}$  with spin 1/2 and 3/2 is 107 keV (with the 3/2 state being the lower lying level), which is less than 2% of the energy of the  $1^-$  state in  $^{208}\text{Pb}$  at 5.51 MeV. The state at 5.51 MeV in  $^{208}\text{Pb}$  has an energy which is in reasonable agreement with the prediction of the hydrodynamical model which gives for the energy of a dipole vibration of the excess neutrons a behavior following the  $30 A^{-1/3}$  expression (see [114]). Therefore the states in  $^{207}\text{Pb}$  could be interpreted within this hydrodynamical model as states of the same type of that in  $^{208}\text{Pb}$  with the single particle coupled to it.

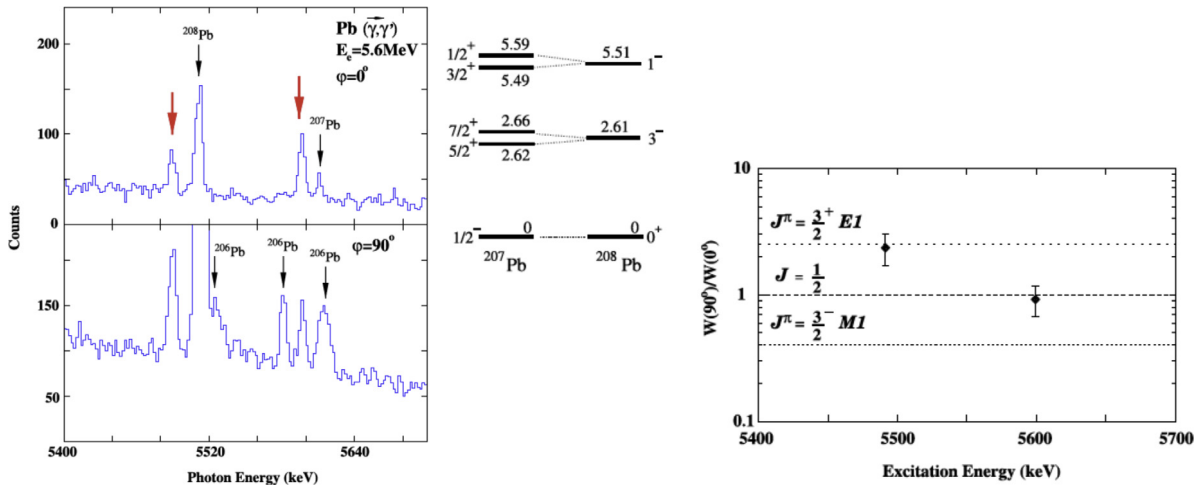


**Fig. 18.** Experimental data for the reaction  $(\gamma, \gamma')$  with an incident polarized beam for the nucleus  $^{207}\text{Pb}$ . The measured spectra at two detector angles (parallel and perpendicular to the beam direction) are on the left panels, the part of the level scheme of interest in the central panel and the parity assignment on the right panel.

Source: Adapted from [112].

### The mass region 240

In this mass region the most complete and recent study concerns the  $^{238}\text{U}$  nucleus. It was carried out at the HiS facility using 100% linearly polarized photon beams from 2.0 to 6.2 MeV [97]. In that experiment 113 gamma transitions to the ground state were observed. Energy, spin, parity, integrated cross section, reduced width, and branching ratio were obtained for each of the identified levels. It was found that 30% of the observed  $\gamma$ -rays correspond to M1 transitions, and the other 70% to E1 transitions. It was concluded that the observed concentration of low-lying E1 transitions are from the low-energy tail of the giant dipole resonance. Predictions by QRPA showed good agreement for the M1 strength but not similar agreement for the E1 strength. The data of the experiment reported in [97] are presented in Fig. 19. One can note that the strength of the transition in the region 4–6 MeV is different than the predictions for states of pygmy type. This can be seen in the right panel of Fig. 19. The data compared with the curve corresponding to standard Lorentzian (SLO) function show that there is no enhancement (the observed strength is smaller than the SLO curve). With the rescale factor by 0.85 of the Saclay data obtained above particle binding energy [110,111], the agreement with a SLO parametrization is enhanced.

## 4. Theoretical studies of low-lying isovector and isoscalar dipole states

### 4.1. Introductory overview

Since the first appearance of the locution “pygmy dipole resonance” on the late 60’s [115,116], there have been a lot of theoretical calculations to describe this new excitation mode, based in macroscopic as well as microscopic models. The incompressible three fluid model [114] (proton, neutron of the core, and the neutron excess) was developed on the same spirit of the Steinwedel–Jensen model [117]. In this macroscopic model the existence of the low-lying dipole state is found in a natural way, although the calculated strength of the PDR was too weak. An improved version of the model is given in Ref. [118] where only two incompressible fluids (the core and the neutron excess) were considered. In this case the strength of the pygmy resonance was in reasonable agreement with the experimental data available at that time [119]. Another macroscopic approach following the Goldhaber–Teller prescription [120], takes explicitly into account the neutron skin [121]; they found that the ratio of the PDR to the GDR sum rule is similar to the one obtained in Ref. [118]. More recently, a macroscopic model where the nucleus is considered as a spherical piece of elastic continuous medium [122] has investigated the PDR in terms of elastodynamics excitation mechanism implying then the isoscalar nature of the state. From the point of view of the microscopic approaches early calculations have shown the strong relation between the neutron excess and the increasing of the low lying dipole strength [123]. Several microscopic many-body models have been extensively studied the low lying dipole mode (see Ref. [6] and references therein). The Hartree–Fock plus random phase approximation (RPA) with Skyrme interactions gives a good description of the internal structure for spherical and shell closed nuclei. The description of open shell spherical and deformed nuclei implies the inclusion of pairing correlation which has to be treated together with the mean field correlation. This is well achieved employing the Hartree–Fock–Bogoliubov (HFB) theory plus the Quasi-Particle RPA (QRPA) with Skyrme or Gogny effective interactions. A

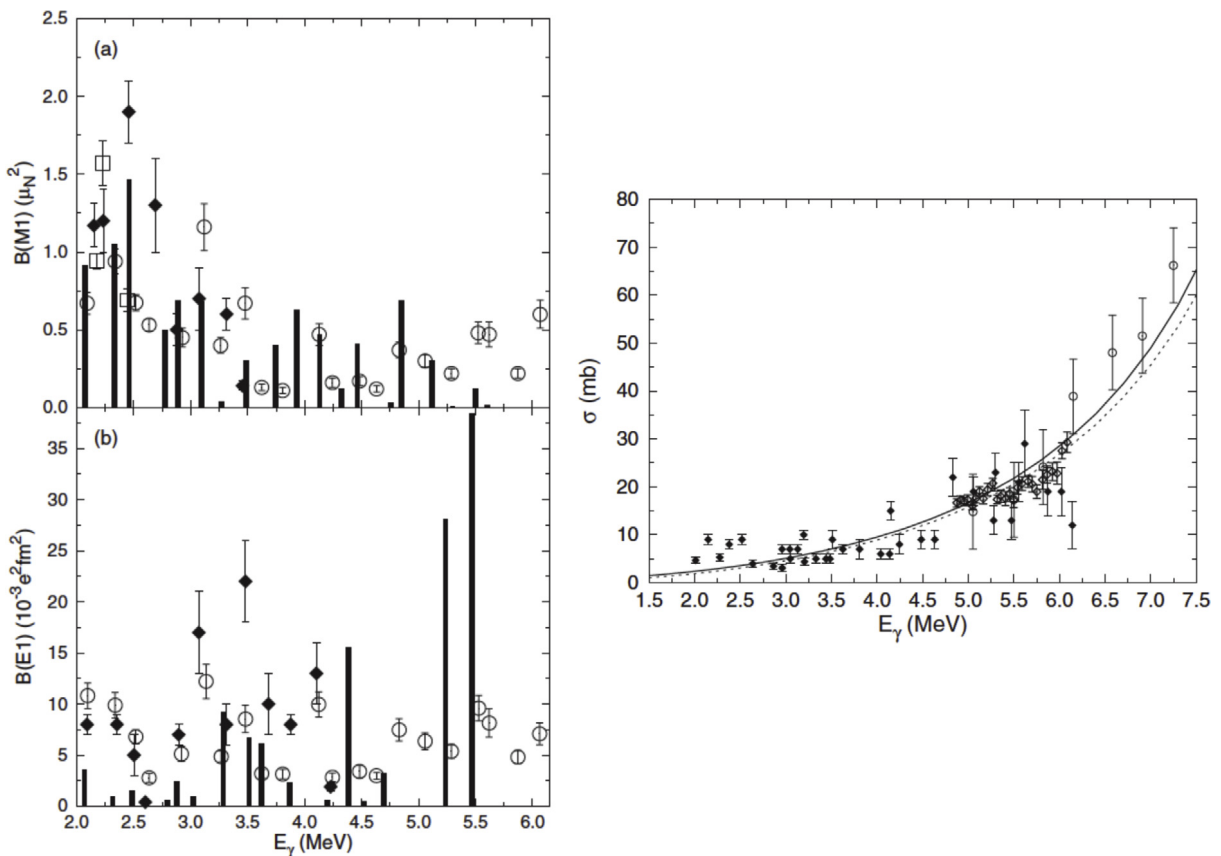


**Fig. 19.** Experimental data for the reaction  $(\gamma, \gamma')$  with an incident polarized beam for the nucleus  $^{238}\text{U}$ . In the left panels the experimental (a) M1 and (b) E1 strengths from discrete transitions and from the continuum of states are given. Calculations of QRPA type are shown with bars with a 0.2 MeV bin size. On the right panel the total  $\gamma$  ray interaction cross section for E1 transitions both discrete and unresolved. The fit to the data with a standard double Lorentzian (dashed curve) and a modified double Lorentzian (solid curve) for the GDR are also shown.

Source: Figures taken from [97].

good account of several nuclear structure phenomena is accomplished by the relativistic RPA (RRPA) [124–128] where the nucleus is described as a system of nucleons coupled with meson and electromagnetic field. A relativistic quasi particle RPA (RQRPA) [129–131] is appropriate for the description of collective excitations in open shell nuclei. These relativistic mean-field models have acquired a level of precision and complexity similar to the non relativistic ones. These mean field theories account for many of the physical properties of the collective excitations for stable nuclei as well as for nuclei far from the stability line. But, some aspects of the collective excitation, where the nuclear structure around the Fermi surface is important, are not well interpreted. Namely, the description of collective states as coherent superposition of one particle, one hole (1p-1h) or quasi particle states is not sufficient. The contribution of more complicated configurations, like 2p-2h, 3p-3h, ..., have to be included in order to get a good description of experimental features. The coupling of simple 1p-1h to more complicated configurations, due to the residual interaction, is easily realized when the Hamiltonian is diagonalized in a configuration space which includes 2p-2h or 3p-3h contribution. For instance in Ref. [132–134], the collective RPA states are used as a basis to construct all the possible two- and three phonon states of several multipolarities to build up the space where the bosonic Hamiltonian is diagonalized. In the so called second RPA (SRPA) the main feature of the RPA are maintained and the contribution of the 2p-2h states are taken explicitly into account [135–137]. Several theoretical approaches are based on the particle-vibration coupling model which takes into account the fact that the nucleons are strongly coupled with the nuclear surface oscillations associated to the collective excitation. As an example one can quote the Extended Theory of Finite Systems (ETFFS) [138]. The model which has been used with great success for giant resonances as well as for low lying states description is the so called quasi particle-phonon model (QPM) [139,140]. In this model the phonon are constructed from the solutions of the QRPA and the coupling to one up to three phonons are taken into account. In these calculation one can get the fragmentation of the one phonon states due to their coupling with higher configurations. This is particular important for the low lying dipole states where, at energies below the neutron emission threshold, experimentally a large fragmentation has been found. A good description of the structure of the states in the PDR region is obtained also within the Relativistic Quasi-particle Time Blocking Approximation (RQTBA) [141–144] where the quasi-particle-phonon coupling is taken into account.

The results of the calculations of all these models give the same answer for the main characteristic of the PDR like the fact that the peak of the dipole strength distribution showing at low energy are seen in nuclei with  $N > Z$  and they are generated by the excitation of the neutron excess. More important, they have been proved to have a strong mixing of isoscalar and isovector character. The presence of a strong peak at low energy in the isoscalar strength distribution, beside the one at high energy corresponding to the well known isoscalar GDR (ISGDR), has motivated further experimental and theoretical investigation. A full comprehension of this phenomenon is still missing although there are calculation able to reproduce it. In particular the particle-vibration coupling model, like the QPM and the RQTBA, have shown the importance of introducing the coupling to one, -two- and three-phonons which turn out to be essential in reproduce most of the experimental findings.

Several works are aimed to show that the PDR can be treated as a manifestation of the Toroidal Dipole Resonance (TDR) [145–147]. They appear at the same energy region and therefore it was suggested that the PDR may be a peripheral manifestation of the TDR although these are irrotational and vortical kind of nuclear motion. The PDR manifests in nuclei with  $N > Z$  while the TDR is present in all nuclei; their claim is that the PDR is a complicated mixture of different kind of dipole motion.

The interpretation of the results of the pygmy dipole strength obtained in the large number of experiments using electromagnetic excitation was mainly obtained by using models based on the phonon coupling which are described above. These models were very successful and predicted also excitation of isoscalar type at about the same energy interval. The experimental works with their results are discussed in Sections 3.2 and 5.

The main feature characterizing the predictions for the low energy dipole excitation of isoscalar and isovector type is in the shape of transition density. To compare data with predictions it is important to use in the calculation of the cross section the transition densities deduced from microscopic calculations. This point is also an important content of this section.

Much more details about the many body model quoted above can be found in the review paper of Paar et al. [6]. Here we will concentrate to the different response that the low-lying dipole states have when investigated by different probes. In particular we will try to put in evidence some characteristics that can be useful to take into account when analyzing the experimental data.

#### 4.2. The dipole strength distribution

In this section we present the dipole strength distributions focusing in particular on the closed shell isotopes of the Ca, Ni, Zr and Sn and Pb nuclei. The calculations here presented have been done with a self-consistent Hartree–Fock plus Random Phase Approximation (HF+RPA) [148] with a spherical symmetry assumption which is applied when the pairing correlation and deformations can be ignored. The Skyrme-type interaction used in the calculations was the SGII interaction [149]. The calculations were performed by putting the maximum energy of the unoccupied single-particle states included in the RPA model space equal to 100 MeV. More details about the RPA calculations can be found in Ref. [148]. We calculate the electromagnetic and isoscalar dipole response in the long wavelength limit by using the following operators:

$$\hat{O}_{1m}^{EM} = \frac{eN}{A} \sum_{i=1}^Z r_i Y_{1m}(\hat{r}_i) - \frac{eZ}{A} \sum_{i=1}^N r_i Y_{1m}(\hat{r}_i); \quad (8)$$

$$\hat{O}_{1m}^{IS} = \sum_{i=1}^A (r_i^3 - \eta r_i) Y_{1m}(\hat{r}_i), \quad (9)$$

where the effective charge for protons ( $\frac{eN}{A}$ ) and neutrons ( $\frac{eZ}{A}$ ) have been introduced to remove the spurious center of mass motion. The isoscalar dipole operator has been modified by introducing the term with  $\eta = 5\langle r^2 \rangle / 3$  to eliminate the contribution from the center of mass. The discrete dipole strength distributions have been folded with a Lorentzian and the results are reported in Fig. 20. The reason of the folding is to simulate the realistic spreading of the strength distribution. For the Sn isotopes this was best achieved with a smaller width. In the upper part of the four set of figures there are shown the dipole electromagnetic folded strength distributions for several isotopes of the Ca, Ni, Zr and Sn nuclei. The isoscalar response for the same isotopes are shown in the lower parts. We note that, for both isovector and isoscalar response, as soon as the neutrons number increases, a major strength moves to lower energies, as was already noted in previous calculations [123]. The population of low lying dipole states is due to the neutron excess as it is shown also from an inspection of the particle-hole (p-h) structure of the RPA single dipole states. In fact, most of the p-h contributions comes from the neutron belonging to the outmost shell (see Section 4.5). Beside of the IVGDR peak between 15 and 20 Mev, one can appreciate the prominent peak of the ISGDR at about 30 MeV whose strength seems to grow up with the increasing neutron number.

Useful information can be obtained from Fig. 21 where the sum of the reduced transition strength is plotted as function of the mass number for some isotopes of Ca, N, Zr and Sn nuclei. The sums have been performed taking the discrete states coming from the RPA calculations rather than the folded ones to avoid to sum up the contribution of the tails of the states of higher energies. The choice of the energy range, shown in the figure, is not straightforward and the change of 1 MeV

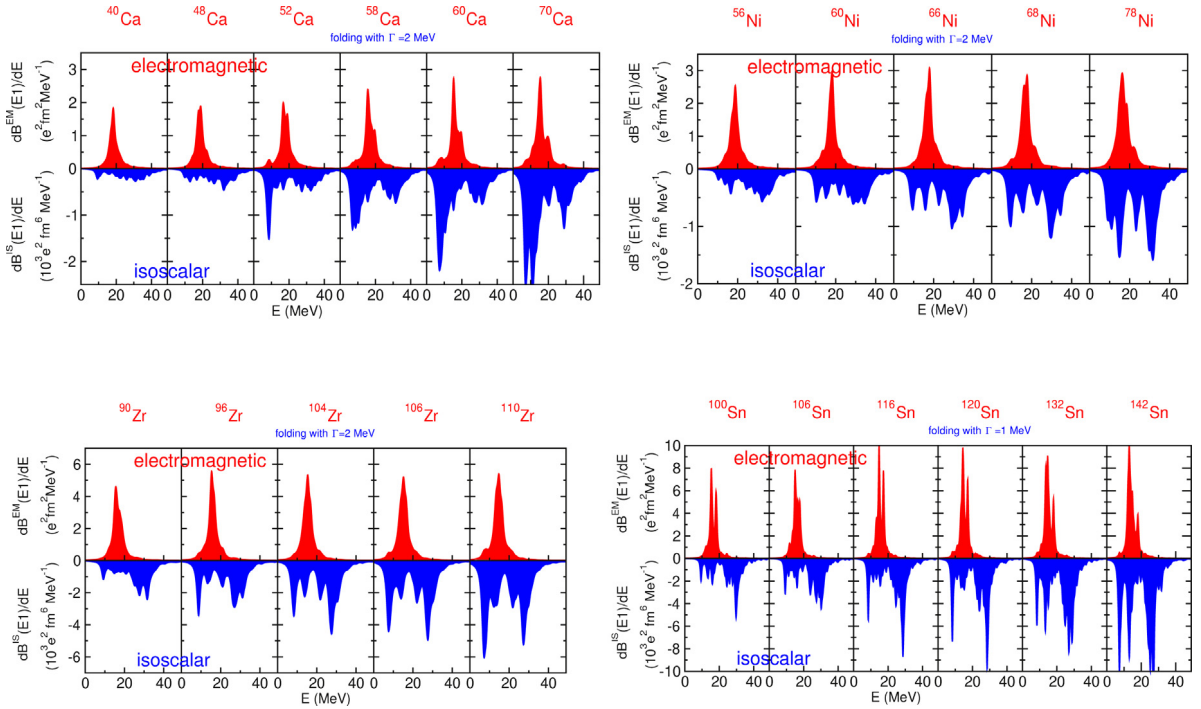


**Fig. 20.** Isovector and isoscalar dipole strength distribution for several isotopes of  ${}^A\text{Ca}$ ,  ${}^A\text{Ni}$ ,  ${}^A\text{Zr}$  and  ${}^A\text{Sn}$ . The calculations have been done with a discrete self-consistent HF plus RPA code with a SGII interaction. The continuous curves are obtained by a smoothing procedure using a Lorentzian with a width of 1 or 2 MeV. The electromagnetic responses are shown in the upper part (in red) while the isoscalar responses are shown (in blue) in the lower part.

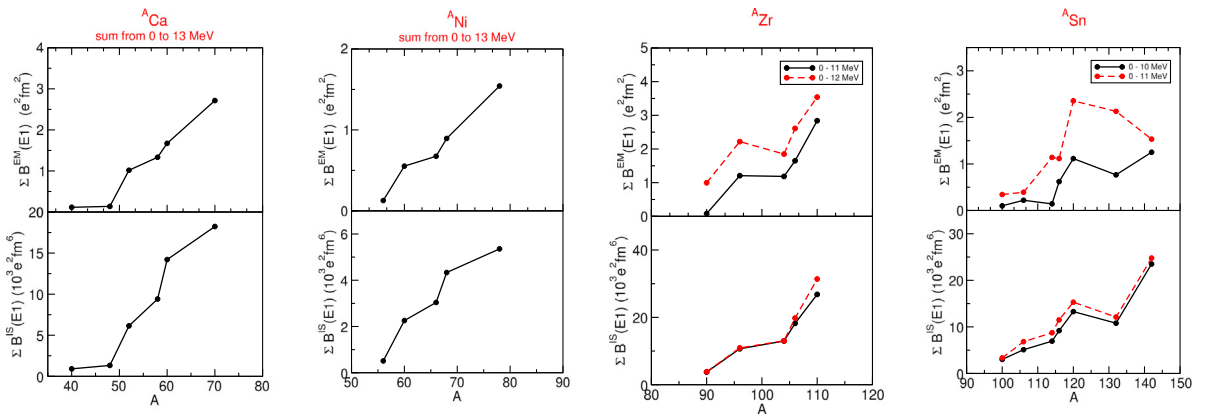


**Fig. 21.** Sum of electromagnetic (upper panels) and isoscalar (lower panels) dipole strength as a function of the mass for several isotopes of  ${}^A\text{Ca}$ ,  ${}^A\text{Ni}$ ,  ${}^A\text{Zr}$  and  ${}^A\text{Sn}$ . The sums have been performed for the energy interval shown in the figure. The continuous curves are drawn to guide the eyes.

can produce sometimes very different results as one can appreciate for the case of the electromagnetic dipole of Zr and Sn. This depends on the fact that for these isotopes the level densities are higher than the lighter nuclei and the separation between the region of the PDR and GDR is less evident. The integration ranges have been chosen in order to include all the states belonging to the PDR peak whose position is slowly changing with the increasing of the atomic number. On the contrary there is no appreciable difference for the isoscalar case. Anyway one can surely say that both isoscalar and isovector strengths increase, although not linearly, with the increasing of the neutrons number. Furthermore, the occurrence of strong rise followed by a very small increase, or in some case decrease, is probably an indication of some shell effects as already noted in Ref. [150]. This behavior can be ascribed to the low density of the states in this energy region.

A distinct behavior is shown, for the case of the sum of the strength of the ISGDR, in Fig. 22 where the sum is plotted as function of N-Z for the four nuclei considered. The sum was performed over an energy interval from 22 to 40 MeV for

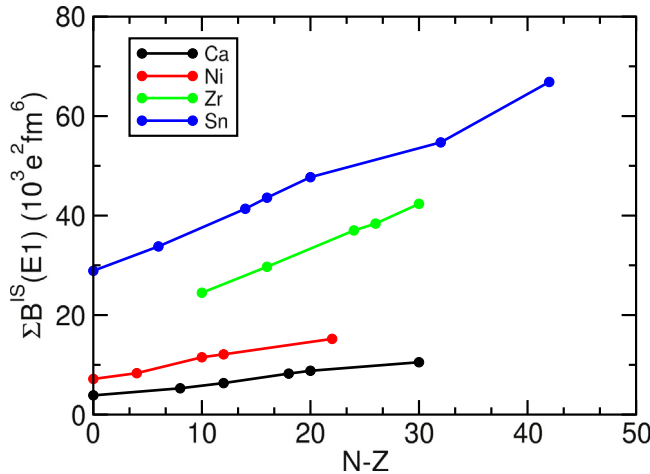


**Fig. 22.** Sum of isoscalar dipole strength for the ISGDR region as a function of the N-Z for several isotopes of  ${}^A\text{Ca}$ ,  ${}^A\text{Ni}$ ,  ${}^A\text{Zr}$  and  ${}^A\text{Sn}$ . The sums have been performed for the energy interval between 22 and 40 MeV for Ca and Ni, and from 20 to 38 MeV for Zr and Sn. The continuous curves are drawn to guide the eyes.

Ca and Ni isotopes, and from 20 to 38 MeV for the Zr and Sn isotopes. These different energy ranges are due to the fact that as far as the mass of the nuclei is increasing the ISGDR peak is moving down as one can appreciate from Fig. 20. One can clearly note an almost perfect linear trend for all the considered cases with no apparent shell effect due to the fact that at high energy the density of the states is higher.

Recently, similar analysis regarding the low lying dipole strength distribution have been done using different mean field approaches as well as several effective interactions. No different results have been obtained in Ref. [151] where a QRPA calculations with three different Skyrme interaction and pairing interaction have been done for several isotopes of Ca, Ni and Sn isotopes. They also find an enhancement of the low lying dipole strength as the neutron drip line is approached as well as a decreasing in energy of the peak for increasing neutron number. A very detailed analysis on the same isotopes has been undertaken with particular attention to the isoscalar low lying dipole states in the work of Papakostantinou et al. [150,152,153]. The calculations have been done with a HFB plus QRPA with a Gogny DS1 finite range interaction and a quasi realistic interaction, namely an Argonne V18 plus a phenomenological three body contact term. They also used a continuum RPA with a SLy4 interaction. They found significant strength at low energy for the isoscalar response, the peak moving at low energy with the increase of neutron excess. They argued that the pygmy dipole strength is strongly influenced by the shell effects.

#### 4.3. Isovector and isoscalar dipole transition densities

A deeper insight on the nature of the different responses of the states in the three energy regions, namely the ones corresponding to the PDR, IVGDR and ISGDR that one can distinguish in the strength distribution, can be obtained by looking to the shape of the transition densities. The microscopic transition densities are commonly determined with the wave function and the X and Y amplitudes coming from a HF plus RPA calculation type. The explicit expression we use can be found in Eq. (B.37) of Ref. [154]. Nuclei with  $N=Z$  show no significant strength at low energy in the isovector response while there is, for all the isotopes, an important contribution for the isoscalar response. The states belonging to this region are quite different depending whether the nuclei have  $N=Z$  or  $N>Z$ . The transition densities in Fig. 23 show clearly the different nature of these states. On the left frames, the proton and neutron transition densities for the dipole state at  $E=12.10$  MeV of the  ${}^{56}\text{Ni}$  are completely in phase both inside the nucleus and at the surface. Consequently, the isovector transition density is almost null while the isoscalar one shows the typical shape of a pure compressional mode (left lower frame of Fig. 23). On the other hand, the transition densities for the low lying state at  $E=10.41$  MeV of the  ${}^{68}\text{Ni}$  isotope (right side of Fig. 23) show the typical behavior of the PDR: neutron and proton in phase inside the nucleus while only the neutron give a contribution on the surface. Consequently, the isoscalar and isovector transition densities have the same magnitude on the nuclear surface which is the region giving the major contribution when the excitation is produced via an isoscalar probe. The discussion above refers to two particular states of the low-lying energy region. In particular, the PDR peak of  ${}^{68}\text{Ni}$  is formed by several dipole states and their transition densities do not have the same form as the one in Fig. 23. However, these shapes are common to the states which have a bigger isovector EWSR so these can be considered as representative of this region. Indeed, if one try to bunch together the states belonging to the PDR peak as it is often done for the cross section calculations [155,156], the resulting transition density results to have the same properties of the one shown in the right part of Fig. 23 (see Refs. [155,156]). This bunching procedure consists in taking as energy the average energy of the states belonging to the group with the condition that the EWSR must be preserved [155,156]. The

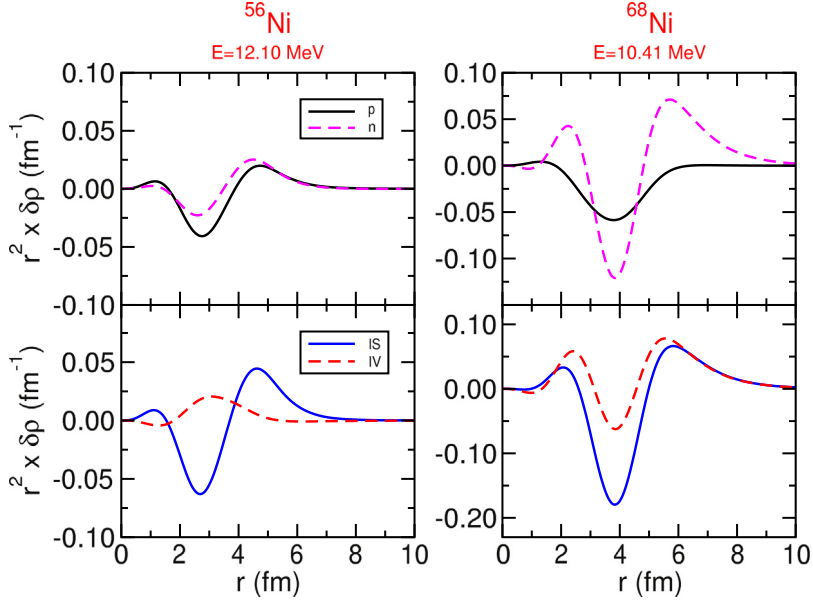


**Fig. 23.** Transition densities for the low lying dipole state of  $^{56}\text{Ni}$  and  $^{68}\text{Ni}$ . In the upper part there are plotted the proton (solid black line) and neutron (magenta dashed line) transition densities while in the lower frames the isovector (solid blue line) and isoscalar (red dashed line) ones. The left part refers to  $^{56}\text{Ni}$  while the right part to  $^{68}\text{Ni}$ .

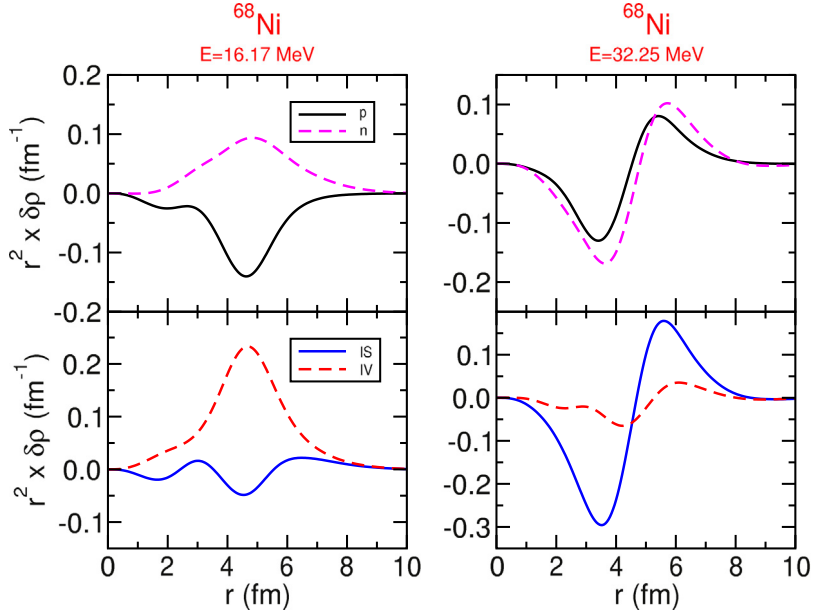


**Fig. 24.** Transition densities for the states belonging to the peak of the IVGDR and ISGDR of  $^{68}\text{Ni}$ . In the upper part there are plotted the proton (solid black line) and neutron (magenta dashed line) transition densities while in the lower frames the isovector (solid blue line) and isoscalar (red dashed line) ones. The left part is for the IVGDR while the right one is for ISGDR.

features of the transition densities shown in Fig. 23 are common to all the RPA-like calculations quoted in the introduction of this section. These properties, namely neutron and proton transition densities in phase inside the nucleus while only the neutron give a contribution on the surface, provide a kind of theoretical definition of the PDR. These characteristics allow the possibility to experimentally explore these states with both isoscalar and isovector probes. In addition, if one

takes into account the coupling with one- or two-phonon states then the PDR peak spreads out in many more states [157]. Calculations done with the particle-phonon model (QPM) and the Relativistic Quasi-particle Time Blocking Approximation (RQTBA) have shown that in the lower part of the PDR energy region the transition densities still show a behavior similar to the one in Fig. 23 (see for instance Refs. [20,95,158]).

The unicity of the feature of the PDR is further evidenced when it is put in comparison with the other two very well known dipole collective modes. The transition densities for the isovector and isoscalar giant dipole resonances are plotted in Fig. 24. There, one can appreciate the almost pure isovector property of the IVGDR; indeed, the proton and neutron transition densities in the upper frame of the left part of the Fig. 24 are symptomatic of an out of phase oscillation of protons against neutrons, according to the macroscopic description of the IVGDR. Conversely, for the ISGDR (on the right side of Fig. 24) the proton and neutron transition densities are in phase in all the nuclear region giving rise to a strong isoscalar transition density typical of the compressional modes.

Such strong differences among the states of the three different energy regions of the dipole strength distribution have strong consequences in the excitation process especially when an isoscalar probe is used. In fact, in such cases the region explored in the nuclear excitation is around the nuclear surface where most of the differences among the three states are concentrated. One of the most important ingredient entering in the calculation of the inelastic cross section is the radial form factor which contains the structure effects and depends on the various model employed for the description of the inner structure of the nuclei. In subsection 4.4 it will be shown that the form factor constructed via a double folding procedure are very sensible to the shape of the transition densities employed [159], especially in the region around the nuclear surface. Therefore it is of paramount importance the choice of a transition density which describe all the details of the state taken into consideration.

The transition densities play a very important role in the construction of the form factor. Beside the microscopic way described above there are several way to build them within macroscopic model like vibrational or rotational collective model [160]. In particular the collective vibrational modes are considered as high frequency and almost harmonic oscillations of the nuclear surface and therefore they are often associate to the deformation of the density, usually described in terms of the derivative of the ground state density. Consequently one can deduce the macroscopic form factors which can be expressed in terms of the derivative of the optical potential which governs the elastic scattering of the colliding nuclei. The inelastic excitation process of most of the collective states can be well described by these macroscopic form factors except for the dipole and monopole modes [3,154,161]. Indeed, for the Isovector Dipole Giant Resonance (IVGDR), which is considered generated by an out of phase oscillation of neutron against protons, one has to take care of the center of mass motion which gives rise to a spurious state and does not correspond to a real excitation of the nucleus. For this mode specific models have been formulated to take into account this aspect. The Steinwedel and Jensen model [117] assume that the oscillations happen maintaining the nucleons within a rigid sphere, while the Goldhaber and Teller [120] model allows the rigid sphere of protons and neutrons to vibrate one against the other. In the latter model the spurious center of mass motion is taken into account by scaling in a proper way the proton and neutron transition densities [162–164]:

$$\delta\rho_p(r) = -\delta_1 \frac{2N}{A} \frac{d\rho_p}{dr}; \quad \delta\rho_n(r) = -\delta_1 \frac{2Z}{A} \frac{d\rho_n}{dr}, \quad (10)$$

where  $\delta_1$  is the so called deformation length and  $\rho_p$  ( $\rho_n$ ) are the proton (neutron) densities. The transition densities are scaled according to the ratio of neutron (N) and proton (Z) number with the total nucleons number (A). If the proton and neutron densities have the same radial form, that is their ratio is equal to  $N/Z$ , then the isoscalar transition density is zero. This is expected to be a good approximation for nuclei with  $N = Z$ , however when  $N > Z$  the proton and neutron densities may have different radial shapes producing an isoscalar transition densities different from zero and therefore making possible an excitation of the isovector GDR by an isoscalar probe. Indeed, expanding it in the neutron excess parameter, according to Satchler [162], the isoscalar transition density for the GDR state can be written in the form

$$\delta\rho_{GDR}^{IS}(r) \approx \delta_1 \gamma \left( \frac{N-Z}{A} \right) \left[ \frac{d\rho(r)}{dr} + \frac{R_0}{3} \frac{d^2\rho(r)}{dr^2} \right] \quad (11)$$

where  $R_0 = (R_n + R_p)/2$  is the average radius of the total nuclear density  $\rho(r)$  and the parameter  $\gamma$  is related to the measure of the neutron skin  $\Delta R = R_n - R_p$  by the relation  $\gamma(N - Z)/A = 3/2 (\Delta R/R_0)$  [123]. The isoscalar transition density is therefore, to leading order, directly proportional to the size of the neutron skin.

A  $3\hbar\omega$  nuclear transitions generated by the second order  $\Delta L = 1$  transition operator give raise to the Isoscalar GDR. For this mode, which can be seen as a compressional one, a macroscopic collective model has been employed for its description [165,166] where a macroscopic collective transition density has been extracted from the isoscalar dipole sum rule. Assuming that the isoscalar dipole energy weighted sum rule is fully exhausted by a single collective state, the corresponding isoscalar transition density, as deduced by Harakeh and Dieperink (HD), is [166]

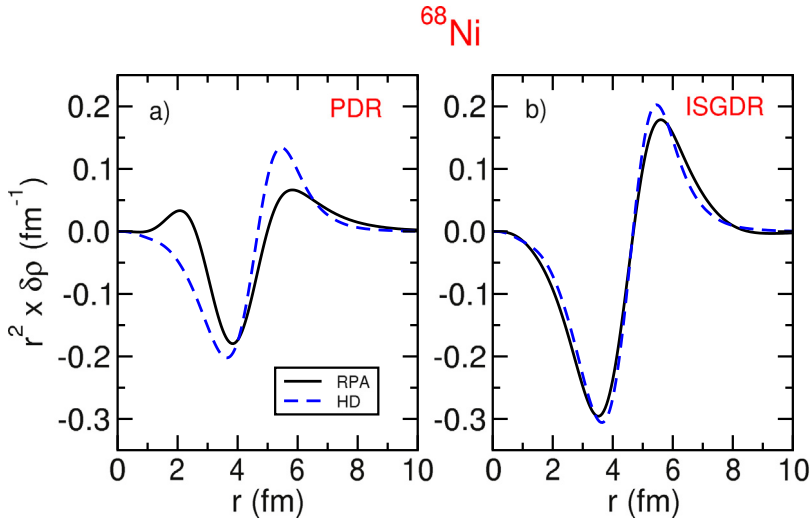


**Fig. 25.** Comparison between the isoscalar microscopic (RPA) transition densities (solid black line) and the one calculated according to Eq. (12) (HD) (blue dashed line) for two dipole states of  $^{68}\text{Ni}$  (the ones in the right frame of Figs. 23 and 24). On the left frame are shown the isoscalar transition densities corresponding to the PDR state, while in the right frame the ones for the ISGDR. Source: Adapted from [159].

$$\delta\rho^{HD}(r) = -\frac{\beta_1}{R\sqrt{3}} \left[ 3r^2 \frac{d}{dr} + 10r - \frac{5}{3} \langle r^2 \rangle \frac{d}{dr} + \epsilon \left( r \frac{d^2}{dr^2} + 4 \frac{d}{dr} \right) \right] \rho_0(r) \quad (12)$$

where the coupling parameter  $\beta_1$  is

$$\beta_1^2 = \left( \frac{6\pi\hbar^2}{mA E_x} \right) \frac{R^2}{(11\langle r^4 \rangle - \frac{25}{3}\langle r^2 \rangle^2 - 10\epsilon\langle r^2 \rangle)} \quad (13)$$

with

$$\epsilon = \left( \frac{4}{E_2} + \frac{5}{E_0} \right) \frac{\hbar^2}{3mA}$$

$E_2$  and  $E_0$  being the giant quadrupole resonance and giant monopole resonance excitation energies, respectively. The distance  $R$  is the half-density radius of the mass distribution. The transition density expression contains the center of mass correction and the terms containing  $\epsilon$  may be disregarded for nuclei with  $A \geq 40$ . It is straightforward to show that the condition of translational invariance ( $\int \delta\rho^{HD}(r)r^3 dr = 0$ ) is satisfied.

In order to compare the macroscopic HD transition density with the microscopic RPA one, one has to normalize the two. Because of the translational invariance condition the normalization is given by imposing the following equality

$$\int \delta\rho^{RPA}(r)r^5 dr = \int \delta\rho^{HD}(r)r^5 dr \quad (14)$$

The calculation was done for the nucleus  $^{68}\text{Ni}$  and the same ground state density (HF with the SGII interaction) employed for the RPA calculations has been used to build up the  $\delta\rho^{HD}$  [159]. The microscopic RPA isoscalar transition density is compared, in Fig. 25, with  $\delta\rho^{HD}$  for the two dipole state PDR and ISGDR of  $^{68}\text{Ni}$ , the same shown in the right frames of Figs. 23 and 24. In panel (b) of Fig. 25, the transition densities for the ISGDR is shown for the two different calculations. The transition densities calculated with the approach followed in Ref. [166] is almost identical, after normalization, to the RPA one. As stated before, they show the typical pattern of a compressional mode with a node in the interior of the nucleus.

On the other hand, the low lying dipole state shows some difference especially at the nuclear surface region where the peak of the  $\delta\rho^{HD}$  is too high with respect to the RPA one and it goes down a bit faster, see panel (a) of Fig. 25. The differences can be ascribed to the fact that, as it was shown before, the PDR has a strong isovector component which, by construction, is not present in the transition densities build up in Ref. [166]. So if one adopt the latter prescription for the PDR state one is implicitly assuming that the pygmy state is a pure isoscalar state which is in contradiction to what has been found in many theoretical many body calculations. Moreover these differences will manifest in a clear manner in the radial form factor constructed with these transition densities and consequently in the calculated cross section. In most of the experiments with isoscalar probes the extraction of information about the strength and the relative EWSR percentage

is based on cross section calculations which depend very much on the models used for the inelastic form factor. Therefore the use of proper form factor is of paramount importance in the deduction of these physical quantities.

#### 4.4. Nuclear form factor of the low lying dipole states

The study of the inelastic nuclear excitation can be performed within different approaches. The most common is the Distorted Wave Born Approximation (DWBA), a first order theory employed when a single step excitation from the ground state is considered to be the relevant excitation process. The underlying assumption is that the elastic scattering is thought to be the most important process and the inelastic excitation is considered as a perturbation. When higher order effects are important, like the strong coupling to other states outside the one taken into account, then one has to take them in consideration and therefore the coupled channel model has to be employed. Beside these full quantal calculations, semiclassical models have been developed and used for the description of heavy ion collision and inelastic cross section calculations. In these models it is assumed that the time evolution of the two nuclei can be described according to the classical equations of motion. This description is plausible when the De Broglie wave length associated with the incident nucleus is small with respect to characteristic magnitude of the process. These conditions are usually satisfied in heavy ion collisions. Therefore, in these cases, the Schrödinger's equation can be cast into a semiclassical coupled channel equations for the time dependent probability amplitudes of the channels wave function (for more details see Refs. [155,156]). In all these approaches, one of the most important ingredient is the determination of the form factors. For instance, the transition amplitude for the DWBA can be written as

$$T^{DWBA} = \int \chi^{(-)}(k_\beta, \vec{r}) F(\vec{r}) \chi^{(+)}(k_\alpha, \vec{r}) d\vec{r}, \quad (15)$$

describing the nuclear reaction from channel  $\alpha$  to channel  $\beta$ . The distorted wave functions  $\chi$  are generated solving the Schrödinger's equation with an optical potential which fits the corresponding elastic scattering cross section. The form factor  $F(\vec{r})$  contains, in this approach, all the structure effect of the nuclear process. The form factors can be constructed within various model of nuclear structure which can be tested by comparing the deduced inelastic cross sections with the experimental ones. They are usually derived either within a macroscopic collective model or in a microscopic approach. One of the most powerful and well founded way to construct a microscopic form factor is by using the well known double folding procedure [160,161]. This method is often used to construct the double folding potential between two heavy ions by integrating the nucleon–nucleon interaction over the densities of the two nuclei. In a similar way the form factors are constructed by using the density of one nucleus on one side and the transition densities of the excited nucleus on the other side. A microscopic neutron and proton transition densities can be calculated by means of many body model like HF plus RPA as shown in Section 4.3. For the nucleon–nucleon interaction one should include the isospin dependent part

$$v_{12} = v_0(r_{12}) + v_1(r_{12}) \boldsymbol{\tau}_1 \cdot \boldsymbol{\tau}_2 \quad (16)$$

where the isoscalar part  $v_0$  generates an isoscalar ion–ion potential and the isovector term  $v_1$  gives an isospin dependent folding potential; here the  $\tau_i$ 's are the isospin of the nucleons. With this choice also the form factors have two components with the following expression

$$F_0 = \int \int [\delta\rho_n^A(r_1) + \delta\rho_p^A(r_1)] \times \\ v_0(r_{12}) [\rho_p^B(r_2) + \rho_n^B(r_2)] r_1^2 dr_1 r_2^2 dr_2 \quad (17)$$

$$F_1 = \int \int [\delta\rho_n^A(r_1) - \delta\rho_p^A(r_1)] \times \\ v_1(r_{12}) [\rho_n^B(r_2) - \rho_p^B(r_2)] r_1^2 dr_1 r_2^2 dr_2 \quad (18)$$

where the  $\delta\rho_i$  ( $i = n, p$ ) are the transition densities of the state under study of nucleus  $A$  which is excited by the mean field of nucleus  $B$ . In the particular case when  $\rho_n/\rho_p = (N/Z)$ , then the form factor (18) is zero when one or the two partner of the reaction have  $N = Z$  [161]. For the calculations presented in the following, the M3Y nucleon–nucleon interaction, Reid type [167], whose explicit expressions can be found in Ref. [160], has been used for  $v_0$  and  $v_1$ . This interaction is not density dependent and it has been successfully employed for the description of several cases of elastic and inelastic reactions. The implementation of a density dependence shows that the obtained potential are almost not distinguishable. Some differences among the corresponding potential is present when different density dependence are taken into account. However, these differences are in the interior part of the nucleus while at the surface the potentials are practically identical [168,169]. Since in the reactions studied here only the peripheral region of the two colliding nuclei is explored, therefore the use of the density independent interaction seems to be well justified.

The nuclear form factors were calculated with the double folding procedure with the two transition densities described in Section 4.3 [159]. The calculation are done in the momentum-space making use of the Fourier transform because the calculation with this method is fast and convenient [160]. The results for the two states PDR and ISGDR are reported in

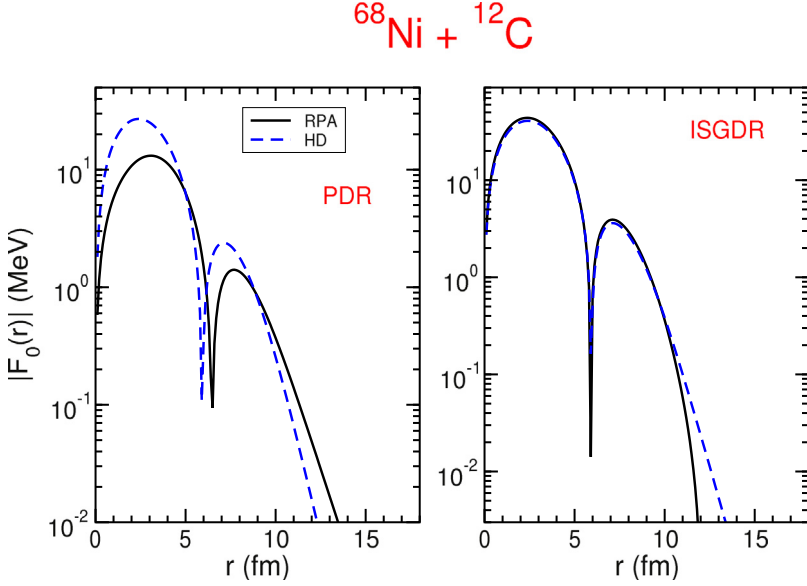


**Fig. 26.** Form factors for the system  $^{68}\text{Ni} + ^{12}\text{C}$  for the PDR state (left frame) and for the ISGDR (right frame). All of them are calculated with the double folding procedure but with different transition densities: the solid black line refers to the microscopic RPA transition densities, the blue dashed line to the HD ones.

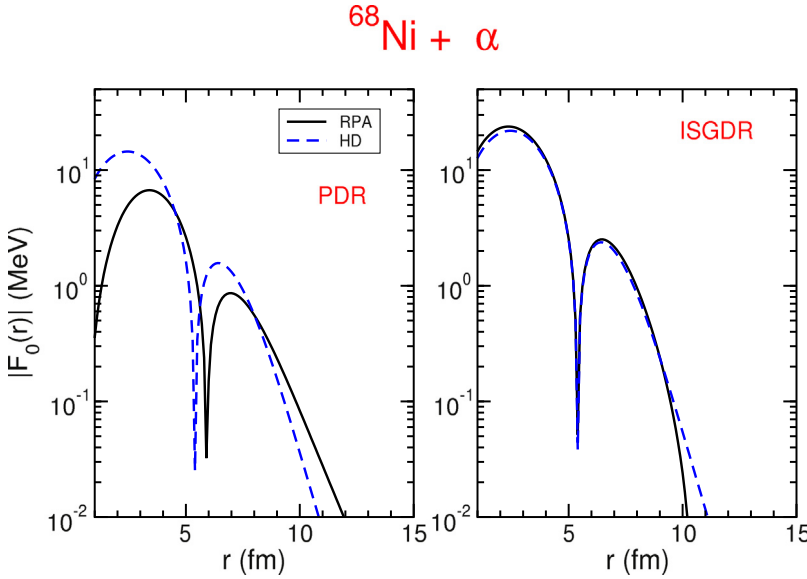


**Fig. 27.** Same as Fig. 26 but for the system  $^{68}\text{Ni} + \alpha$ .

**Fig. 26** for the system  $^{68}\text{Ni} + ^{12}\text{C}$  whose experimental results are recently available [39]. For the ISGDR state, right frame of Fig. 26, the microscopic nuclear form factor (solid black line) and the one calculated with the Harakeh and Dieperink (HD) transition densities (blue dashed line) are almost identical in all the significant distance range. Some difference can be appreciate in the very peripheral region but this will not have any effect in the cross section calculations. Conversely, strong differences are evident in the case of the PDR state. In the left frame of Fig. 26, the blue dashed line, corresponding to the HD form factor, is entirely different from the microscopic one (black solid line) both in the intensity and especially around the most important surface region. Identical behavior can be found in Fig. 27 where the  $\alpha$  particle is used as isoscalar probe as it has been often employed in many experimental investigations.

As stated above, the inelastic cross section can be calculated following several approaches. We have done DWBA calculations for the system  $^{68}\text{Ni} + ^{12}\text{C}$  at 10 MeV/u with the code DWUCK4 [170].

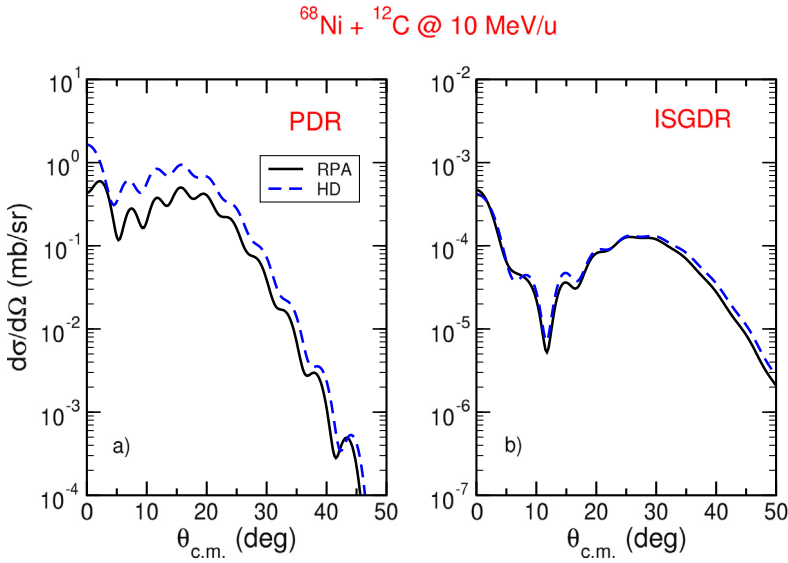


**Fig. 28.** Differential cross sections for the system  $^{68}\text{Ni} + ^{12}\text{C}$  at 10 MeV/u for the PDR state (left panel) and for the ISGDR (right panel). They have been calculated with the DWUCK4 code. The solid black lines are the results of the calculations done with the form factors constructed with the microscopic RPA transition densities, the blue dashed line with the HD ones.

The differential cross section for the ISGDR state, shown in Fig. 28(b), for the microscopic form factors and the HD ones are almost indistinguishable due to their almost identical form factors. This is a consequence of the fact that this state is a pure isoscalar state and it is well described by the procedure employed in Refs. [165,166]. On the other hand, the comparison for the PDR case is not satisfactory: the cross section corresponding to the HD form factors are higher with respect to the microscopic one up to a factor of 3 in the more important forward angular region. This can be ascribed to the different transition densities shapes at the surface of the nucleus. Since we are dealing with surface processes, the forward angle part of the cross section is the most important contribution to the excitation process. Moreover, the almost factor three in the external region of the form factors is generating a factor of almost nine in the cross section.

The above analysis has shown that for the pure isoscalar state ISGDR the macroscopic and microscopic models coincide in the description of the transition densities and in the form factors and consequently in the cross sections. In the case of the PDR state the weakly-bound nature of the involved orbitals leads to different slopes in the tails of the macroscopic and microscopic transition densities, with consequent differences in the corresponding form factors and cross sections.

Therefore, one has to be carefully in the use of the form factor in the experimental analysis of PDR state excitation. Use of non appropriate form factor has its consequence on the calculated cross section and therefore in jeopardizing the extracted physical quantities. Only the microscopic form factor, by construction, includes all the important properties of these states, starting from the strong mixing of isoscalar and isovector character. These microscopic form factors have been successfully employed in the analysis of various experiments performed with  $^{17}\text{O}$  as isoscalar probe [26–29]. In these papers, only the use of the microscopic form factor has allowed to extract the isoscalar component of the  $1^-$  excited states.

#### 4.5. Collectivity of the low lying dipole states

One important question is how collective are the dipole states observed at low energies. One measure of the collectivity is the number of particle-hole components [171,172] entering in the RPA wavefunction with an appreciable weight. In the RPA calculations presented here, one can analyze the nature of these low lying states in more detail. Following Ref. [171], one can see what is the contribution, in percentage, of a p-h configuration to the formation of a given dipole state. In Ref. [155] there are shown such components for one low lying dipole state, together with their contribution to the norm of the states. The major contribution comes from the neutrons closer to the nuclear surface. Indeed, the neutron p-h configurations contribute for more than 80% to the formation of the state. Another way to measure the grade of collectivity was indicate as the ratio between the weight, in terms of the RPA amplitudes, of the p-n contributions and the total number of p-h states for the considered multipolarity [173].

The fundamental concept that underlies collectivity is coherence. The reduced transition probability from the ground state to the excited state  $\nu$  can be written as

$$B(E\lambda) = \left| \sum_{ph} b_{ph}(E\lambda) \right|^2 = \left| \sum_{ph} (X_{ph}^\nu - Y_{ph}^\nu) \langle p \parallel \hat{O}_\lambda \parallel h \rangle \right|^2 \quad (19)$$

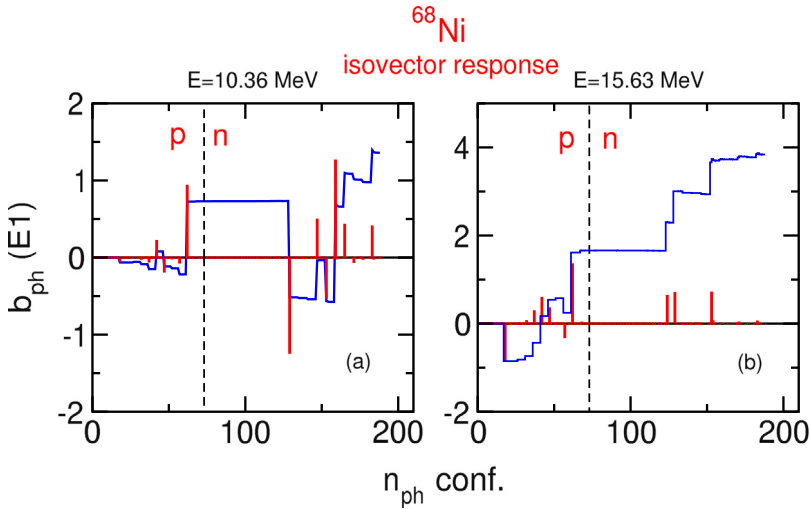


**Fig. 29.** Partial contributions for the  $b_{ph}$  of the reduced transition probability for electromagnetic excitations vs. the p-h configurations used in the RPA calculations. The order goes from the most to the less bound ones. The dashed lines divide the protons from the neutron configurations. The bars correspond to the individual  $b_{ph}$  contributions while the continuous thin (blue) line is the cumulative sum of the contributions. The figures on the left column are for one low lying dipole states of  $^{68}\text{Ni}$  while the one on the right are for the GDR state.

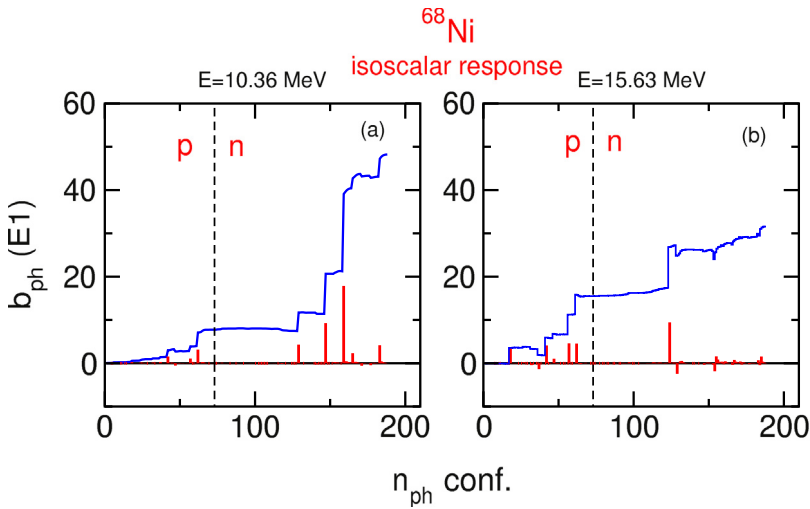


**Fig. 30.** Same as Fig. 29 but for the isoscalar response.

where  $\langle p \parallel \hat{O}_\lambda \parallel h \rangle$  are the  $2^\lambda$  reduced multipole transition amplitudes associated with the elementary p-h configurations. The previous quoted measure, based only on the RPA magnitude ( $|X_{ph}^\nu|^2 - |Y_{ph}^\nu|^2$ ), can be misleading because it does not take into account the transition amplitude nor the relative signs of the separate contributions. On the contrary, coherence plays a fundamental role in building a significant value for  $B(E\lambda)$ . Indeed, as it is shown in Ref. [155] an elevated number of p-h contribution it is not a sufficient condition to assess the collectivity of a state. This is clearly shown in Fig. 29 where the partial contributions  $b_{ph}$  versus the p-h configurations used in the RPA calculations are plotted. The order goes from the most bound configurations to the higher ones. In the RPA, the number of configuration entering in the calculations depends on the energy cut off that one impose to the particle-hole configurations, in the calculation shown here it is imposed an energy cut-off of 50 MeV. The bars in the figure correspond to the individual values of the  $b_{ph}$  while the continuous thin line is the cumulative sum of the contributions. The dashed lines divide the protons from the neutron configurations. The Fig. 29(a) refers to a state lying in the energy range of the PDR while the one in Fig. 29(b) is for a state belonging to the GDR region. From the figure we can clearly see how the  $B(E1)$  of the GDR states are built up by the small contributions of many p-h configurations which add coherently. For the low-lying states we have a different behavior: there are several p-h configurations participating to the formation of the  $B(E1)$  but they do not add coherently, some of them have opposite sign giving rise to a final value which is small. From our novel analysis, it emerges that

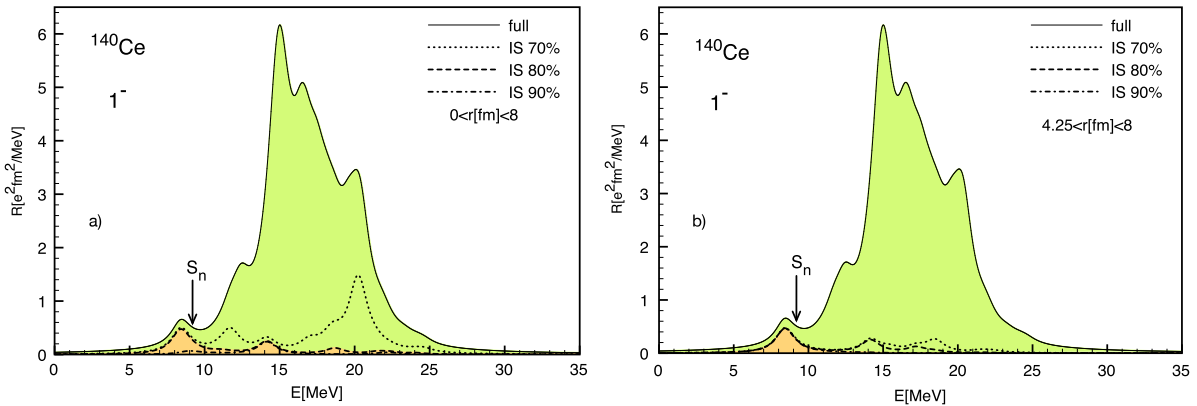


**Fig. 31.** Dipole transition strength for  $^{140}\text{Ce}$  calculated within the RHB + RQRPA. The dotted, dashed and dotted-dashed curves give the isoscalar contributions (see legend) for two different regions of the nucleus. On the left frame for radial region between 0 and 8 fm; on the frame (b) for distances between 4.25 fm and 8 fm. (See text).

Source: Figure adapted from [175].

although the low-lying states cannot be described as collective as the GDR states they cannot be considered as single p-h configuration. On the contrary, looking at the isoscalar response for the same two states then one can appreciate from Fig. 30 the collective character in both cases. In summary one can state that while the isoscalar response for the low lying dipole states shows, for all the examined cases, a clear sign of collectivity, the isovector response for the same excited states do not show the same behavior. The latter are the product of a cooperative, although not coherent as discussed above, effect of several particle-hole excitations. Equivalent conclusions have been drawn in other work [174].

#### 4.6. Isospin character of the low-lying dipole states from theory

The use of isoscalar probes has brought to light new interesting feature of the PDR mode as the isospin splitting. This point is discussed extensively in the next section in connection with several experimental results in different mass regions. From the theoretical point of view, there were several studies intended to establish the isoscalar content of this mode. For instance, calculations done with a fully self-consistent relativistic quasi-particle random phase approximation based on the relativistic Hartree-Bogoliubov model (RHB + RQRPA) have produced the transition strength [175] which is the quantity that can give useful information. The calculation was done for  $^{140}\text{Ce}$  and for this nucleus the isoscalar strength content was analyzed with the following procedure. Whenever the proton and neutron transition densities, for each particular state, were found in phase over more than 70% (80%) within the radial interval between 0 and 8 fm the state was denoted IS 70% (IS 80%). The result of this analysis is plotted in Fig. 31 (a) where most of the low lying strength show an isoscalar character. The same analysis was performed for the surface region between 4.25 fm and 8 fm and in Fig. 31 (b) it is shown that in this case transitions with predominant isoscalar character are located mainly in the low energy region giving rise to the peak at 8.4 MeV. Therefore, reaction like  $(\alpha, \alpha'\gamma)$  or  $(^{17}\text{O}, ^{17}\text{O}'\gamma)$ , which explore the peripheral nuclear surface are more suited to excite the states belonging to this region. On the other hand the electromagnetic interaction acts on the entire nucleus. Similar results were found using the fully self-consistent non relativistic mean field approach based on Skyrme Hartree-Fock plus random phase approximation, for the nuclei  $^{68}\text{Ni}$ ,  $^{132}\text{Sn}$ , and  $^{208}\text{Pb}$  [174]. For each radial distance, at which the neutron and proton transition densities were calculated, the state  $\nu$  is defined 70% isoscalar if the 70% of the points satisfy the following condition:  $|\delta\rho_{\nu}^{IS}(r)| > |\delta\rho_{\nu}^{IV}(r)|$ . This analysis show that most of the states that are 70% isoscalar belong to the PDR peak at low energy for all the three nuclei studied.

A more complete and satisfactory study was carried out within the QPM [139] and the relativistic quasi-particle time-blocking approximation RQTBA [141–143] that take into account the coupling to multiphonon states going beyond the quasi-particle RPA. The QPM wave functions include one-, two- and three-phonon components and their spectrum is calculated within a QRPA based on Saxon-Woods mean field corrected in order to reproduce the experimentally known single particle levels. The RQTBA is based on the covariant energy density functional and it goes beyond the simple two-quasiparticle configuration. In this framework the model space is constructed with the quasiparticles of the relativistic mean field and the phonons are calculated within the self-consistent relativistic QRPA. In both approach the electromagnetic as well as the isoscalar response have been calculated for the nucleus  $^{124}\text{Sn}$  and both of them clearly show the suppression of the isoscalar dipole strength at higher energy in comparison with the isovector B(E1). In Fig. 2 of Ref. [176] the inelastic cross section for the reaction  $(\alpha, \alpha', \gamma)$  for  $^{124}\text{Sn}$  is compared to the measured  $B_{em}(\text{E1})$  values for the same nucleus and with the  $B_{IS}(\text{E1})$  and  $B_{em}(\text{E1})$  calculated within the QPM and RQTBA model.

However, the comparison to the experimental data requires more attention on the isoscalar part because the  $\alpha$  scattering cross section cannot be directly compared with the calculated isoscalar B(E1). Thus the comparison is at a

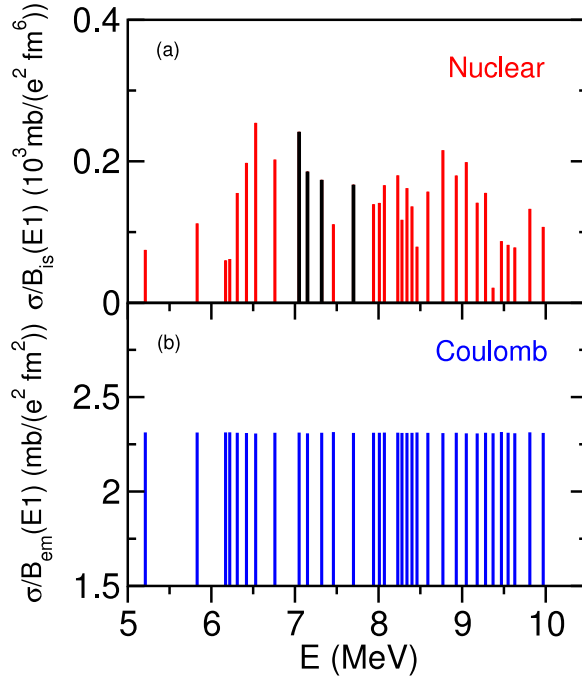


**Fig. 32.** Ratios between the inelastic cross sections, calculated by putting to zero the energies of the states, to their corresponding  $B(E1)$ . The two panels show the results for the nuclear (a) and the Coulomb (b) excitations. See text.

“qualitative level”. Indeed, while the relation between the isovector reduced transition probability  $B(E1)$  and the inelastic Coulomb cross section is clear, that is they are proportional, the same relation with the IS  $B(E1)$  is not evident. In order to move the comparison at a quantitative level one has to perform inelastic cross section calculations.

Calculation within a semiclassical model have been performed for the system  $\alpha + {}^{124}\text{Sn}$  at  $E_\alpha = 136$  MeV [177]. This semiclassical model [155,156] assumes that the colliding nuclei move on a classical trajectory determined by the real part of the optical potential while the internal degree of freedom are described according to the quantum mechanical. The internal structure of the nucleus  ${}^{124}\text{Sn}$  was calculated [20] within the RQTBA and the ground state density as well as the transition densities were used to construct the optical potential and the radial form factors by a double folding procedure.

To illustrate the difference in the relation between cross section and  $B(E1)$  for isoscalar and isovector probe one could take the ratio, for each dipole state, between the Coulomb (nuclear) cross section and the isovector (isoscalar) reduced transition probability. But these ratios are biased by the Q-value effect, that depends on the energies of the states, which imply that the cross section have extra factors depending on the dynamic of the excitation process. In order to eliminate such effect, we calculate the cross section by setting to zero the energies of the states. In this way one eliminates the contribution due to the dynamics of the reaction and one should obtain, at least for the Coulomb inelastic cross section, a value proportional to the  $B_{em}(E1)$ . Therefore a plot of the ratio of the inelastic cross section, calculated only with the Coulomb interaction, and the  $B_{em}(E1)$  should produce a constant value for all the considered states. In Fig. 32, we plot the ratio

$$\frac{\sigma_x^i(E_i = 0)}{B_x^i(E1)} \quad (20)$$

where  $\sigma_x^i(E_i = 0)$  is the excitation cross section for the dipole state  $i$  calculated by putting by hand its energy  $E_i$  to zero and  $B_x^i(E1)$  is its reduced transition probability. The index  $x$  indicate the two isovector and isoscalar cases. These ratios are plotted at the values of the real energies of the states. Then, in the lower frame of Fig. 32 the ratio for the Coulomb case shows a constant value for all states. Conversely, in the case where only the nuclear interaction is taken into account the ratio is not constant as shown in Fig. 32(a). Therefore for nuclear excitation one has to perform inelastic cross section calculations in order to extract precise information from the comparison between experimental data and theoretical calculation. However, the calculated cross section reproduce the global feature of the strong reduction of the experimental  $\alpha$  cross section at higher excitation energy compared to the isovector channel. This calculation provides the missing link to directly compare the results from the microscopic RQTBA calculations to experimental data measured via the  $(\alpha, \alpha'\gamma)$  reaction, confirming the structural splitting of the low-lying E1 strength.

## 5. The isospin character of low-lying dipole states from experiments

The study of the isospin character of dipole states dates back to the beginning of the eighties when the first searches were made to identify states of dipole character with energy values corresponding either to  $1\hbar\omega$  or  $3\hbar\omega$  ( $\hbar\omega$  being the main energy gap in nuclear shells). Some evidence, in the  $^{208}\text{Pb}$  and  $^{144}\text{Sm}$  nuclei, for the presence of excitations corresponding to the  $3\hbar\omega$  component of the isoscalar dipole resonance denoted as Isoscalar High Energy Dipole resonance (ISHEDR) was reported first. This evidence was found in experiments measuring inelastic scattering ( $\alpha, \alpha'$ ) at very forward angles. In the following years many experiments were performed and systematics measurements at high energy resolution have allowed to deduce the high energy dipole strength at around 25 MeV and from the ensemble of measurements the value of the nuclear compressibility was obtained (see [9] and references therein). The main experimental difficult to extract unambiguously the high lying isoscalar dipole strength is the proper subtraction of the enormous nuclear continuum as well as the elimination of other multipole strengths which are present in the excitation energy region of interest.

Information on the existence of the low energy part corresponding to excitation at around an energy equal to  $1\hbar\omega$  was first obtained at  $A < 40$  [178] and a major step forward for the search of the low-energy component of the isoscalar dipole excitation was made using the  $(\alpha, \alpha'\gamma)$  reaction. By measuring in coincidence with the inelastically scattered  $\alpha$ -particles the  $\gamma$ -decay to a ground state  $0^+$  one can uniquely identify the multipolarity of the excited intermediate states. This is because the  $\alpha\text{-}\gamma$  angular correlation bears the characteristic feature of the angular momentum of the state from which the gamma-ray is emitted.

This approach of measuring  $\gamma$ -decay following excitation via alpha particle was used in a pioneering experiment performed in the nineties [178] in which the nuclei  $^{208}\text{Pb}$ ,  $^{90}\text{Zr}$ ,  $^{58}\text{Ni}$  and  $^{40}\text{Ca}$  were used as targets. The chosen bombarding energy was 120 MeV and indeed for heavy nuclei up to about 150 MeV the Coulomb excitation hardly plays a role in the excitation of these state.

The main aim was to identify the  $1\hbar\omega$  excitations. In that experiment NaI(Tl) scintillator detectors were used to measure  $\gamma$ -rays and a magnetic spectrometer for the detection of the scattered  $\alpha$  particles. The main results of this experiment were that substantial amounts of strength were located in the region  $1\hbar\omega$  in medium and heavy mass nuclei. Moreover it was demonstrated that the  $(\alpha, \alpha'\gamma)$  reaction is an elegant and powerful tool in identifying the low-energy isoscalar dipole strength. This reaction is found to have sensitivity to the radial transition density on the nuclear surface. Two important outstanding features were clearly evident in the results of this experiment, one is the strong fragmentation of the dipole strength, and the other is that the isoscalar low energy dipole strength is never the lowest in excitation energy, contrary to the situation for isoscalar octupole excitations. This can be understood keeping in mind that odd-parity states arise mainly from exciting nucleons to the next higher shell. Because of the attractive isoscalar residual interaction a coherent collective state is pushed down in energy. The lowest  $3^-$  state is usually located around  $E_x=2-3$  MeV in heavy nuclei. The fact that the most collective  $1^-$  state is never the lowest in excitation energy could indicate that the dipole strength is less collective than the octupole type.

The main limitation of the experiment of Poelhekken et al. [178] was related to the energy resolution of the photon detectors, scintillators, used to measure the gamma-rays. The use of scintillator detectors did not allow at that time to extend these interesting studies in other nuclei of interest, as e.g. the semimagic ones which are characterized by level spacing of 10–20 keV.

Because of the great interest in understanding the nature of  $1^-$  states below particle binding energy in the last decade several new measurements were made with the same reaction  $(\alpha, \alpha'\gamma)$  but using in the set up HpGe detectors allowing high resolution measurements of gamma-rays. Moreover several more recent experimental studies were made using another isoscalar probe, namely using the reaction  $(^{17}\text{O}, ^{17}\text{O}'\gamma)$ . The use of Ge detectors allowed to study for the first time semimagic nuclei. Only in the case of investigations of unstable nuclei scintillator detectors were used and the experiments were done in inverse kinematics.

The main features of the experimental techniques used in the study of the isospin character of dipole states and for the search of low-lying dipole strengths in unstable nuclei are presented in the three following subsections. There a short description is given for the different set-ups used for the measurements of the  $(\alpha, \alpha', \gamma)$  and  $(^{17}\text{O}, ^{17}\text{O}'\gamma)$  reactions with stable targets and for the measurements of gamma decay in inelastic reactions in inverse kinematics for unstable beams. For the discussion of the obtained results, presented in the next section, the experimental data are grouped according to their mass regions. In fact, because of the existence of several results, most of them rather recent, an organization of their presentation is needed. This presentation points out that the studies on the nature of the low lying dipole response have addressed different mass regions in order to find out whether or not there are similarities and/or differences and how large are the effects of shell closures and of level density .

## 6. Results from experiments using isoscalar probes

### 6.1. The isospin character of dipole states in light nuclei (mass $\leq 30$ )

The experimental study of excitation of isoscalar dipole type requires investigation in two energy regions of the nuclear excitation spectra, one corresponding to an energy of  $1\hbar\omega$  and the other to  $3\hbar\omega$ , with  $\hbar\omega$  being the size of the major shell gap in the harmonic oscillation. The first evidence of the high lying  $3\hbar\omega$  dipole excitation was obtained for the nuclei by

measuring the  $(\alpha, \alpha')$  reaction at very forward angles [9]. For light nuclei, one of the first investigations of the electric dipole response showed a low lying strength of pygmy type in  $^{17}\text{F}$  populated with the reaction  $^{16}\text{O}(p, \gamma)$  [179].

The only nucleus far from stability, accessed using radioactive beams, for which the dipole response was studied with both Coulomb excitation and scattering of  $\alpha$  particles is  $^{20}\text{O}$  [47]. The main motivation for this study, conducted under the same experimental conditions, is to determine whether or not the isospin splitting in low-energy dipole excitations is universal among neutron-rich nuclei. Furthermore light nuclei are the subject of extensive studies to test predictions based on ab initio calculations.

The main result of the experiment on  $^{20}\text{O}$  was the difference in population cross section for states below the particle binding energy when using  $^{197}\text{Au}$  or  $^4\text{He}$  target. This can be clearly viewed in Fig. 33 giving the Doppler-corrected  $\gamma$ -ray spectra measured with the two different targets. In this figure the background spectra was obtained using the  $^{24}\text{O}$  since no bound excited states are known for this nucleus and the energy resolution was limited by Doppler broadening. The comparison of the spectra reveals that there are three strong peaks at around 3.68, 5.36, and 6.84 MeV in the  $^{20}\text{O} + \text{Au}$  reaction, while these peaks are rather weak in the  $^{20}\text{O} + \alpha$  reaction. Because of the kinematical conditions this implies that the corresponding states are better excited by the Coulomb potential (gold target) rather than by the nuclear potential ( $\alpha$  target). There is also some evidence that these  $\gamma$ -rays originate from the  $1^-$  states. In particular the analysis of the single and  $\gamma-\gamma$  coincidence spectra shows the decay of the two  $1^-$  states at 5.36 and 6.84 MeV takes place via ground state decay and to the first  $2^+$  state (1.67 MeV) with rather large branching (26% and 48%, respectively).

Cross sections and transition strengths were extracted via a distorted-wave Born approximation (DWBA) analysis with the Ecs97 code. The used optical potential, is that widely used in the analysis of experimental data on unstable nuclei within the suitable energy range [47]. Because of the large thickness of the target and of the angular opening of the detectors it was important to take these effects into account in calculating the scattering angle distributions. The angular smearing from multiple Coulomb scattering in the targets (8 mrad in gold) and by the angular resolution of the detectors (4 mrad) were thus included. In addition, the different values of the angular acceptance of the Zero-Degree spectrometer for the two reactions were taken into account.

From the measured cross sections the fraction of the isoscalar dipole sum rule ISD EWSR were extracted and the obtained values are shown in comparison with the  $B(E1)\uparrow$  strengths in Fig. 34. In the left panel of this figure the corresponding values for  $^{16}\text{O}$  for states in the same energy region are displayed. The difference in the  $B(E1)\uparrow$  strengths is significant between  $^{16}\text{O}$ , the doubly magic nucleus in the oxygen chain, and  $^{20}\text{O}$ . To be noted that the integral of the  $B(E1)\uparrow$  strength over the two states goes from  $0.492 \cdot 10^{-3} \text{ e}^2 \text{ fm}^2$  in  $^{16}\text{O}$  to  $7.36(33) \cdot 10^{-2} \text{ e}^2 \text{ fm}^2$  in  $^{20}\text{O}$ . Conversely the integrated ISD EWSR fraction does not show much variation, being 4.2% in  $^{16}\text{O}$  and 3.37(34)% in  $^{20}\text{O}$ . In the case of  $^{16}\text{O}$ , the isovector dipole strength is strongly suppressed having this nucleus the same number of neutrons and protons. This explains the almost purely isoscalar nature of the state referred to as the macroscopic squeezing mode [166], but the present results indicate that low-energy dipole excitations in  $^{20}\text{O}$  exhibit a dual character, suggesting that these states have different underlying structures.

The experimental results were compared with the random-phase approximation (RPA) calculation using SLy4 and SkI2 Skyrme interactions [180], the latter shown in Fig. 35. The transition density calculated by using the SLy4 interaction indicates that the excitation mostly involves the one-particle-one-hole state of the proton. This leads to a rather strong isovector with weaker isoscalar strength. The relationship between the isovector and isoscalar strengths was similar to that observed for the  $1_2^-$  state at 6.84(7) MeV, regardless of the interaction. In contrast the other  $1_1^-$  state at 5.36(5) MeV was found to have much stronger isoscalar strength than hardly compared to the prediction. It was therefore deduced that the  $1_2^-$  state at 6.84(7) MeV is generated by the proton excitation, leading to its dominant isovector character. The other  $1_1^-$  state at 5.36(5) MeV, hardly explained by the RPA predictions, may originate from more complex effects. One possibility is that this  $1_1^-$  state cannot be represented by the superposition of the one-particle-one-hole excitations, on which the present RPA is built. In this scenario, more elaborated calculation considering two-particle-two-hole states is desired. Another possibility is the presence of pairing correlations. In this case, the valence neutrons may contribute to the  $1_1^-$  state, because the pairing correlation affects the orbital occupancy of the valence neutrons. Further theoretical studies including these effects are necessary to obtain insight on the structure of this  $1_1^-$  state. It is also interesting to compare the low-energy dipole strengths with those in other neutron-rich nuclei in the mid mass regions, the case of Ca isotopes being the most interesting in this connection. The isoscalar dipole strength decreases with increasing energy, while the isovector dipole strength is largely unchanged below the neutron threshold. Since the comparison with RPA suggests that the proton excitation generates the dominant isovector character, investigating such state in various neutron-rich nuclei is important.

Altogether the study of low lying dipole state needs to be done with much detail since the intrinsic structure of these states varies considerably.

## 6.2. The isospin character of dipole states in Ca isotopes

The first information on the existence of low-energy isoscalar dipole strength in the excitation energy region of  $1 \hbar\omega$  ( $\hbar\omega$  being the main energy gap in nuclear shells) was obtained  $^{40}\text{Ca}$ . The experimental tool was the inelastic scattering of  $\alpha$ -particles for which the isoscalar dipole cross section is at its maximum at very forward angles. The identification of the multipolarity of the excited states is well achieved by measuring in coincidence with the inelastically scattered  $\alpha$ -particles the  $\gamma$ -decay to a  $0^+$  ground state.

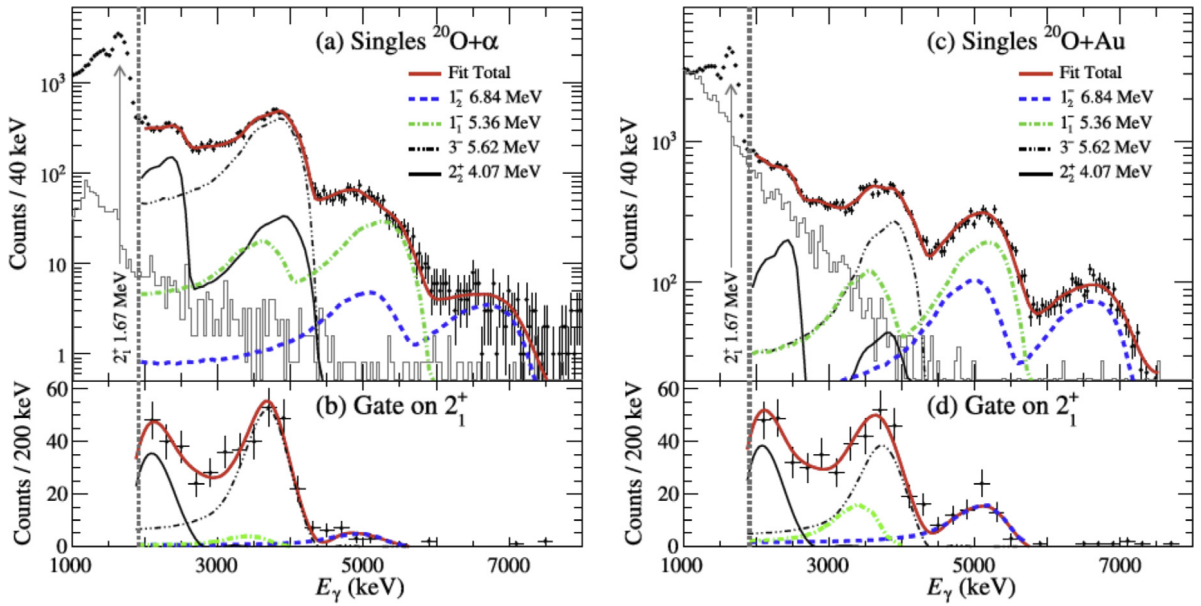


**Fig. 33.** The Doppler-corrected  $\gamma$ -ray spectra:  $^{20}\text{O} + \alpha$  singles(a),  $^{20}\text{O} + \alpha$ , detected in coincidence with the  $2_1^+$  state (1.67 MeV)(b),  $^{20}\text{O} + \text{Au}$  singles(c),  $^{20}\text{O} + \text{Au}$ , detected in coincidence with the  $2_1^+$  state (d). The gray histograms are the background spectra. Error bars are statistical. The fit was performed above the energy of 1900 keV (energy higher than vertical gray-dotted lines).

Source: Adapted from [47].

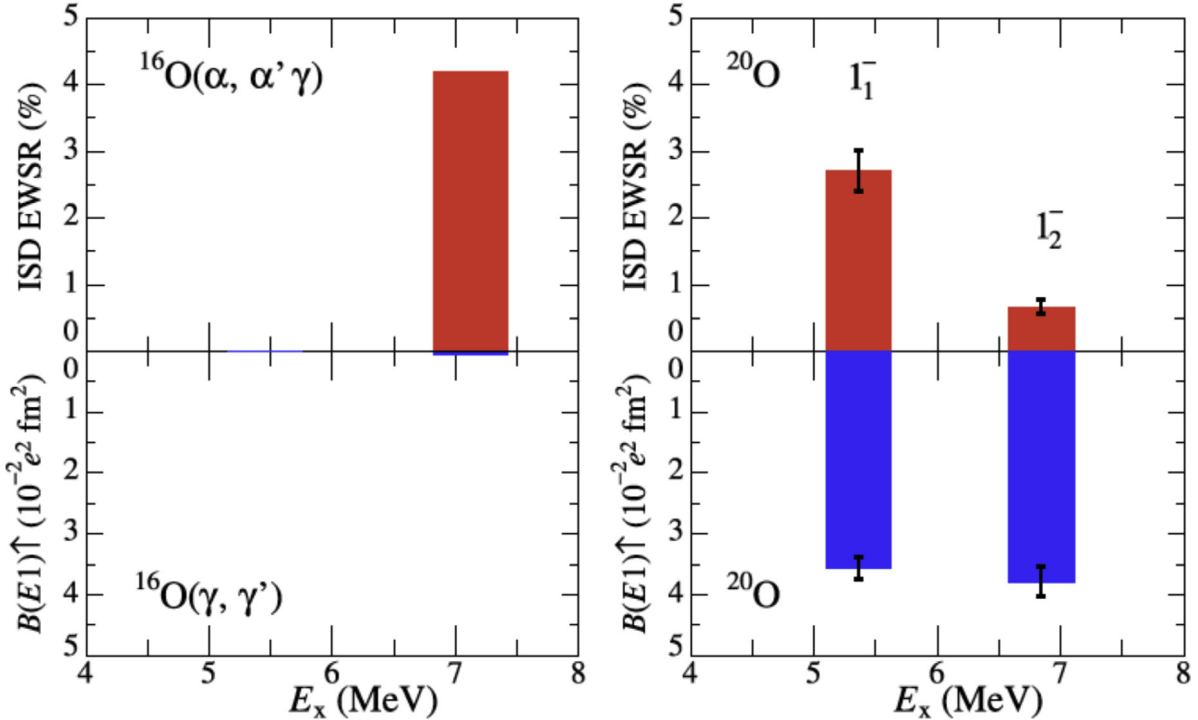


**Fig. 34.** The measured ISD EWSR (top) and  $B(E1)\uparrow$  (bottom) strengths in  $^{20}\text{O}$  (right), in comparison with  $^{16}\text{O}$  (left).

Source: Adapted from [47].

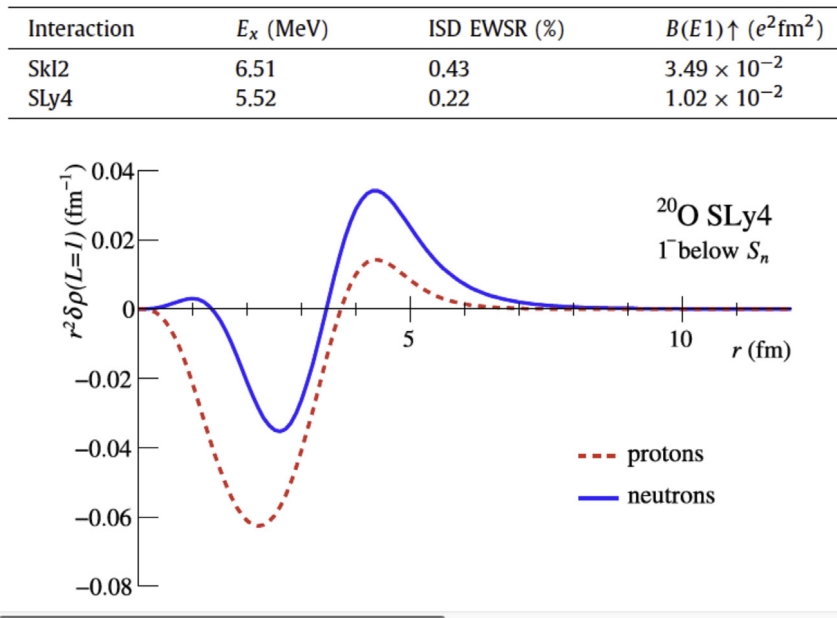


**Fig. 35.** The transition density of the  $1^-$  state below the neutron-separation threshold calculated using the RPA approach. Protons are represented by the dashed red line and neutrons by the solid blue line.

Source: Adapted from [47].

The isotopic chain of Ca isotopes including two doubly-magic nuclei  $^{40}\text{Ca}$  and  $^{48}\text{Ca}$  is considered among the key-stones for testing theoretical approaches. In addition, the rather low level density of these nuclei allows a detailed experimental investigation of individual excitations. Concerning the measurement using the  $(\gamma, \gamma')$  reactions results from experiments made at the S-DALINAC showed that the measured fraction of the Thomas–Reiche–Kuhn (TRK) energy weighted sum rule (EWSR) for IV E1 transitions up to 10 MeV amount to 0.020(3)% for  $^{40}\text{Ca}$  and to 0.39(7)% (0.39(4)% for  $^{44}\text{Ca}$ ) (for  $^{48}\text{Ca}$ ) [181]. These findings are consistent with microscopic calculations using the extended theory of finite Fermi systems [182]. It should also point out that for the  $^{40}\text{Ca}$  nucleus a strong E1 gamma transitions at around 5.9 MeV is not included in the group of gamma transitions in pygmy states. This is due to the fact that its decay branching ratio, recently measured in an experiment using the  $(\gamma, \gamma')$  reaction, suggests a two phonon nature of this state. Indeed the data indicate the presence of a strong decay branch via an E2 gamma-ray with a strength similar (within the error bars) to that from the decay from the first  $2^+$  state.

The strong motivation to study the excitation of  $1^-_1$  states in  $^{40}\text{Ca}$  and  $^{48}\text{Ca}$  using different probes is connected to the need of understanding theoretical predictions indicating that all even Ca isotopes with  $N=14-40$  develop strong IS-LED states. In addition it was predicted that the nature of these states varies with neutron number and excitation energy and this calls for data for both the  $B(E1)$  strength and for the response to the isoscalar operator by employing isoscalar probes.

The work employing  $(\alpha, \alpha'\gamma)$  reaction at  $E_{beam} = 136$  MeV on a  $^{48}\text{Ca}$  target resulted in the measurement of the double differential cross section for seven  $1^-_1$  states [181]. The measured spectrum is shown in Fig. 36 from which one can see that the transitions of interest are above the sensitivity limit, which was determined by integrating the background in the  $\gamma$ -ray spectrum. The excitation of states with spin quantum number  $J=1$  was identified via decays to the ground state. The measured  $\gamma$ -ray spectrum displays the presence of ground state decays from excitation of natural parities only (namely  $1^-, 2^+, \dots$ ). Additional information on the parity of these states was obtained from a measurement using linearly polarized photons, performed at the High Intensity Gamma-ray Source (HIGGS) facility. The measured experimental asymmetries of the decays led to the assignment of an electric character to all excited spin 1 states.

Double-differential cross sections were deduced from the  $(\alpha, \alpha'\gamma)$  data and compared to  $\alpha\text{-}\gamma$  angular distributions calculated from m-state amplitudes that were obtained from DWBA calculations. This analysis was very useful to pin down the origin of the observed ground-state transitions (see Fig. 36). Results of the angular correlation of the most intense transitions were found to be well reproduced not only in the case of the  $1^-$  states but also for the  $2^+$  state at 3.8 MeV and 3 state at 4.5 MeV (see Fig. 36).

The fraction of the exhausted EWSR for isoscalar dipole (ISD) transitions (ISD EWSR) derived from the  $(\alpha, \alpha'\gamma)$  data is shown in Fig. 37 in comparison to  $B(E1)\uparrow$  values from  $(\gamma, \gamma')$  data. For  $^{40}\text{Ca}$  the  $\alpha$ -scattering cross sections are roughly proportional to the E1 strengths deduced from the  $(\gamma, \gamma')$  experiment. The situation in  $^{48}\text{Ca}$  differs from that in  $^{40}\text{Ca}$  in both, the total E1 strength and its fragmentation into mainly seven excitations. More remarkable and surprising is the

difference in the response to the isovector ( $\gamma$ -ray) and isoscalar ( $\alpha$ -particle) probes: two excitations show a converse behavior. The  $1^-$  state at 7.3 MeV, which has the strongest E1 transition probability in the  $(\gamma, \gamma')$  experiment, was not excited by the  $\alpha$  particles within an experimental sensitivity limit for the cross section of 0.15(4) mb/sr. On the contrary, the state at 7.6 MeV, which provides one of the weakest transitions in the  $(\gamma, \gamma')$  experiment, has the largest cross section for excitation by particles amounting to 1.61(9) mb/sr.

Different theoretical approaches are available that give insight into the nature of the E1 excitations in the Ca isotopes [136,138,183–185]. Chambers et al. [183] applied density functional theory and predicted a linear dependence of the low-lying E1 strength on the excess neutrons in the Ca chain. This behavior was not found experimentally, since the E1 strength up to 10 MeV in  $^{44}\text{Ca}$  is similar to that in  $^{48}\text{Ca}$ . Further calculations [152] pointed out that phonon coupling (as well as coupling to the single-particle continuum, pairing, and complex configurations) is required to reproduce the  $(\gamma, \gamma')$  data. The E1 response in even Ca isotopes was also investigated along with the ISD response on basis of first-order quasiparticle RPA using the Gogny D1S interaction [152]. Over the whole range of neutron numbers ( $N = 14 - 40$ ) different scenarios explain the origin and nature of ISD strength which is present in all Ca isotopes. Proton-skin oscillation, pure IS oscillation, as well as neutron-skin oscillation are the generating mechanisms, where the latter one is predicted for  $N < 30$ . The RPA results in terms of strength distributions are shown in Fig. 37 for both doubly-magic Ca isotopes. An energy shift of around 3 MeV to lower energies is generally needed for reproducing the data in the Ca isotopes [152]. Such an energetic discrepancy with data is consistent with other RPA studies of various nuclei and is expected to be caused by coupling to complex configurations and low-lying phonons, effects which RPA does not take into account. For lighter isotopes up to  $^{48}\text{Ca}$  one excitation with a dominantly IS character and almost constant ISD strength is predicted. This state is visible for  $^{40,48}\text{Ca}$  in Fig. 36 and can be assigned to the strongly excited state in the  $(\alpha, \alpha'\gamma)$  experiments on  $^{40}\text{Ca}$  and  $^{48}\text{Ca}$  at 6.9 and 7.6 MeV, respectively. The corresponding IS velocity fields (see Fig. 37) are characterized by similar flows for both nuclei, having also similar transition densities and form factors, with an oscillation of a surface layer against a core and a toroidal surface oscillation. From this comparison it was inferred [181] that the state at 7.6 MeV could be a pure IS state and, therefore,  $N = 28$  seems to define the transition from IS to mixed, neutron-skin oscillation ( $N < 30$ ). A pure IV state, as experimentally identified at 7.3 MeV, is not predicted close by the strong ISD state, but at higher excitation energy. Unlike the experimental results, in RPA the stronger IV states lie generally above the IS state. A possible explanation is that RPA does not take into account coupling to low-lying two-phonon states and the energetic shift of the particle-hole states close to the Fermi level, which, in the present model, are predominately responsible for the low-lying dipole strength. As in the experimental data, there is a similar IS-IV pattern for  $^{40}\text{Ca}$  and a different IS-IV pattern for  $^{48}\text{Ca}$ .

The experimentally observed difference in the dipole response of  $^{48}\text{Ca}$  is due to different isospin characters of the excitations. In comparison to the self-conjugate nucleus  $^{40}\text{Ca}$ , the dipole spectrum of  $^{48}\text{Ca}$  is richer showing IS, IV, and isospin-mixed nature which indicates a coexistence of different dipole modes with the possibility to mix. Concerning collectivity it has to be noted that the E1 strength of each state is much less than one single-neutron unit. From experiment and prediction for both isotopes one sees that much more of the total ISD strength is carried by the low-lying excitations compared to the IV strength and in all cases most of the ISD strength is carried by only one excitation. This suggested the coexistence of different underlying mechanisms in the two different channels.

### 6.3. The isospin character of dipole states in nuclei in the mass region $\approx 70$

In this mass region experiments were made for the stable  $^{74}\text{Ge}$  and the unstable  $^{68}\text{Ni}$  nucleus. The main results and comparison with theoretical predictions are here discussed.

#### *The $^{74}\text{Ge}$ nucleus*

An experiment was performed at iThemba laboratories to study the population cross section for known  $1^-$  states for the reaction  $(\alpha, \alpha'\gamma)$  at bombarding energy of 48 MeV [158]. The  $\alpha$  particles were measured in Si telescopes at the angular range  $20^\circ$  and  $72^\circ$ . The obtained results for the relative cross section  $(\alpha, \alpha'\gamma)$  and for the relative intensity for  $(\gamma, \gamma')$  are shown in Fig. 38.

With respect to  $(\alpha, \alpha'\gamma)$  studies at bombarding energy of 136 MeV in heavier nuclei  $^{124}\text{Sn}$ ,  $^{138}\text{Ba}$  and  $^{140}\text{Ce}$  in  $^{74}\text{Ge}$  the isoscalar response at low energy is much stronger. In addition, many of the dipole excitations in the energy interval  $6 < E_x < 9$  MeV are found to have a strongly mixed nature with large isovector component. Only a few weakly populated pure isoscalar states and several pure isovector states are found at  $E_x > 6$  MeV. This finding is in general agreement with the predictions shown in the top panel in the right part of Fig. 38, displaying prediction within the RQTBA framework [158]. The transition densities within the same model (proton and neutron components, isoscalar and isovector components) for two states, one below and one above 6 MeV are shown in the bottom-right panel Fig. 38. One sees clearly that the isoscalar component at 7 MeV is very small, consistently with the experimental results.

#### *The $^{68}\text{Ni}$ nucleus*

The search of the presence of pygmy states in this unstable nucleus started almost a decade ago with an experiment performed at the Laboratory GSI using the RISING set up (see [45] and [187] and references therein) in a special configuration to detect high energy  $\gamma$ -rays. The used experimental setup RISING at GSI was designed to detect scattered particles at  $0^\circ$  allowed to select Coulomb excitation and the chosen bombarding energy of 600 MeV/A assured that the

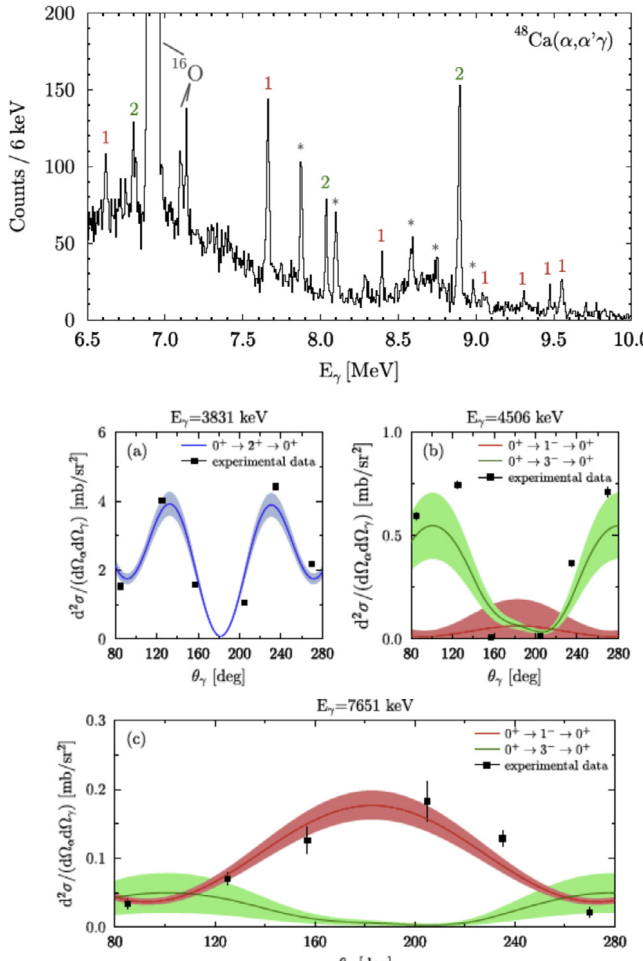


**Fig. 36.** In the top panel the  $\gamma$ -ray spectrum  $^{48}\text{Ca}$  obtained using the  $(\alpha, \alpha'\gamma)$  reaction and by gating on deexciting transitions to the ground state. Observed electric transitions in  $^{48}\text{Ca}$  are labeled according to their multipolarity. Transitions in  $^{40}\text{Ca}$  are marked with stars, and the ones in  $^{16}\text{O}$  are labeled. In the lower panels double-differential cross sections from the  $(\alpha, \alpha'\gamma)$  reaction on  $^{48}\text{Ca}$  for different transitions to the ground state, together with calculated  $\alpha\gamma$  angular correlations for specified spin sequences. The angular correlations were fitted to the data points and the fit error is indicated by the width of the bands.

Source: Adapted from [181].

dominant excitation is from virtual photons of E1 type. The difficulty in this type of measurements is to achieve high precision for the Doppler correction. Indeed the Doppler correction is dominating the energy resolution of the measured gamma-spectrum. The measured spectrum shows a peak centered at approximately 11 MeV, whose intensity can be explained in terms of an enhanced strength of the dipole response function (pygmy resonance). This is shown in the top-right part of Fig. 39. The same figure illustrates on the top-left panel the incident radioactive beams including the  $^{68}\text{Ni}$  ions that can be well separated from the other ions in the beam cocktail and impinging the Au target (for very recent data for the nucleus  $^{70}\text{Ni}$  on a Au target see [188]). The found strength in the pygmy resonance region is approximately 5% of the EWSR strength. This is similar to what was found with the LAND set up at GSI for unstable neutron-rich nuclei around and including the  $^{132}\text{Sn}$  nucleus [4], but is sizably larger than in stable nuclei. This result is in rather good agreement with theoretical predictions giving values ranging from 5 to 10% (see [4,45,46,187]).

An important aspect of the predictions for pygmy states is the presence of both an isovector and isoscalar components and to test the presence of the latter one needs to excite the nucleus using mainly nuclear excitation.

To investigate the presence of an isoscalar component in the pygmy region for the nucleus  $^{68}\text{Ni}$  an experiment was recently made using  $^{68}\text{Ni}$  ions at a bombarding energy at 28 MeV/A impinging on a  $^{12}\text{C}$  target. This experiment was performed at the fragmentation facility of LNS-INFN with the set up CHIMERA plus FARCOS to measure the scattered particles and the emitted gamma-rays [39]. Fig. 39 (bottom-left panel) shows the energy loss  $\Delta E$  and energy scatter plot and  $\Delta E$  and time of flight (TOF) scatter plot used for the isotopic identification of the fragments with nuclei with Z between 27 and 30. The gamma ray spectrum (then converted in cross section) obtained after subtraction of the statistical model contribution (similarly to what done in the case of the Coulomb excitation data at 600 MeV/A) is shown in Fig. 40. The data presents a peak centered at approximately 10.5 MeV and within the error bars of the uncertainty of

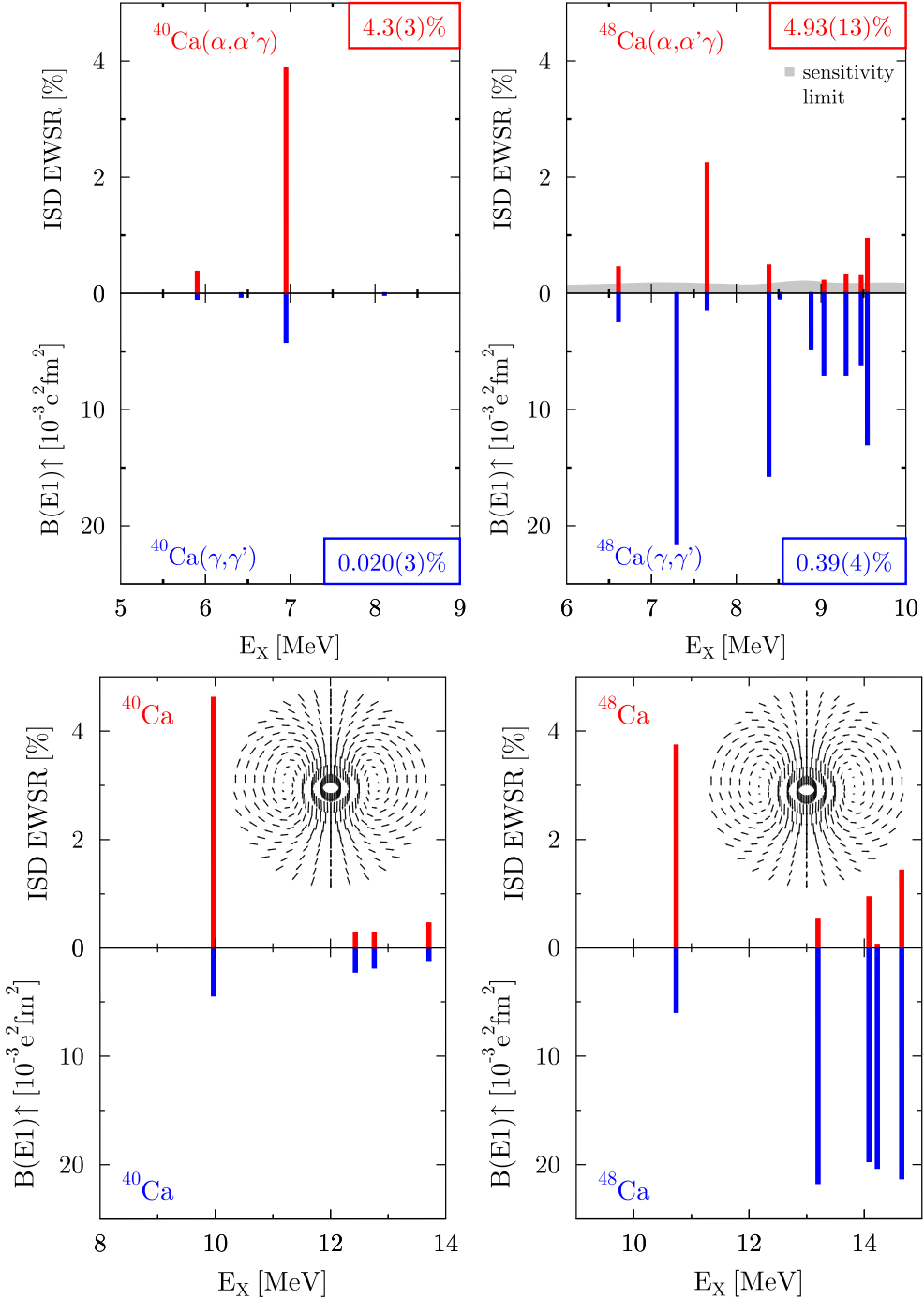


**Fig. 37.** The panels at the top show the low-lying E1 strength in  $^{40}\text{Ca}$  and  $^{48}\text{Ca}$  obtained using the  $(\alpha, \alpha'\gamma)$  reaction (upper panel) and the  $(\gamma, \gamma')$  reaction (lower panel). The gray-shaded area indicates the experimental sensitivity limit. The framed percentages give the summed exhaustion of the respective ISD (upper panel) and IV (lower panel) EWSR. The panels at the bottom show the low-lying ISD and  $B(E1)\uparrow$  strength in  $^{40}\text{Ca}$  (left panel) and  $^{48}\text{Ca}$  (right panel) obtained from RPA calculations from [152]. In addition, IS velocity fields for the lowest lying excitation are shown. Source: Adapted from [181].

the energy determination (due mainly to the Doppler correction and to the subtraction of the calculated statistical model contribution) this peak is in rather good agreement with the peak centroid (11 MeV) found with the Coulomb excitation data at 600 MeV/A.

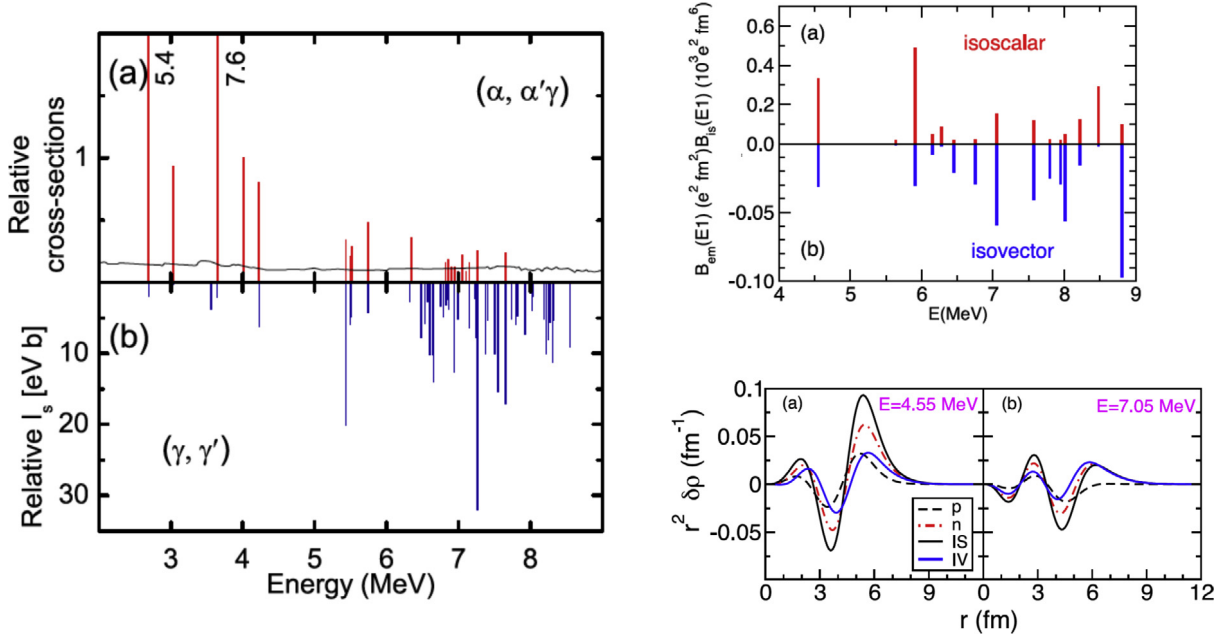


**Fig. 38.** Data for the relative cross section of population of states in  $^{74}\text{Ge}$  with the  $(\alpha, \alpha'\gamma)$  at 48 MeV (a). The yield of the state at 4007 keV is used to normalize the data. In panel (b) the relative integrated scattering cross sections obtained from  $(\gamma, \gamma')$  [186] are shown. Numbers next to some transitions indicate the total value of relative cross section. In panel (a), the sensitivity limit is shown by the black solid curve. In the top right panel the reduced transition probabilities in  $^{74}\text{Ge}$  from RQTBA calculations are plotted for the isoscalar (a) and electromagnetic (isovector) (b) dipole operators. Transition densities for two calculated RQTBA states at  $E_x=4.55$  (a) and 7.05 MeV (b) in  $^{74}\text{Ge}$  are shown.

Source: Adapted from [158].

For the experiment made with  $^{68}\text{Ni}$  ions on a  $^{12}\text{C}$  target more details are given in Fig. 40. From this figure it is important to note the following: (i) the spectrum measured in coincidence with the  $^{67}\text{Ni}$  ions (the red open-square points in the top left panel of Fig. 40) that is much steeper than that of  $^{68}\text{Ni}$ ; (ii) the angular distribution of the gamma-rays has the behavior of the E1 transitions; (iii) the angular distribution of the scattered  $^{68}\text{Ni}$  ions is decreasing as expected. However for the latter no calculations were made with the DWBA approach mainly because no data were collected for the elastic scattering from where to deduce the optical model parameters.

It is important however to point out calculations of the cross section made at 28 MeV/A indicate that for the inelastic cross section more than 60% is due to nuclear interaction, 9% to Coulomb interaction and the rest to the interference between nuclear and Coulomb contribution. The mixed character of the dipole states can be inferred by the comparison of the two experiments, one with the Au target (at 600 MeV/A) and the other at 28 MeV/A with a C target. In addition, it seems that the so-called isospin splitting is not present in this case. The result is interesting but needs further investigation in the future to be more quantitative in the interpretation of the cross-sections. For example, the experiment performed with the  $^{12}\text{C}$  target did not provide information on the population cross section but only the decay cross section. In contrast, the data at 600 MeV/A were also corrected for neutron branching ratio and virtual photon spectra to deduce the population cross section.

#### 6.4. The isospin character of dipole states in the mass region 90

##### The $^{90}\text{Zr}$ nucleus

This nucleus, with a magic neutron number, was first studied in the work of Ref. [178] with the  $(\alpha, \alpha'\gamma)$  and it showed the presence of isoscalar strength up to around the particle binding energy. Since that experiment used low resolution detectors for the detection of  $\gamma$ -rays and since it was clear that the use of other isoscalar probes is important to investigate further the problem, another experiment was performed for this nucleus using high resolution set up and  $^{17}\text{O}$  as a probe [26].

In that experiment  $2^+$  and  $1^-$  states were populated via the  $(^{17}\text{O}, ^{17}\text{O}'\gamma)$  reaction at 340 MeV. The gamma decay was measured using the AGATA demonstrator array consisting of high resolution segmented Germanium detectors. Differential cross sections were obtained at few different angles for the scattered particle.

For the  $1^-$  states the population cross section obtained in the  $(^{17}\text{O}, ^{17}\text{O}'\gamma)$  experiment is compared in the bottom left panel of Fig. 41 with that measured in the  $(\gamma, \gamma')$  electromagnetic reaction. Some increase of  $B(E1)\uparrow$  is seen in the  $(\gamma, \gamma')$  data (from Ref. [101]) while a strong decrease is evident in the  $(^{17}\text{O}, ^{17}\text{O}'\gamma)$  data. In addition, the relative behavior of the

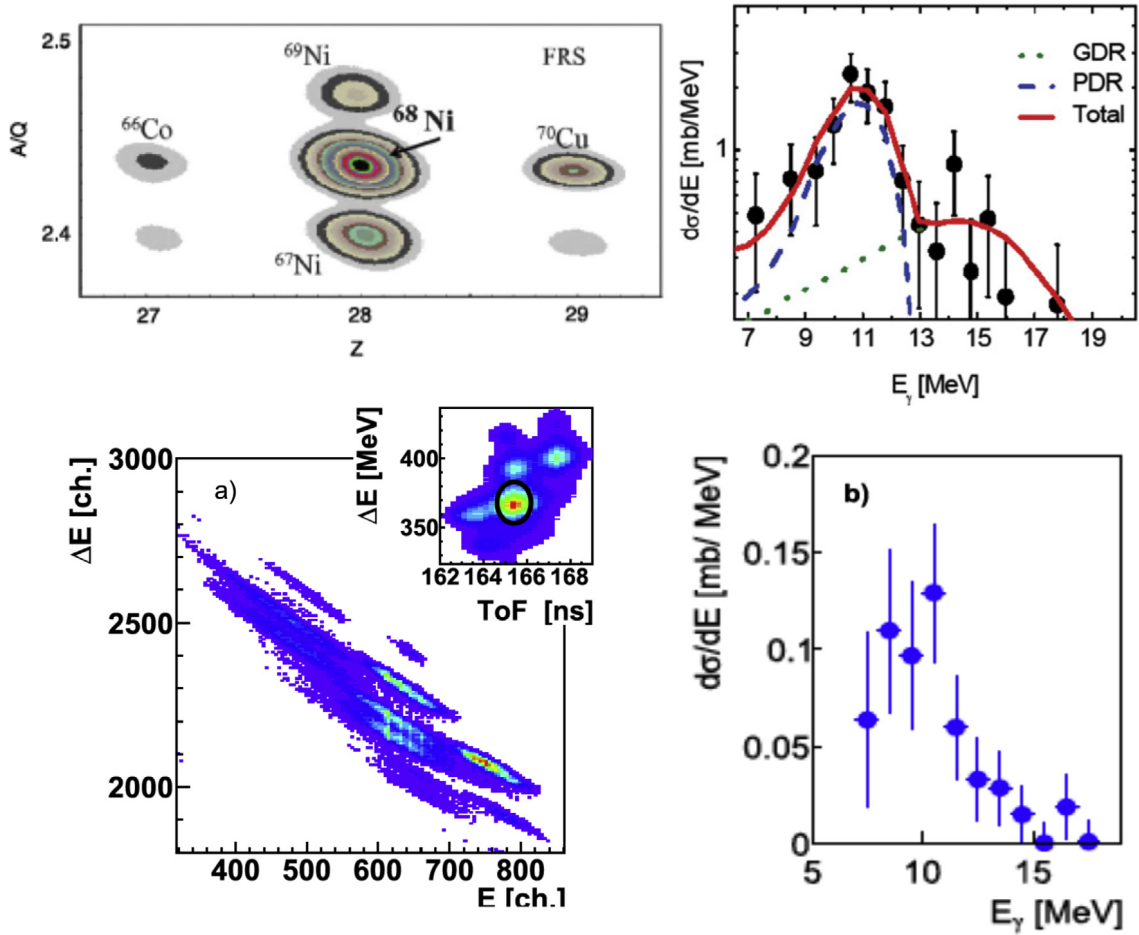


**Fig. 39.** Data on  $\gamma$ -decay for the nucleus  $^{68}\text{Ni}$  obtained with the RISING setup using the reaction  $(^{68}\text{Ni}, ^{68}\text{Ni}'\gamma)$  on an Au target at 600 MeV/A are shown in the right upper panel. Data obtained with the CHIMERA plus FARCOS set up using the reaction  $(^{68}\text{Ni}, ^{68}\text{Ni}'\gamma)$  [187] on a  $^{12}\text{C}$  target at 28 MeV/A [39] are shown in the right lower panel. The left-upper and left-lower panels show the particle identification scatter plots for the corresponding data on  $\gamma$ -decay.

Source: Adapted from [187] and [39].

cross sections measured at  $E_x > 6.5$  MeV is shown in the top-left panel of Fig. 41 for the reactions  $(^{17}\text{O}, ^{17}\text{O}'\gamma)$ ,  $(\gamma, \gamma')$ , and the  $(\text{p},\text{p}')$  reactions [55]. There the quantity  $\sigma_R = \sigma(E_x)/\sigma(7 \text{ MeV})$  is plotted, where  $\sigma(E_x)$  is the cross section at excitation energy  $E_x$ . A strong increase of these relative cross sections in the excitation energy interval 6.5 to 11 MeV is observed for the  $(\gamma, \gamma')$  and  $(\text{p},\text{p}')$  data while a strong decrease is evident in the  $(^{17}\text{O}, ^{17}\text{O}'\gamma)$  data.

For the  $(^{17}\text{O}, ^{17}\text{O}'\gamma)$  reaction at 20 MeV/u the results of the elastic scattering and inelastic excitation cross section for the  $2^+$ ,  $3^-$ , and  $1^-$  states were compared with DWBA predictions. In the top-right panel of Fig. 41 this comparison is shown for the strongly populated  $1^-$  state at 6.424 MeV. The DWBA calculation for this state, based on the adopted  $B(E1)\uparrow=0.018 \text{ e}^2\text{fm}^2$  value and with the standard form factor used for isovector dipole states (as, for example, the GDR), is shown as a black solid line in the top-right panel of Fig. 41. This calculation accounts only for a rather small fraction of the measured yield. It is clear that the nuclear part is not well described by the standard distorted potential approach in the case of this  $1^-$  state. Therefore a calculation was performed using a microscopically calculated form factor [26] (shown in the bottom-right panel of Fig. 41) which was calculated by a double folding procedure with a M3Y nucleon-nucleon interaction [159]. The corresponding prediction, shown with the red curve in the top-right panel of Fig. 41, reproduces well the data. From this analysis it was found that the  $1^-$  state at 6.424 MeV has a dominant isoscalar component and has a character typical of pygmy states. In addition, it is found to exhaust 2.17% of the isoscalar dipole EWSR strength.

#### The $^{94}\text{Mo}$ nucleus

The  $(\alpha, \alpha'\gamma)$  reaction at  $E_\alpha = 136$  MeV was employed to study the electric dipole response in the open-shell vibrational nucleus  $^{94}\text{Mo}$  below the neutron-separation threshold [19]. The overall feature of the excitation of  $1^-$  states can be seen in Fig. 42 where comparison is made with the data obtained with the  $(\gamma, \gamma')$  reaction. The excitation cross section is

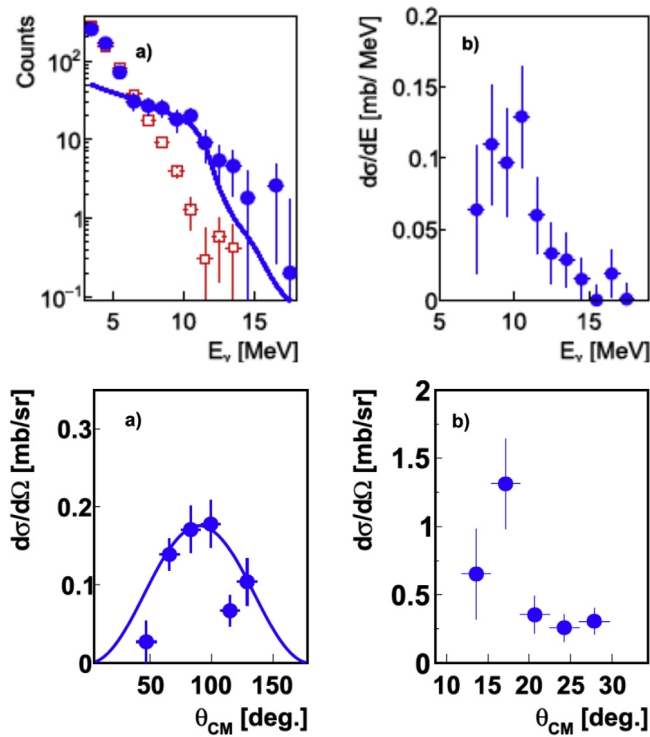


**Fig. 40.** Data for  $^{68}\text{Ni}$  obtained with the reaction  $(^{68}\text{Ni}, ^{68}\text{Ni}' \gamma)$  on a  $^{12}\text{C}$  target at 28 MeV/A. The panels show: (top left) the  $\gamma$ -ray spectra in coincidence with  $^{67}\text{Ni}$  (red points) and with  $^{68}\text{Ni}$  (blue points) and the corresponding statistical model calculation; (top right) the  $\gamma$ -ray spectrum after subtraction of the two spectra on the top left panel; (bottom left) the  $\gamma$ -ray angular distribution; (bottom right) the angular distribution of the scattered  $^{68}\text{Ni}$  ions.

Source: Adapted from [39].

characterized by the presence of a plateau in the excitation energy region between 6 and 8 MeV, where the PDR is located, and it ends with a sharp drop at the neutron-separation energy where the neutron channel opens.

The comparison of the two reactions yields some qualitative information about the isospin character of the excited states and therefore also about their nature. The majority of the stronger states below 5 MeV observed in  $(\gamma, \gamma')$  were also excited by the  $\alpha$  particles and above 5 MeV only a few states which were excited by photons, were excited by the  $\alpha$  particles as well. All other dipole excitations at these higher excitation energies are completely missing in the  $\alpha$ -scattering experiment.

For the three states with excitation energies  $E_x = 4136.3(15)$  keV,  $E_x = 5442.1(9)$  keV, and  $E_x = 5701.9(4)$  keV in addition to the ground-state decay a transition to the first  $2^+$  state at 871 keV was observed for the first time. This can be seen in the excitation-energy spectra obtained with gates on  $E_x = E_\gamma$  and  $E_x = E_\gamma + 871$  keV in the two-dimensional  $E_\gamma$  versus  $E_x$  plots. The branching ratios were determined to be 0.53(4), 0.45(6), and 0.27(3) for the three  $1^-$  states above. These branching ratios are not longer negligible for the calculation of the cross section. This information of the branching ratios is a further structural information which helps to clarify the structure of the PDR. To be noted that this experiment showed the excitation of previously known symmetric and mixed-symmetric  $2^+$  states and thus new information on further excited states was gained.

### 6.5. The isospin character of dipole states in the $^{124}\text{Sn}$ nucleus

The low lying dipole states in the region below the neutron binding energy in neutron rich stable  $^{124}\text{Sn}$ , nucleus with magic proton number, were investigated with experiments using the three probes  $(\gamma, \gamma')$ ,  $(\alpha, \alpha'\gamma)$ , and  $(^{17}\text{O}, ^{17}\text{O}', \gamma)$  [20,71,176], and [28].

It is of particular interest to compare the measured  $(^{17}\text{O}, ^{17}\text{O}', \gamma)$  cross sections with  $(\gamma, \gamma')$  and  $(\alpha, \alpha'\gamma)$  results. This comparison is presented in left panel of Fig. 43 showing the differential cross-sections associated to the ground-state decay spectrum with data in bins 100 keV wide. In the case of  $(^{17}\text{O}, ^{17}\text{O}'\gamma)$  and  $(\alpha, \alpha'\gamma)$  data, for each 100 keV bin two cross sections are shown: one corresponding to the counts in the known discrete peaks (full colored bars) and the other to the total measured counts denoted as unresolved strength (dashed gray bars). From this figure one sees for both  $(^{17}\text{O}, ^{17}\text{O}', \gamma)$  and  $(\alpha, \alpha'\gamma)$  data that there is a splitting of the PDR states in two regions. This is due to the different nature of

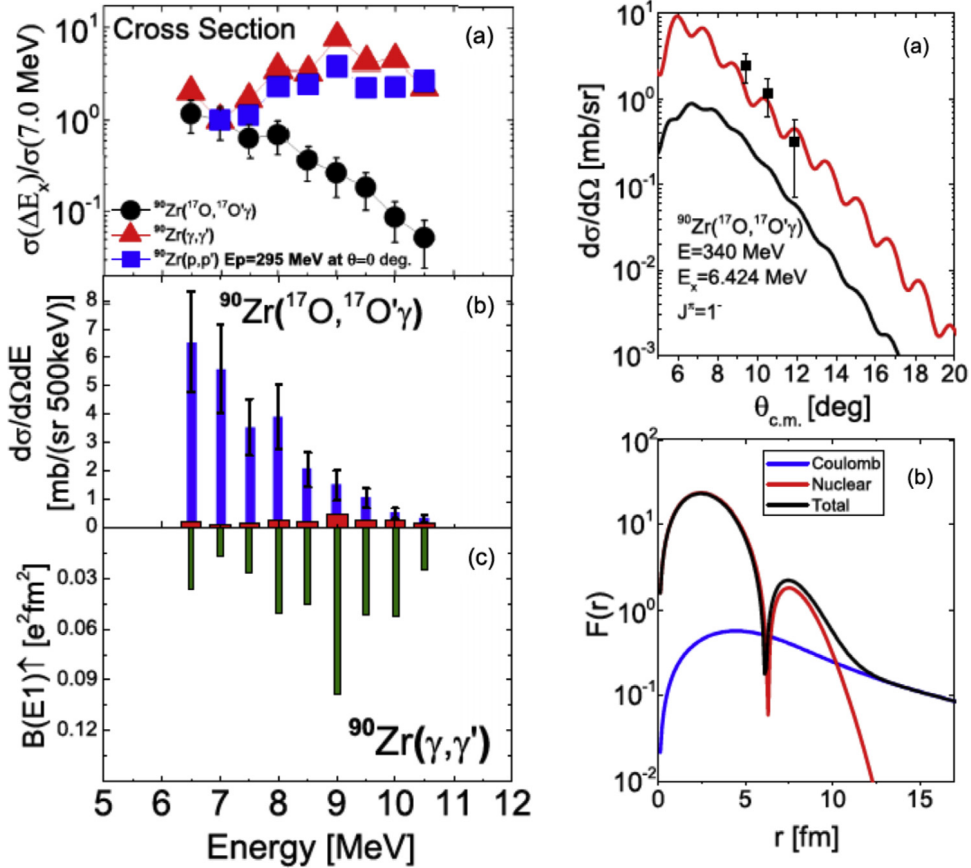


**Fig. 41.** The measured cross section ratio normalized at its value at 7 MeV is shown in 0.5-MeV bins as a function of excitation energy for the reactions  $(^{17}\text{O}, ^{17}\text{O}'\gamma)$  (black solid circles), from the one deduced from  $(\gamma, \gamma')$  data (red triangles) [91] and from the  $(p, p')$  data (blue solid squares) [55]. (Middle) The measured differential cross section for  $(^{17}\text{O}, ^{17}\text{O}'\gamma)$  in 0.5-MeV bins is displayed with blue bars. The red bars give calculated DWBA cross-section predictions assuming as  $B(E1)^\uparrow$  the values from  $(\gamma, \gamma')$  [91] shown in the bottom panel with the green bars. The right top panel shows the cross section in comparison with DWBA calculations. The black solid curve represents the calculations with the standard phenomenological form factor. The red solid line includes the nuclear contribution calculated with the microscopic form factor shown in the right bottom panel. Source: Adapted from [26].

these states: the low-lying part of the E1 strength appears to be characterized by isoscalar transition densities that are peaked on the surface which lead to an enhancement in the isoscalar E1 response, while the higher-lying states can be interpreted as transitions towards the GDR and, thus, are suppressed in the isoscalar channel [20]. The splitting of the PDR region becomes even more evident if we integrate the strength in the discrete peaks measured in each experiment into two regions, 5–7 and 7–9 MeV (insets of Fig. 43). From here one sees clearly that the strengths in the two regions measured in the  $(\gamma, \gamma')$  experiment are almost equal while this is not the case for  $(^{17}\text{O}, ^{17}\text{O}'\gamma)$  and  $(\alpha, \alpha'\gamma)$  experiments. The small relative difference between  $(\alpha, \alpha'\gamma)$  and  $(^{17}\text{O}, ^{17}\text{O}'\gamma)$  in the population cross sections of some states might be related to the nature of these states and to the different Coulomb and nuclear contributions of these reactions.

Concerning the size of the cross section and its description, DWBA calculations were performed and these are shown in comparison with the data in the right part of Fig. 43. The data are integrated in the excitation energy region 5.5–7 MeV. The cross-section calculations for the Coulomb excitation are shown with the black dashed line and correspond to the summed  $B(E1)$  equal to 0.22 W.u. A calculation including both the Coulomb and nuclear contributions and corresponding to a form factor of GDR type is shown with the green solid line in the bottom panel of Fig. 43. A large disagreement between data and these two calculations is found. In particular, the cross sections associated to a pure Coulomb excitation only accounts for less than 10% of the measured yield. This leads to conclude that the main contribution to the inelastic excitation comes from the nuclear part which need a nuclear form factor for these states different than that of GDR type. Indeed, the data are reproduced by the DWBA calculation (red solid line) including a microscopic form factor based on the transition density associated to the E1 pygmy states (shown in the inset of the figure) obtained with a relativistic quasiparticle time-blocking approximation (RQTBA) microscopic model [142]. The microscopic form factors have been obtained from these transition densities by using the double folding procedure [159]. It is also found that the total measured strength in the discrete peaks is 2.2(0.3)% of the EWSR and 7.8(0.7)% for the unresolved region.

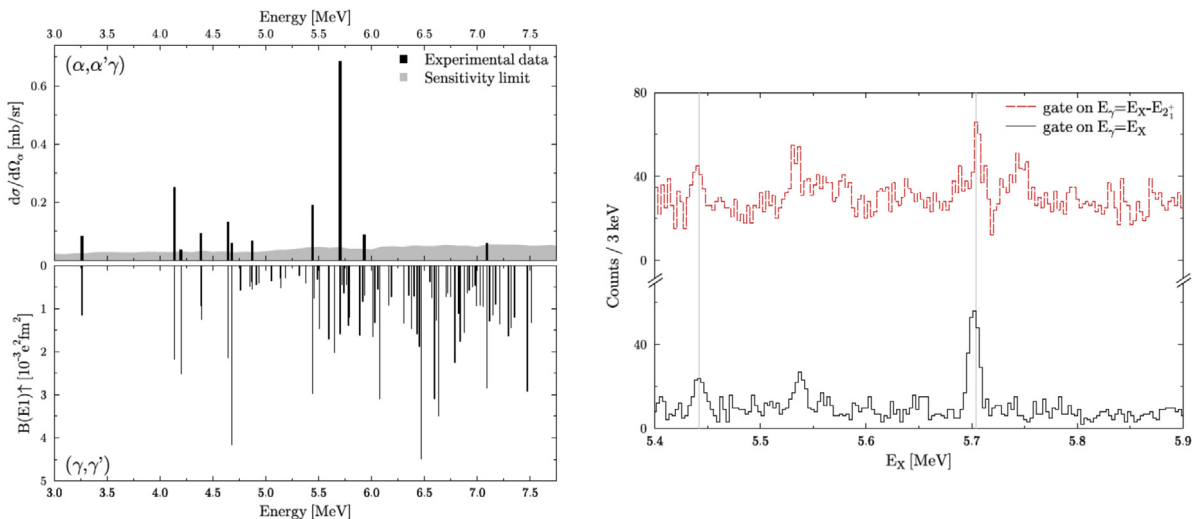


**Fig. 42.** Left panel: the experimental data obtained for the nucleus  $^{94}\text{Mo}$  with the  $(\alpha, \alpha'\gamma)$  reaction in comparison with data from [100] with the  $(\gamma, \gamma')$  reaction. Right panel: Excitation-energy spectra with gate on excitation energy shifted by the value of the first excited state at 871 keV. If the decay of a state branches strongly enough, transitions are visible at the same excitation energy in both spectra as for the transitions indicated by the vertical lines.

Source: Adapted from [19].

### 6.6. The isospin character of dipole states in the semimagic $N=82$ nucleus $^{140}\text{Ce}$ nucleus

The first high resolution measurement with the  $(\alpha, \alpha'\gamma)$  reaction to investigate the nature of pygmy states concerned the semimagic  $^{140}\text{Ce}$  nucleus ( $N=82$ ) [20,189]. In heavy semimagic even–even nuclei, such as  $^{140}\text{Ce}$ , the experimentally observed level spacing of the states building the PDR region is of the order of  $10 – 20$  keV, as deduced from measurements [88]. In addition, the level density of states with other multipolarities in the energy region of interest is also very high. Thus the selectivity of the  $(\alpha, \alpha'\gamma)$  reaction combined with a high resolution set up was well exploited to populate and identify low spin states.

Extensive works exist concerning the study of  $1^-$  in this nucleus which has the first  $1^-$  state at 3.643 MeV populated very strongly with the  $(\gamma, \gamma')$  reaction. This particular state was recently investigated with a very high statistics and low background experiment allowing to detect the branching ratios from this state [105]. The experiment is proving the existing conjecture for this state being a two phonon state belonging to the multiplet resulting from the coupling of vibrations of quadrupole and octupole type. In this connection it is important to point out that a first direct proof of the two-phonon character of the lowest  $1^-$  states of  $N=82$  isotones was provided in pioneering measurements of the decay of the collective  $1^-$  to  $3^-$  states via  $E2$  transitions. These measurements by M. Wilhelm et al. [190,191] used the  $(p, p'\gamma)$  reaction.

The  $1^-$  states at energy larger than 4 MeV are the ones denoted as pygmy states and for them it is important to examine their population and compare it with that of other reactions. This comparison is shown in Fig. 44. The figure shows the results obtained with the three reactions  $(\alpha, \alpha'\gamma)$ ,  $(\gamma, \gamma')$ , and  $(^{17}\text{O}, ^{17}\text{O}', \gamma)$  [29]. The main finding is that the  $1^-$  states with energy in the region 4–6 MeV are populated with all three reactions while states in the interval 6–8 MeV are only populated with the  $(\gamma, \gamma')$  reaction. The dissimilarity of the measured distributions with the isoscalar probes with that measured with the pure electromagnetic probe could only be explained by a different underlying structure of these two groups of  $E1$  excitations and hence a different response to the electromagnetic interaction of the photon on the one hand and the nuclear part of the  $\alpha$  and  $^{17}\text{O}$  interaction on the other hand. To be noted that the similarity of the population pattern obtained with the  $(\alpha, \alpha'\gamma)$  and 136 MeV and  $(^{17}\text{O}, ^{17}\text{O}', \gamma)$  at 20 MeV/u supports the isoscalar nature of both probes, as discussed in connection with other nuclei in this section [29].

In a simple macroscopic picture, two aspects in the structure of the excitations can cause the different responses: the isospin character and the radial transition density (surface or non-surface-peaked transition density). In the long-wavelength approximation ( $qr \ll 1$ ), the electromagnetic dipole operator is pure isovector to first order and the photon field interacts with the nucleus as a whole. Photons, therefore, induce primarily isovector transitions, which need not have surface-peaked transition densities. In contrast, the nuclear part of the  $\alpha$  and  $^{17}\text{O}$  interaction with the nucleons is purely isoscalar, and interact mainly with the surface of the nucleus. Therefore, isoscalar excitations with transition densities that are peaked at the surface are dominantly excited. In this simple picture, the dipole excitations around 6.5 MeV must have a weaker isoscalar component and/or have transition densities that are located more in the inner part of the nucleus compared to the excitations at 5.5 MeV. Apart from these considerations, the abrupt change of the  $E1$  distribution

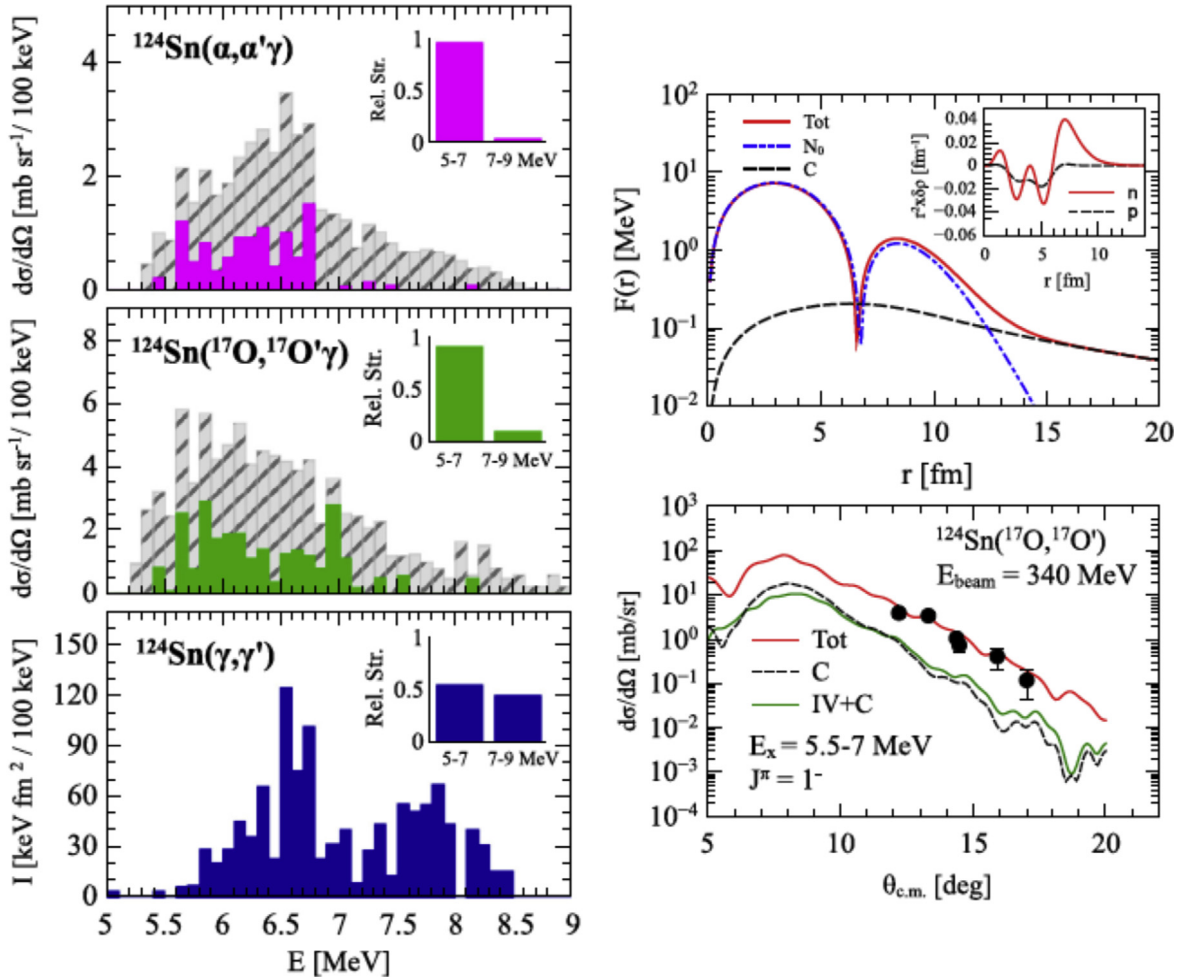


**Fig. 43.** Left panels: differential cross sections measured in the  $^{124}\text{Sn}(^{17}\text{O}, ^{17}\text{O}'\gamma)$  experiment [28], in bins of 100 keV (central panel). The unresolved strength, corresponding to the total binned counts in the measured spectra, is depicted in gray. For comparison, the strengths measured in  $\alpha$ -scattering (top panel) [20] and photon-scattering (bottom panel) [71] are shown. In each panel, the inset gives the relative intensity corresponding to the measured cross sections in the discrete lines integrated in two regions 5–7 and 7–9 MeV. Top right panel: Form factor associated to the PDR states for the  $^{124}\text{Sn}(^{17}\text{O}, ^{17}\text{O}')$  reaction at 20 MeV/A. The Coulomb (black dashed line) and the nuclear (blue dashed line) components are shown together with the total one (red solid line). The inset shows the neutron and proton transition densities used for the calculation of the form factors. Bottom right panel: differential cross sections for the  $1^-$  states in the excitation energy interval 5.5–7 MeV. The black dashed line shows the DWBA calculation with the Coulomb contribution only; the green solid line is a DWBA calculation including both the Coulomb and nuclear contributions with a form factor of GDR type; the red solid line (reproducing well the data) uses the total form factor shown in the top panel of the figure.  
Source: Adapted from [28].

observed in  $(\alpha, \alpha'\gamma)$  and  $(^{17}\text{O}, ^{17}\text{O}', \gamma)$  as compared to the NRF results shows that the PDR cannot be explained with a single underlying structure.

In the case of the  $(^{17}\text{O}, ^{17}\text{O}', \gamma)$  data a DWBA analysis was performed to describe the pygmy dipole excitation cross section. The optical potential was deduced from the elastic scattering data obtained in the same experiment. In the case of the  $1^-$  states the values of 0.061 and 0.121 W.u. for the sum of  $B(E1)\uparrow$  strength were used for the low- and high-energy regions, respectively. These values are known from the NRF experiment of Ref. [9]. For the nuclear contribution two different expressions were used for the form factor. Indeed one DWBA calculation was made using the standard collective form factor of IVGDR type and with this it was found that predictions account only for a small fraction of measured cross sections (12% and 42% for the low- and high-energy regions, respectively). This finding suggested that a large contribution to the cross section comes from the nuclear part and thus a proper form factor is needed. A second DWBA calculation used a microscopically calculated transition density which is illustrated in Fig. 45. This transition density shows typical features of the PDR states: neutron and proton transition densities are in phase in the interior and there is a strong surface contribution due only to neutrons. With the form factor calculated by the double folding procedure with the microscopic transition densities [159] it was possible to reproduce the data. This result indicates that the reaction  $(^{17}\text{O}, ^{17}\text{O}', \gamma)$  has

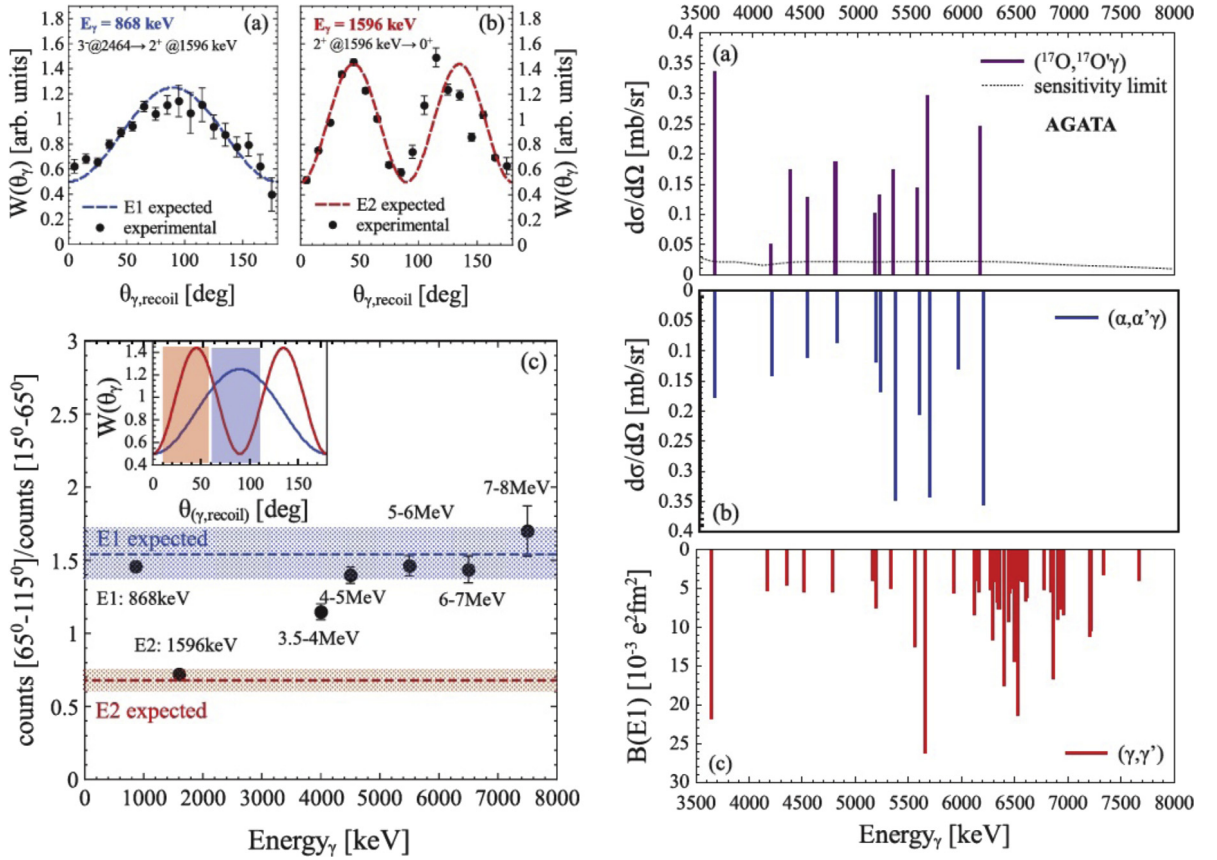


**Fig. 44.** The right panels show data on pygmy states in  $^{140}\text{Ce}$  obtained with the reactions  $(\alpha, \alpha' \gamma)$  [189],  $(\gamma, \gamma')$  [88], and  $(^{17}\text{O}, ^{17}\text{O}', \gamma)$  [29]. The left panels show angular distributions of  $\gamma$ -rays measured with the array AGATA and the  $(^{17}\text{O}, ^{17}\text{O}', \gamma)$  reaction. Source: Adapted from [29].

isoscalar character, because of its similarity with the  $(\alpha, \alpha' \gamma)$  in the excitation cross section, and that it is probing well the nuclear surface.

The isoscalar strength (SIS) in units of  $\text{e}^2 \text{ fm}^6 \text{ MeV}$  was obtained from the DWBA analysis of the experimental data. The summed strength in all discrete peaks was found to be to  $0.20(6) 10^4 \text{ e}^2 \text{ fm}^6$ . The total strength was found to be equal to  $0.88(11) 10^4 \text{ e}^2 \text{ fm}^6$ . These results were compared with two calculations, using the RQRPA and RQTBA approaches [29]. In the case of the RQRPA calculations, all the strength is accumulated in one peak at the energy of 8.39 MeV, while in RQTBA it is fragmented into a few peaks up to 8.8 MeV. It is found that the measured ISEWSR for the total PDR strength, which can be considered as an upper limit of the experiment, is lower than the predictions of the two models, but rather close to that obtained with the RQTBA approach. It should be noted that these two calculations predict the pygmy dipole states at higher energies as compared to the experimental observations. In the case of RQRPA, difference is about 3 MeV. It has been found that the pygmy mode, arising in the RQRPA as a single state with isoscalar character, is strongly fragmented over many states in a broad energy region due to the coupling to phonons. As a result, some fraction of the strength is located well below the original position of the RQRPA pygmy mode. It is in general difficult to reproduce the fragmentation of the pygmy dipole states as the relativistic RQRPA calculations largely overestimate the energy of the lowest  $2^+$  phonon, and this is also the case for the  $^{140}\text{Ce}$  nucleus. The RQTBA model, which additionally takes into account the coupling to the low-energy surface phonons, is able to reproduce the fragmentation to some extent, but also overestimates the PDR energy by about 2 MeV. It was discussed, e.g., for the  $^{116}\text{Sn}$  case that for the lowest RQTBA states the transition densities look similar to the RQRPA ones, but because of the fragmentation, the amplitude of the density oscillations is about a factor of 3 smaller. However, since there are more states, in total they can effectively give a similar contribution to the cross section. Therefore, it is reasonable enough to use RQRPA transition densities as it was done for the form factor calculations.

Another very recent and interesting work was made on the excitation of pygmy states in the  $^{140}\text{Ce}$  nucleus using inelastic scattering of protons at bombarding energy of 80 MeV [30]. This experiment is the latest in a series of experiments to investigate the PDR with different complementary probes to provide a multi-messenger data set on the properties of the PDR in  $^{140}\text{Ce}$ . The results of this experiment in comparison with other data and theoretical predictions are shown

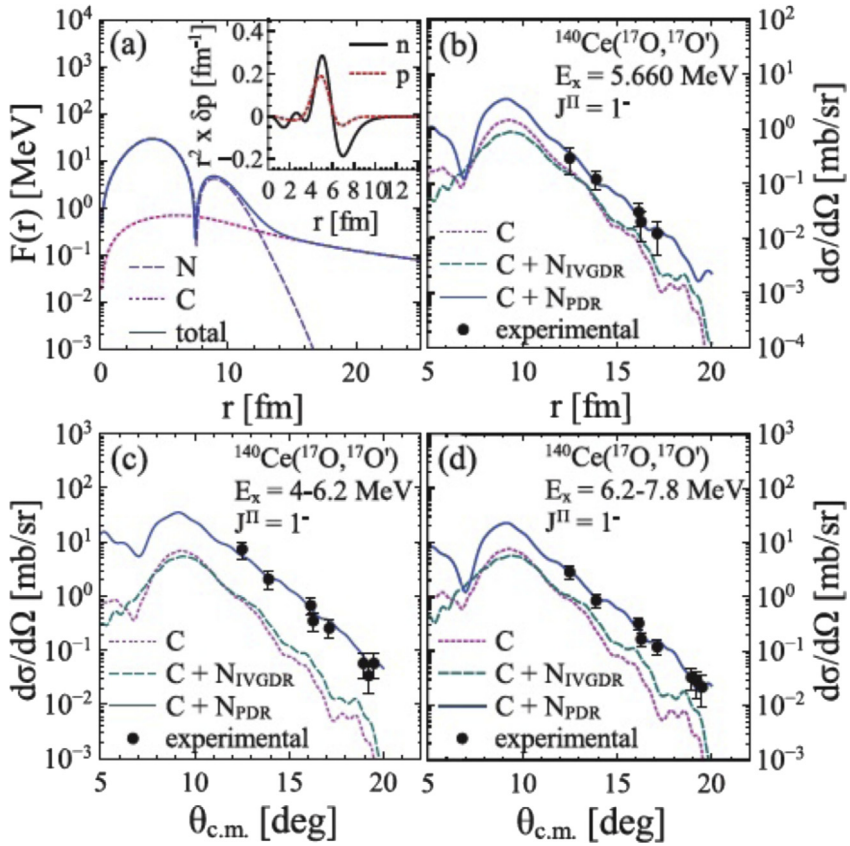


**Fig. 45.** Experimental cross sections for the PDR  $\gamma$  transitions in the nucleus  $^{140}\text{Ce}$  at (b) 5660 keV, and the integrated regions (c) below and (d) above 6.2 MeV measured in the ( $^{17}\text{O}$ ,  $^{17}\text{O}'$ ,  $\gamma$ ) experiment of Ref. [29]. The dotted purple line represents the Coulomb cross section calculated with the DWBA while the dashed green line is the total cross section using the standard collective form factor. The solid blue line represents the total cross section using the microscopic nuclear form factors in (a).

Source: Adapted from [29].

in Fig. 46. The prediction for the cross section were obtained within the Quasi-particle-Phonon Model (QPM) [30]. The transition densities from the QPM model, not only at the RPA level, but including the full model space of up to 3p-3h configurations were used to deduce the cross sections for excitation with both protons and  $\alpha$  particles. This allowed to compare the calculations to the experimental results on an absolute scale for single excitations. To be noted the good agreement of the calculations with the different data which not only concerns the excitation cross section but also the branching ratios to the first  $2^+$  state.

The comparison of the data obtained with the  $(\alpha, \alpha'\gamma)$  reaction and  $(p, p'\gamma)$  reaction indicates that the two reactions are predominantly of isoscalar nature although some admixture of isovector part is also present in the  $(p, p'\gamma)$  case. There is a small group of states populated with the  $(p, p')$  reaction and not with the  $(\alpha, \alpha')$  reaction. For protons this selectivity is less distinct as inelastic proton scattering is also sensitive to isovector components and the surface peaked interaction is less pronounced.

The proton scattering is found to have cross sections for the single excitations which are smaller than  $\alpha$  scattering by a factor of about 10 and this is well reproduced by the QPM calculation. The large cross sections in the QPM calculation for states around and above 7 MeV compared to the 5–6 MeV region show the increased isovector character of these excitations, forming a transitional region towards the IVGDR at higher energies. The decay intensity of the involved  $1^-$  states to the first-excited  $2^+$  state is connected to the mixing of the PDR built on the ground state to the PDR built on the first-excited state and, thus, allows for a sensitive test of the degree of mixing. The overall agreement between the experimental data and QPM calculations on an absolute scale for all observables simultaneously is satisfactory and corroborates the present interpretation of the PDR on all its major aspects in a quantitative way. Since each observable is sensitive to a different aspect of the wave function of the excited states, this proves the high accuracy in the detailed modeling of the PDR within the QPM.

It is interesting to observe that the measurements made for another N=82 isotope, the  $^{138}\text{Ba}$  nucleus, was found to provide a similar picture for the excitation of  $1^-$  states [21]. The comparison of  $(\alpha, \alpha'\gamma)$  data for  $^{140}\text{Ce}$  and  $^{138}\text{Ba}$  is given in Fig. 47.

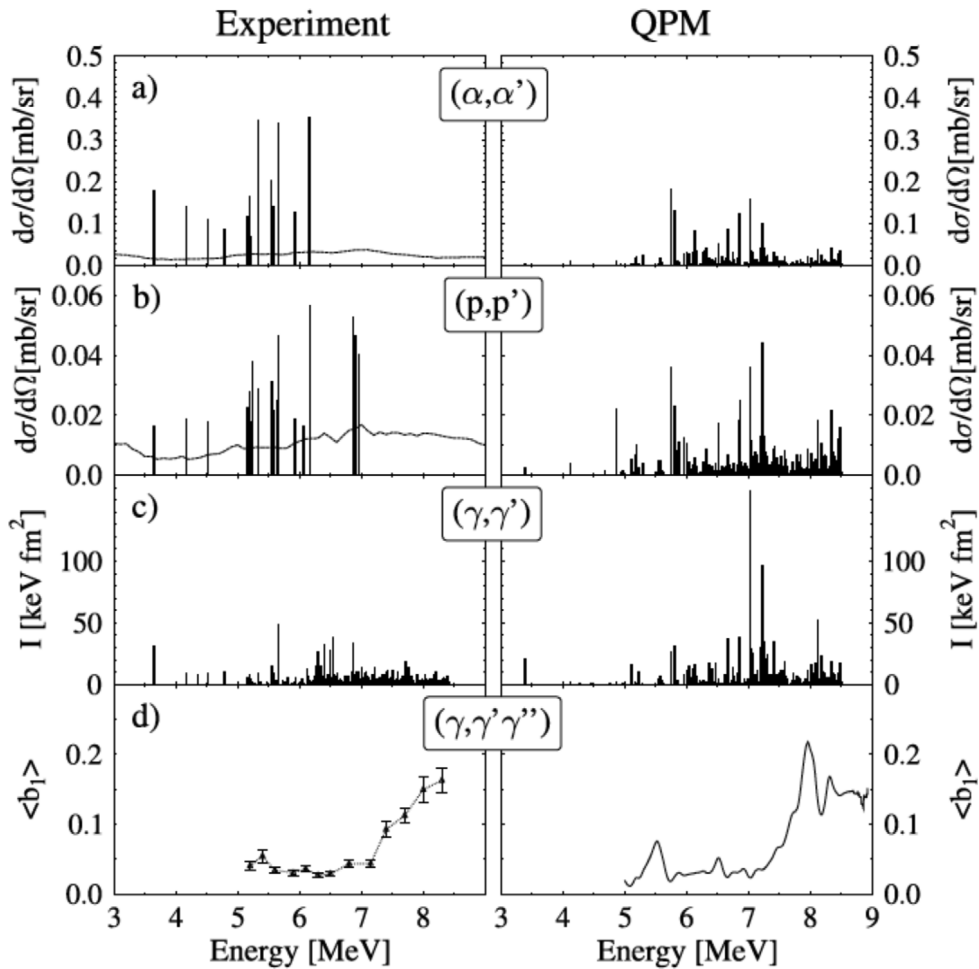


**Fig. 46.** The experimental results on pygmy states in  $^{140}\text{Ce}$  for  $(\text{p}, \text{p}'\gamma)$ ,  $(\alpha, \alpha'\gamma)$  and  $(\gamma, \gamma')$  reactions from [14,30,88,189]. The solid lines in panels (a) and (b) represent the sensitivity limit of the experiments. The lowest panel shows the measured averaged branching ratio to the first excited state from [14]. In the right column, the corresponding calculations within the QPM model are shown.  
Source: From [30].

### 6.7. The isospin character of dipole states in the $^{208}\text{Pb}$ nucleus

Similarly to the case of  $^{90}\text{Zr}$ , the  $^{208}\text{Pb}$  nucleus was first studied in the work of [178] with the  $(\alpha, \alpha'\gamma)$  and showed the presence of isoscalar strength up to around the particle binding energy. A further investigation using higher resolution gamma-ray detectors and another excitation probe was performed using the AGATA detection array and the inelastic scattering of  $^{17}\text{O}$  beams at 20 MeV/A as a probe [27].

The main results of that work are shown in Fig. 48. The leftmost panel gives the measured cross sections averaged over angles (the average angle being  $15.6^\circ$  in the center of mass frame) for E1 transitions. The shaded areas show the sensitivity limit cross section, deduced on the basis of the background present in the spectra. In the bottom part of the left and of the central panel of Fig. 48 values of  $B(\text{E}1)$  deduced from  $(\gamma, \gamma')$  measurements [192] are shown. To be noted that  $(\text{p}, \text{p}'\gamma)$  data of [17] provide, in the region of interest here, results basically identical to those of  $(\gamma, \gamma')$ . Examining the left most panel of Fig. 48 one notes a rather strong reduction of the cross section, appearing at first glance anomalous, for the excitation of E1 states in the 6.5–7.5 MeV as compared with that of the region 4.5–6.5 MeV. This seems to be in contrast with the known  $B(\text{E}1)\uparrow$  values and with the fact that the decrease of the number of virtual photons in such a small excitation energy interval is not expected to account for it. On the other hand, the common finding that the Coulomb excitation cross section for the transitions in the region 4.5–6.5 MeV is much smaller than the data (it accounts for only 20%–30% of the measured values) indicates clearly that these E1 states are excited strongly also by nuclear interaction. This nuclear contribution appears to be different for these two energy intervals and consequently this suggests that the nature of the states is not the same.

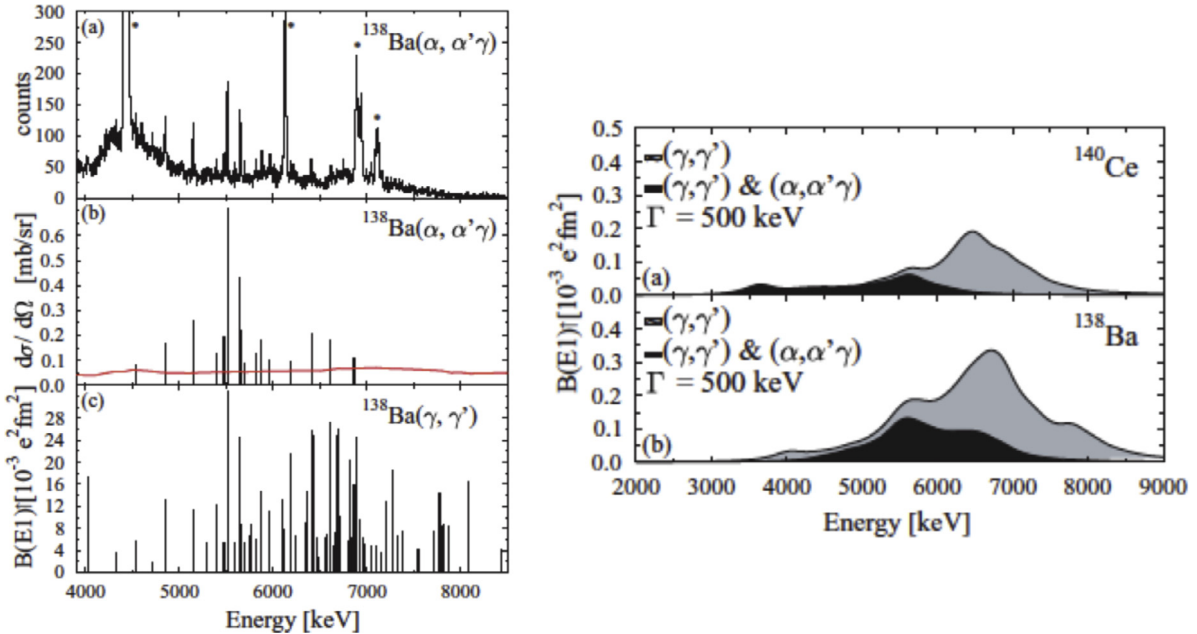


**Fig. 47.** The experimental results on pygmy states in  $^{138}\text{Ba}$  for  $(\alpha, \alpha'\gamma)$  and  $(\gamma, \gamma')$  from [21]. On the right hand side comparison is made with data on  $^{138}\text{Ba}$  with a folding Lorentzian functions with a width of 500 keV.

Source: Adapted from [21].

Another interesting feature of the present experiment is the fact that for the two known closely lying  $1^-$  states at 7.063 MeV and 7.083 MeV, the ( $^{17}\text{O}, ^{17}\text{O}'$ ) reaction populates only the second state and not the first, in contrast with the fact that the  $B(E1)\uparrow$  of the first state is much larger than that of the second. Similarly to what found in the case of  $^{48}\text{Ca}$  [181], this could suggest that these states are originated from an isospin pure level which is then split by isospin mixing.

The population of the  $2^+$  states, given in the central panel of Fig. 48 does not show any anomalous behavior. In this nucleus few  $2^+$  states are in the region of the  $1^-$  states and their identification via gamma decay requires the use of high resolution detectors.

The description of the measured cross section in terms of reaction models is presented in the right panel of Fig. 48. The performed calculations, which are in strong disagreement with the data, were obtained using a standard form factor, namely the isovector GDR type, and are very similar to the Coulomb excitation alone. In contrast, the calculation reproducing the data use a form factor deduced using as a transition density the one reported in the bottom part of the rightmost panel of Fig. 48. The extracted values of the fraction of the isoscalar E1 sum rule for the most intense measured  $1^-$  transitions are 2.6(0.8)% (4.842 MeV), 3.5(0.5)% (5.512 MeV), 0.92(0.23)% (5.292 MeV), 1.69(0.28)% (6.264 MeV). The obtained summed value, including the contribution of all the observed  $1^-$  transitions up to 7.335 MeV, is 9.0(1.5)%, in line with the value reported in [178] and consistent with the fact that most of the isoscalar strength in  $^{208}\text{Pb}$  is around 22 MeV [9]. It should be also pointed out that the fraction of the isoscalar electric dipole sum rule for the 4.842 MeV E1 state was not obtained in the past with  $(\alpha, \alpha'\gamma)$  but only from an analysis reported in [178] of a low resolution measurement of (p,p') scattering.

## 7. The structure of pygmy states from beta decay studies

The E1 strength below the neutron threshold in terms of a state-by-state spectroscopy, including the specific decay branchings, is presently under investigation but much has still to be done in this connection. The knowledge of the decay branchings is on the other hand important to test in detail theoretical predictions.

An opportunity to obtain these crucial  $\gamma$ -ray branching ratios has recently been highlighted by the spectra of  $\gamma$ -rays following  $\beta$  decays which were recorded in total absorption spectrometers (TAGS). In those works considerable population probabilities for high-lying states was found. In particular, the population of levels with energies corresponding to almost the  $Q_\beta$  value (7.626 MeV) was found for some  $\beta$  decays such as  $^{86}\text{Br}$  decaying to  $^{86}\text{Kr}$ . It should also be reminded that  $\beta$  decay prefers to connect levels with similar spin and parity and thus for this particular case being spin and parity of the ground state of  $^{86}\text{Br}$   $J^\pi = 1^-$  it very likely that,  $1^-$  levels associated with the PDR are populated in  $\beta$  decay. One expects this to be in general true for  $\beta$  decays with high  $Q_\beta$  values from parents with low ground-state spin and negative parity. These observations have motivated the work of [193] aiming at determining the structure of  $1^-$  levels exploiting

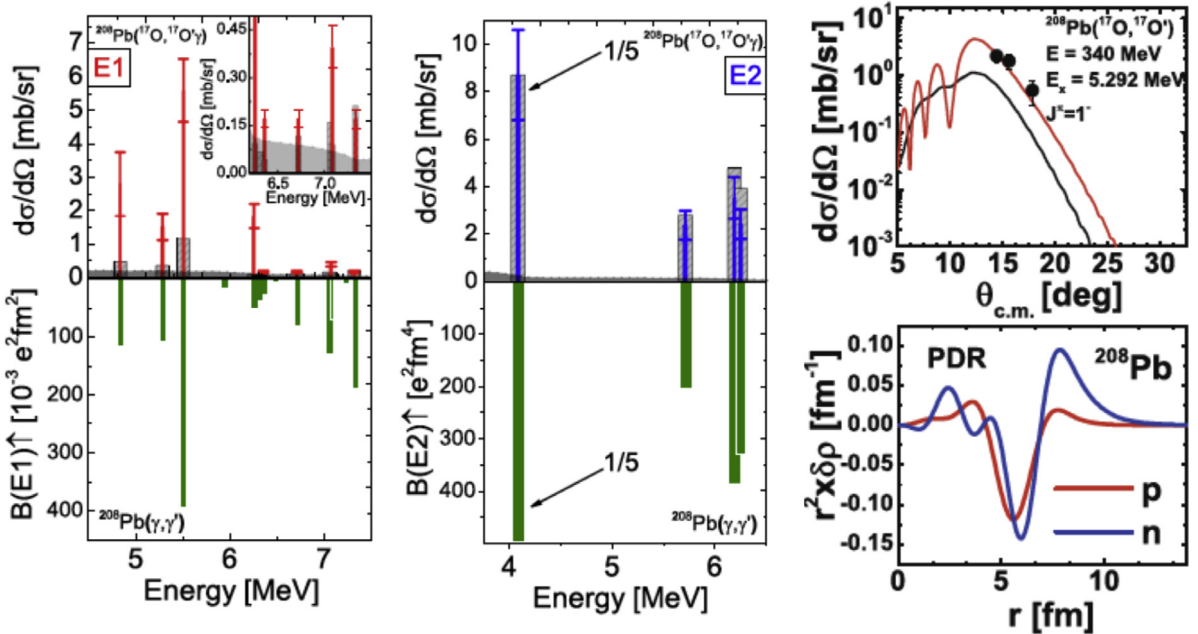


**Fig. 48.** Top left and central panels: the measured differential cross section for E1 transitions (red bars in the left panel) and E2 transitions (blue bars in the right panel) for the nucleus  $^{208}\text{Pb}$ . The inset shows the details in the higher energy region. The dashed bars give calculated DWBA excitation cross sections using  $B(E1)\uparrow$  values from [79] and [192] and standard form factors. The shaded areas show the sensitivity limit of the experiment. Bottom left and central panels: electromagnetic reduced transition strength measured with  $(\gamma, \gamma')$  [192]. Right panels: DWBA calculations in comparison with data using the Coulomb form factor and the microscopic form factors including the transition density shown in the bottom right panel.

Source: Adapted from [27] and [24].

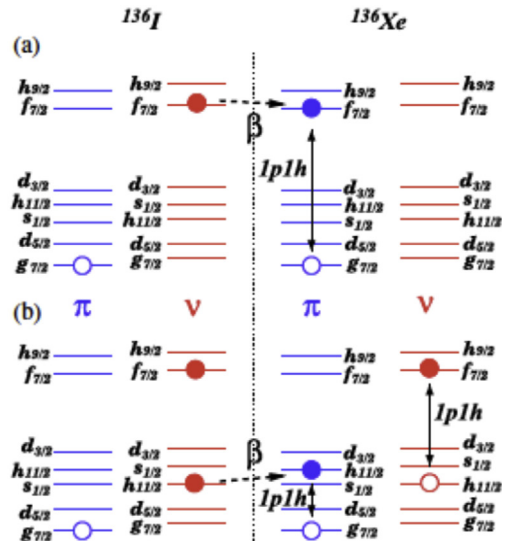
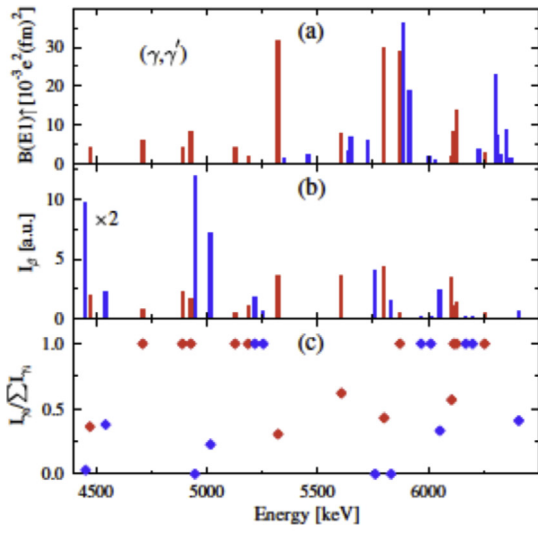


**Fig. 49.** In the left panel candidates for  $1^-$  levels in  $^{136}\text{Xe}$  are shown. Part (a) shows the  $B(E1)\uparrow$  strength distribution of  $1^-$  states as extracted from  $(\gamma, \gamma')$  reaction [95], part (b) shows the relative level population intensity in the  $^{136}\text{I}$   $\beta$  decay and part (c) the ground-state branching ratios extracted from  $\beta$  decay. Levels marked with red bars were populated in both reactions. In the right panel a schematic picture of  $^{136}\text{I}$   $\beta$  decay is given. Part (a) shows the population of a 1p-1h configuration in  $\beta$  decay of a neutron ( $\nu$ ) near the Fermi surface and part (b) shows the population of a 2p-2h configuration in  $\beta$  decay of a neutron initially situated below the Fermi surface. For simplicity, only unpaired particles (full circles) and holes (empty circles) are presented.

Source: Adapted from [193].

the beta-decay process. A considerable number of such  $\beta$  decays are encountered covering different mass regions. Some examples are reported in [193] among which the interesting case of  $^{136}\text{I}$  ( $J_0 = 1^- \rightarrow 1^+$ )  $\rightarrow ^{136}\text{Xe}$  which was studied in detail since data from  $(\gamma, \gamma')$  on  $^{136}\text{Xe}$  are available for comparison. The beta decay of  $^{136}\text{I}$  is characterized by  $Q_\beta = 6.93$  MeV which is sufficient to populate higher-lying  $1^-$ , that were found to exist copiously via  $(\gamma, \gamma')$  measurements. One expects that, due to the selectivity of beta decay, not all the known  $1^-$  states are populated. This is indeed the case as one can see in Fig. 49 where the population via beta decay of high lying states is compared with the experimental  $B(E1)^\dagger$  values. This comparisons evidences that several levels are observed with both techniques. Concerning the experimental features of that it is important to point out that  $\gamma - \gamma$  coincidence events were reported only for levels up to an energy of 4.5 MeV. It was also realized that the assignment of level energies based on  $\gamma$ -ray energies is not unambiguous but on the other hands branches to lower-lying excited states for several levels. These branching transitions were not seen in the  $(\gamma, \gamma')$  measurement because of the background present in the measured spectra in this energy region [95]. However, in the particular case of  $^{136}\text{Xe}$  the  $(\gamma, \gamma')$  spectra indicate that in contrast with  $\beta$ -decay data the branching of the strongly populated 5322-keV level should be much smaller. From Fig. 49 one clearly sees that several  $\gamma$ -ray decays were observed exclusively with one of the two methods. There are experimental reasons to be considered to interpret for this finding. In fact, the missing coincidence information in the  $(\gamma, \gamma')$  prevent to clearly identify transitions leading to the ground state from those leading to lower-lying excited levels and this is particularly true for weak transitions.

Moreover, levels populated in  $\beta$  decay can have an excitation probability in  $(\gamma, \gamma')$  which is too small and thus these  $\gamma$  transitions are below the sensitivity limit or the states decay to excited states and thus difficult to see in  $(\gamma, \gamma')$ . In particular there are two levels (at 4454 and 5016 keV) seen only in  $\beta$  decay which exhibit large branching transitions to lower-lying excited states. Furthermore in some cases the parity of the state could not be well established and was assumed to be negative and if instead the real parity of the state is positive the degree of forbiddenness for beta decay is higher thus reducing the population of the state. In general, one has to remember that it is true that  $\beta$ -decay data provide valuable spectroscopic information but this is limited to the excitation window given by  $Q_\beta$  and it is well known that not all  $1^-$  levels are below  $Q_\beta$ .

It is interesting to examine the details of the nuclear structure of states involved in the  $\beta$  decay and this was done by restricting it to Fermi type decays. The starting point is that as compared with  $^{136}\text{Xe}$  in its ground state, the nucleus  $^{136}\text{I}$  has an extra neutron in the  $|f\rangle = |2f_{7/2}\rangle$  level and a proton hole in the  $|g\rangle = |1g_{7/2}\rangle$  level which couple to the  $1^-$  total angular momentum. Therefore the ground state of  $^{136}\text{I}$  can be seen as the lowest energy  $1^-$   $ph$  phonon built on top of the  $^{136}\text{Xe}$  ground state. The QRPA calculation predicts that this state has an almost pure ( $> 99.9\%$ )  $[vf, \pi g^{-1}]_{1^-}$  particle-hole configuration. If only  $1p-1h$  excitations in the daughter nucleus are considered, then the Fermi  $\beta$  decay of the neutron in the  $f$  level leaves  $^{136}\text{Xe}$  in either  $[\pi f, \pi g^{-1}]_{1^-}$  or in the  $[vf, vg^{-1}]_{1^-}$  excited states, as schematically illustrated in Fig. 49. Another possibility is that a neutron in some other subshell may also undergo a  $\beta$  decay leaving the daughter nucleus in the  $2p-2h$  excited state (see Fig. 49). The probability of finding the daughter nucleus in these particular  $1p-1h$  and  $2p-2h$  configurations was predicted to be of the same order. The level  $|j\rangle$  located between the  $f$  and the  $g$  levels allows it to have simultaneously a neutron hole and proton particle. To interpret this type of data the QPM model was extended to describe the  $\beta$  decay of odd-odd nuclei to excited states of even-even nuclei. Previous  $\beta$ -decay studies dealt with even-even mother nuclei. These calculations for odd-odd nuclei predicted that the states with a strong  $[vf_{7/2}, vg_{7/2}^{-1}]$  configuration in their wave function should be well excited in both reactions. Some levels (at 5322, 5801, and 5872 keV) exhibit this feature in the two different measurements. One can think that the levels strongly excited in  $(\gamma, \gamma')$  but not populated in  $\beta$  decay are probably dominated by other neutron configurations. At the same time, one can expect that levels observed in  $\beta$  decay only (those at 4454 and 5016 keV in this case) are good candidates to be two-phonon states. This conclusion is also supported by the corresponding weak decay to the ground state. The experimental study of level-population probabilities in  $\beta$  decays of Fermi type and its interpretation within the QPM provides an alternative insight into the microscopic structure of the wave functions of  $1^-$  levels.

Since  $\beta$  decay represents an additional probe for PDR studies it is important to extend these studies for Gamow Teller (GT)  $GT\beta$  decay. Indeed in the case of neutron rich nuclei the  $GT\beta$  decay is the dominant process. Madurga et al. [195] report on the  $\beta$  decay of  $^{83}\text{Ga}$ , where high-energy states in the daughter  $^{83}\text{Ge}$  are populated following GT selection rules. The energy spectra of  $\beta$  delayed neutrons from  $^{83,84}\text{Ga}$  decays are clearly constrained by the underlying nuclear structure, as opposed to a structureless level-density dependence.

The measurement of the gamma-rays following  $\beta$  decay up to an energy of approximately 10 MeV was made for the  $^{80,83}\text{Ga}$  nuclei (with  $Q_\beta = 10.3$  and 11.7 Mev, and neutron separation energy  $S_n$  of 8.1 and 3.6 MeV, respectively) using the radioactive beams [194]. The  $\gamma$  spectra obtained using  $\text{LaBr}_3$  detectors in coincidence with a  $\beta$  particle detected in the cylindrical plastic scintillator surrounding the point in which the beta decaying nucleus is implanted. Keeping in mind the value of the neutron separation energy one expects gamma-ray emission up to 4 MeV. In contrast, the measured energy spectrum was observed to extend up to approximately 9 MeV with a broad structure after 5 MeV. These events were found to be compatible with  $^{83}\text{Ga}$  half life (see bottom part of Fig. 50). The  $^{83}\text{Ga}$   $\beta$ -delayed neutron emission probability was measured to be between 56(7)% and 85(6)% of the total decay strength and a contribution from  $^{83}\text{Ga}$   $\beta n$  was excluded since in that case no  $\gamma$ -rays were reported above an energy of 3.4 MeV. After the needed experimental check it was concluded that the photons in the energy interval between 5 and 9 MeV should originate from levels in  $^{83}\text{Ge}$  at high energy which can be populated in the  $\beta$  decay of  $^{83}\text{Ga}$ .

The relative  $\gamma$ -ray branching was estimated to be 16(4)%. This value, when normalized to the  $2.0(4)\text{MeV}^{-1}$   $B(\text{GT})$  deduced from neutron emission in  $^{83}\text{Ga}$ , corresponds to an average integrated  $B(\text{GT})$  going through  $\gamma$  radiation of 0.4(1)

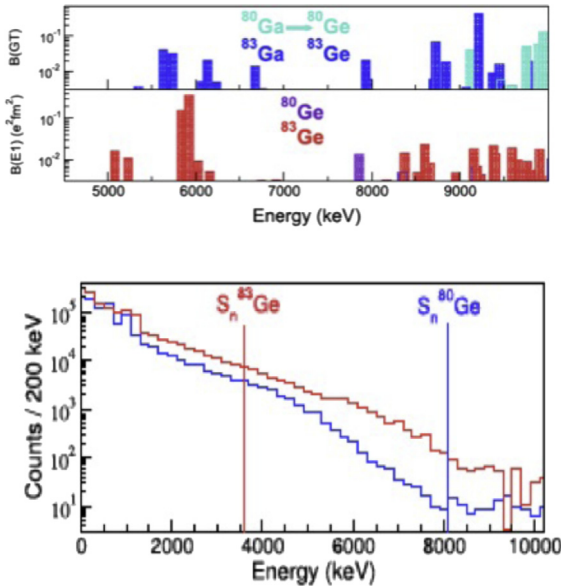


**Fig. 50.** Bottom panel: the  $\gamma$ -ray energy spectrum as measured in coincidence with  $\beta$  electrons from the decay of  $^{80,83}\text{Ga}$ . The neutron separation energies of the daughter nuclei  $^{80,83}\text{Ge}$  are also indicated. The two spectra are normalized to the same number of  $\beta$ -decay events. Top panel: GT $\beta$ -decay and E1 strength distributions from microscopic Gogny-QRPA calculations.

Source: Adapted from [194].

MeV<sup>-1</sup> (strength that has escaped observation in the past and was previously attributed to the low-lying  $^{83}\text{Ge}$  states). While significant  $\gamma$  branching ratios from neutron-unbound states up to 2 MeV in less exotic nuclei were attributed to a high centrifugal barrier sampled by neutrons, here  $l$  can be as low as 1 and thus the centrifugal barrier effects are less relevant. A hindrance of neutron emission can come from core-neutron removal spectroscopic factors [194]. State-of-the-art microscopic QRPA calculations (see top part of Fig. 50) show that the beta decay of Gamow-Teller type involving deeply-bound neutrons could trigger coherent dipolar oscillations (PDR) which in turn gives rise to a sizable emission of E1  $\gamma$  radiation. The process is favored by the rapid development of a neutron skin beyond the N = 50 neutron shell closure. However, a better quantification of the process and of its evolution with neutron number need to be made to support this simple interpretation. New measurements in the future, also with high resolution detectors could be enlightening.

In general, studies of high energy photon emission in neutron rich matter are important not only to understand the reduction of the measured first-forbidden  $\beta$ -decay probabilities but are also relevant for reactor physics and related topics.

## 8. Further aspects

### 8.1. The dipole response and the nuclear level density

The impact of the low-energy part of the strength function of E1 type on astrophysical reaction rates involved in the nucleosynthesis r-process has been discussed extensively (see e.g. Refs. [8,142,196,197]). In this connection in order to obtain the reaction rates in stellar environment, one needs to know the gamma strength function (GSF) and the level density (LD) and moreover one needs to ascertain the validity of the Brink-Axel hypothesis for gamma-rays with energy in the region of nucleon binding energy. There issues and their direct links to the nuclear dipole response are discussed in this section.

The gamma strength function describes the average gamma decay behavior of an excited nucleus. It is given for electric or magnetic transitions  $X\epsilon(E, M)$  with multipolarity  $\lambda$  by the following expression:

$$f^{X\lambda}(E_\gamma, J) = \frac{2J_0 + 1}{(\pi\hbar c)^2(2J + 1)} \frac{\langle \sigma_{abs}^{X\lambda} \rangle}{E_\gamma^{2\lambda-1}} \quad (21)$$

with  $\langle \sigma_{abs}^{X\lambda} \rangle$ ,  $E_\gamma$ ,  $J$  and  $J_0$  being respectively the photoabsorption cross section, the gamma-ray energy, and the spin of the excited and ground states. Although all electromagnetic multipoles contribute in principle to the gamma strength function, it was found that the dipole radiation gives the dominant contribution with the electric dipole radiation E1 being much larger than the magnetic dipole radiation M1. Above the particle emission threshold the GSF is governed by the isovector giant dipole resonance while at low energy the GSF consists in the sum of the low energy tail of GDR and of the pygmy dipole resonance.

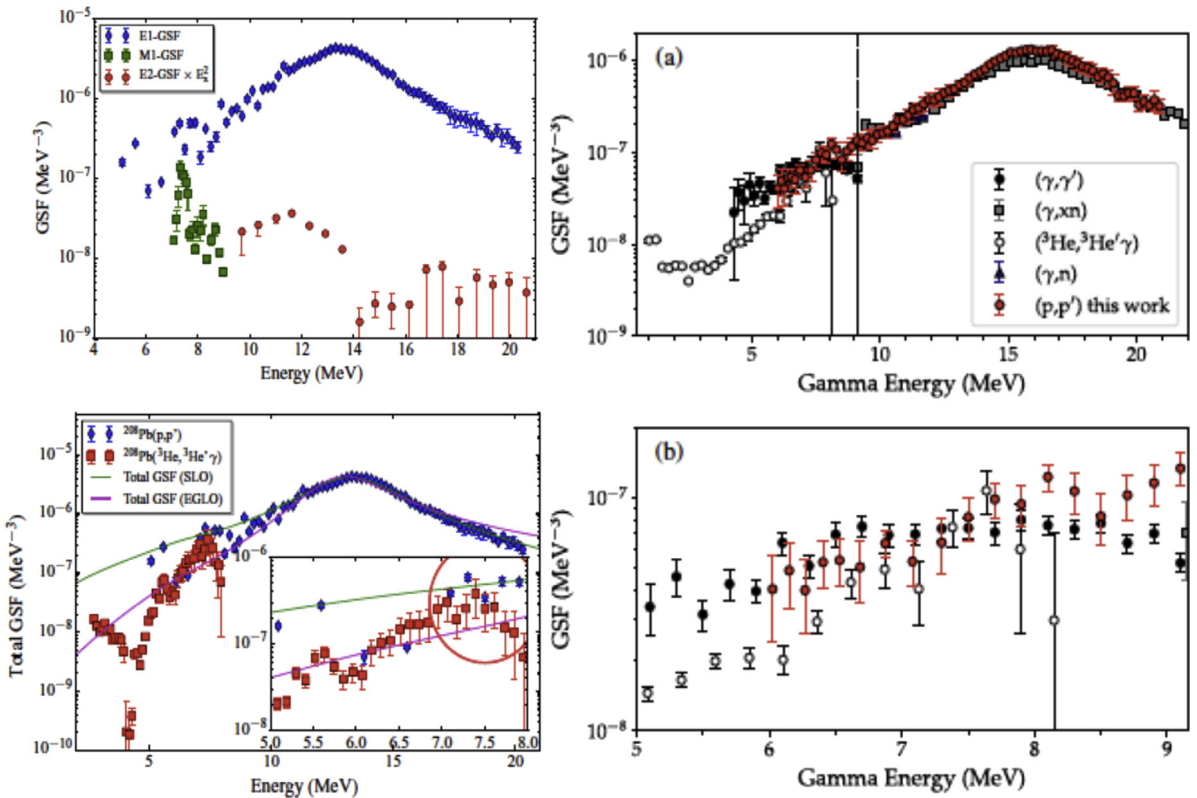


**Fig. 51.** Bottom left: Total GSF of  $^{208}\text{Pb}$  from the  $(\text{p},\text{p}')$  data [17] and [18] in comparison to the reanalyzed results from the Oslo experiment [199]. The inset shows an expanded view of the low-energy region, between 5 to 8 MeV. Top left panel: E1, M1, and E2 contributions to the GSF of  $^{208}\text{Pb}$  [200]. Right top panel (a): GSF of  $^{96}\text{Mo}$  from [52] (red circles) compared with  $(^3\text{He}, ^3\text{He}'\gamma)$  from [201] and [202] (open circles),  $(\gamma, \text{xn})$  [203] (gray squares),  $(\gamma, \text{n})$  [204], (blue upward triangles), and  $(\gamma, \gamma')$  [205] data including a statistical model correction for unobserved branching ratios (black circles). Right bottom panel (b) Expanded range from 5 MeV to neutron threshold [52].

Source: Adapted from [52] and [200].

The Brink–Axel hypothesis states that the GSF is the same independently of the properties of the initial and final states and thus should be the same in gamma emission or absorption experiments. For gamma-ray transitions in the region of the GDR (see also discussions in the following sessions) the Brink–Axel hypothesis is well fulfilled up to the region of temperature 1.2–3.5 MeV as deduced from extensive work on the GDR in hot rotating nuclei formed in fusion evaporation reactions. The existing work also shows that the statistical model describes well the de-excitation process of highly excited nuclei. In the case of a stellar scenario, as that in which the r-process is taking place, the reaction of interest is the absorption of gamma-rays at energy much lower than that of the GDR and mainly in the region around the particle emission threshold. In addition, these absorption reactions occur in nuclei whose initial state can be an excited state and thus the importance of the use of the Brink–Axel hypothesis to make predictions. However, recent studies suggest possible deviations from the Brink–Axel hypothesis due to nuclear structure effects that could be still present at low temperatures (see [96,198]). This finding is in contrast with others [52] supporting the complete validity of the Brink–Axel hypothesis.

The combined study of the gamma strength function and of the level density was made using measurements of the  $(\text{p},\text{p}')$  cross sections at incident laboratory energy  $E_{\text{beam}} = 295$  MeV and at extreme forward angles for the nuclei  $^{208}\text{Pb}$  and  $^{96}\text{Mo}$  [200,206]. The data deduced from the  $(\text{p},\text{p}')$  excitation cross sections are compared with data obtained from cross sections for gamma and neutron decays and for the  $(\gamma, \gamma')$  reactions for two nuclei  $^{208}\text{Pb}$  and  $^{96}\text{Mo}$  in the right top and two bottom panels of Fig. 51. To be noted that in general below excitation energy of 6 MeV the data from  $(^3\text{He}, ^3\text{He}'\gamma)$  obtained at low energy differs from the  $(\text{p},\text{p}')$  data. The  $(^3\text{He}, ^3\text{He}'\gamma)$  data from the Oslo group (see Ref. [202]) are the results obtained after applying to the measured spectra an analysis technique based on difference spectra sensitive to the product of the level density and gamma-ray strength function. The lines in the left bottom panel of Fig. 51 show the prediction based on a Standard Lorentzian function (SLO)

$$f_{\text{SLO}}(E) = \frac{\sigma_r \Gamma_r}{3(\pi \hbar c)^2} \frac{\Gamma_r E}{(E^2 - E_r^2)^2 + (\Gamma_r E)^2} \quad (22)$$

where  $\sigma_r$  is the peak cross section,  $E_r$  and  $\Gamma_r$  are the centroid energy and the width of the IVDGR. The prediction of the more sophisticated model, the Enhanced Generalized Lorentzian (EGLO) is also shown in the figure and reproduces

better the experimental data. The EGLO prediction consists of two terms, a Lorentzian with an energy and temperature dependent width and a term describing the shape of the low energy part of the Gamma Strength Function.

The level density of nuclear states can be extracted from the experimental ( $p,p'$ ) data by using the fluctuation analysis technique. The main steps for this analysis, which can be applied only if the data contains events from one type of states only ( $1^-$  in this case), are here given. The application of the fluctuation analysis technique is based on two assumptions:

(i) in a highly excited nucleus the probability for a given spacing between states characterized by the same values for spin and parity is given by the Wigner distribution [206]:

$$P_W(s) = \frac{\pi s}{2} \exp\left(-\frac{\pi s^2}{4}\right) \quad (23)$$

with  $s = D/\langle D \rangle$  the ratio between the actual level spacing and the mean level spacing. This distribution has a maximum close to the mean value and show a suppression of small distances between neighboring levels.

(ii) The ground state decay widths or transition strengths obey a Porter-Thomas distribution

$$P_{PT}(s) = \frac{1}{\sqrt{2\pi}s} \exp\left(-\frac{s}{2}\right) \quad (24)$$

with  $s = \Gamma/\langle \Gamma_0 \rangle$ . These assumptions are the same adopted for the Random Matrix Theory (RMT) (see Refs. [207,208]) and rely on the observation that they reproduce nuclear excitation in the energy region around the neutron separation energy [209]. The procedure of the fluctuation analysis, consisting mainly in four steps, is illustrated in a schematic way in the left panel of Fig. 52. To get level density from fluctuations one needs to eliminate the contribution to fluctuations arising from finite statistics and this is done by folding the data at each point with a Gaussian function with a value of width  $\sigma$  chosen to be smaller than the experimental energy resolution. This spectrum is denoted as  $g(E_x)$  (see second panel from the top in the left part of Fig. 52). A second spectrum  $g_>(E_x)$  is created by convoluting the data with a Gaussian function with a value of  $\sigma_>$  which is at least two times larger than the experimental energy resolution in order to remove gross features from the spectrum. Generally stable results correspond to  $\sigma = 0.5 \Delta E$  and  $\sigma_>/\sigma = 2.5$  to 3.5. The dimensionless stationary spectrum  $d(E_x) = g_>(E_x)/g(E_x)$  is shown in the third panel from the top in the left part of Fig. 52. The normalization on the local mean value results in the vanishing of the energy dependence of the cross sections. The quantity  $d(E_x)$  displays sensitivity to the fine structure of the spectrum and it is distributed around an average intensity  $d(E_x) = 1$ . With increasing excitation energy the mean level spacing decreases, and in turn the oscillations of  $d(E_x)$  are damped. With the autocorrelation function

$$C(\epsilon) = \frac{\langle d(E_x)d(E_x + \epsilon) \rangle}{\langle d(E_x) \rangle \langle d(E_x + \epsilon) \rangle} \quad (25)$$

one can obtain a quantitative description of the fluctuations. Here  $\epsilon$  gives the energy shift between the spectra. The value  $C(\epsilon = 0) - 1$  represents the variance of  $d(E_x)$ :

$$C(\epsilon = 0) - 1 = \frac{\langle d^2(E_x) \rangle - \langle d(E_x) \rangle^2}{\langle d(E_x) \rangle^2} \quad (26)$$

This quantity is shown in panel (d) of Fig. 52. The mean level spacing  $\Delta D$  is proportional to the variance of  $d(E_x)$  and can be extracted from the value of  $C(\epsilon = 0) - 1$ . The nuclear level density can then be determined from the mean level spacing as  $\rho(E) = 1/\Delta D$ . The result of this procedure for the case of  $^{208}\text{Pb}$  is in the right panel of Fig. 52.

The next step is to deduce the total level density and this was achieved using the following expression:

$$\rho_{tot}^{PT}(E) = \frac{2\rho_{tot}(E, J, \Pi)}{f(J)}, \quad (27)$$

where  $\rho_{tot}(E)$  is the total level density at energy  $E$  and  $\rho_{tot}(E, J, \Pi)$  is the level density for transitions with spin  $J$  and parity  $\Pi$ . The spin distribution is given by the function  $f(J)$  defined as,

$$f(J) = \frac{2J+1}{2\sigma^2} \exp\left[-\frac{(J+1/2)^2}{2\sigma^2}\right] \quad (28)$$

where  $\sigma$  is the spin cutoff parameter which depends on the parameters of the Fermi gas model. Parameter sets derived within the back-shifted Fermi gas model (BSFG) approach [210] and [211]. These include those from [199] usually adopted in the analysis of the Oslo experiments, a global set recommended in RIPL-3 [214], and the parametrization of Ref. [210] providing a good description of level density for many nuclei near the valley of stability and especially developed for network calculations of reactions involved in the s-process. In the case of the analysis shown in the right panel of Fig. 52 the average value of the three parametrizations was used. To be noted that the error bars include this model dependence which actually dominates over the uncertainties in the extraction of the  $1^-$  level density with the fluctuation analysis.

It has been particularly important to obtain the level density in  $^{96}\text{Mo}$  in the region of the PDR using the described approach, well tested for the nucleus  $^{208}\text{Pb}$ . Indeed for  $^{96}\text{Mo}$  conflicting results have been found for the gamma strength function from the  $(\gamma, \gamma')$  measurements and from those obtained by the Oslo group which assumes validity of the Brink-Axel hypothesis. This result is shown in Fig. 51 where the data for  $^{208}\text{Pb}$  (covering here also the energy below binding

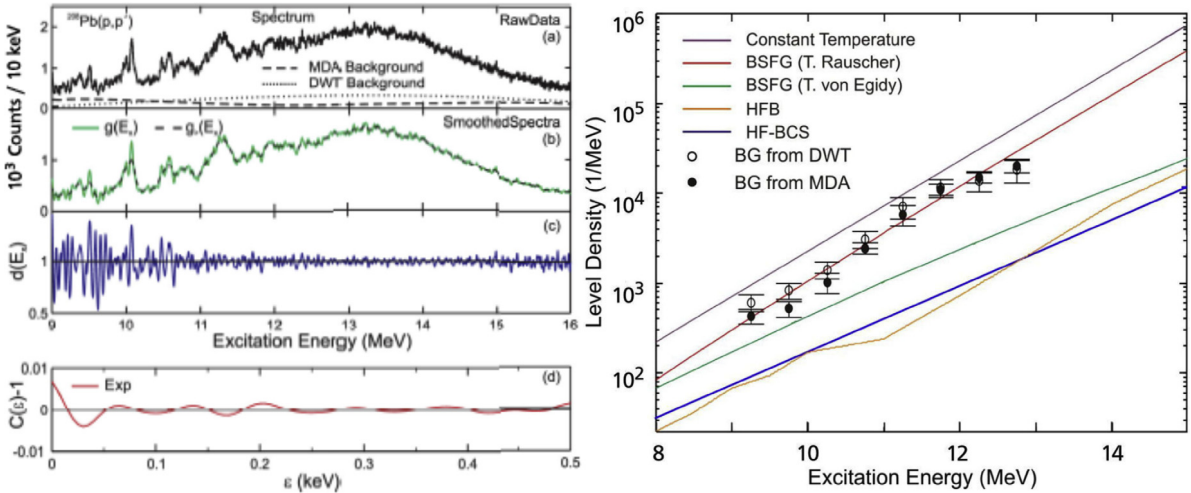


**Fig. 52.** Left panels (a) Spectrum of the  $^{208}\text{Pb}$  ( $p,p'$ ) reaction at  $E_0 = 295$  MeV and angles from  $0^\circ$  to  $0.94^\circ$  and the background obtained from MDA (dashed line) and discrete wavelet transform (DWT) of the spectrum decomposition (dotted line). (b) Background subtracted smoothed spectra  $g(E_x)$  and  $g_{>}(E_x)$ . (c) Stationary spectrum  $d(E_x)$ . (d) Experimental autocorrelation function. Right panel shows the comparison of the experimentally obtained level densities for  $1^-$  states in  $^{208}\text{Pb}$  in the energy range 9–12.5 MeV with predictions from (top to bottom at  $E_x = 15$  MeV) the constant temperature model [108] (purple line), the BSFG model using the parameters of Ref. [210] (red line) and the parameters of [211] (green line), HFB [212] (orange line), and HF-BCS [213] (blue line).

Source: Adapted from [206].

energy) are also shown. In addition, it was found that the extracted gamma strength function agrees with results of compound nucleus  $\gamma$  decay experiments [201,202] supporting validity for the Brink–Axel hypothesis in the energy region of the PDR, in contrast to results from the  $(\gamma, \gamma')$  reaction [205] and the claims of Ref. [96]. The data have allowed the extraction of the level density at excitation energies around the neutron threshold up to approximately 13 MeV, a region which is hardly accessible by other methods. The test of the general validity of the Brink–Axel hypothesis in the region of the pygmy resonance requires however a more systematic comparison of the GSF derived from  $\gamma$  absorption and emission experiments over a broad range of nuclei. In particular, the role played by deformation needs to be explored.

One interesting feature found in the GSF of a number of nuclei is the presence of an unexpected rise at around 3 MeV which is visible in the data presented in the bottom panel of Fig. 53. In the case of medium mass nuclei this effect (also called upbend) was found to be even more pronounced.

An unexpected enhancement of the GSF for low transition energies ( $E_\gamma < 3$  MeV) was discovered more than a decade ago in the iron isotopes  $^{56,57}\text{Fe}$  [215]. This feature was not predicted by any theoretically derived GSFs; in fact the GSF data showed an enhancement of more than a factor of 10 compared to typical models for the E1 strength [215].

The most recent data on NLDs and GSFs of  $^{56,57}\text{Fe}$ , which were extracted from  $(p, p'\gamma)$  coincidences, are shown in Fig. 54 in comparison with data from other reactions using heavier projectiles and thus populating higher spin states. Two different normalization procedures were used. For the nucleus  $^{56}\text{Fe}$  the upbend was experimentally shown to be of dipole nature in [221] from a measurement of the angular distribution of the gamma-rays. Taking into account the presence of strong Porter–Thomas fluctuations, there is no indication of any significant excitation-energy dependence in the  $\gamma$ -ray strength function, in support of the generalized Brink–Axel hypothesis and consistently with what was found with the same method in the heavy nucleus  $^{238}\text{Np}$  [222].

It is important to remind that an enhancement at around 3 MeV was also found in many medium-mass nuclei, including  $^{43,45}\text{Sc}$  [223,224],  $^{60}\text{Ni}$  [225],  $^{73,74}\text{Ge}$ , and Mo isotopes [201,226,227]. To date, the heaviest nuclei where the upbend has been seen are  $^{138,139}\text{La}$  and  $^{151,153}\text{Sm}$  [221].

After the upbend was independently confirmed in  $^{95}\text{Mo}$  [226] using a different technique, theoretical investigations of the origin of this phenomenon were made. Within the thermal-continuum quasiparticle random-phase approximation, the upbend was explained as due to E1 transitions caused by thermal single-quasiparticle excitations in the continuum, with its strength depending on the nuclear temperature. On the other hand, shell-model calculations [228,229] show a strong increase in  $B(M1)$  strength for low-energy M1 transitions. At present,  $^{60}\text{Ni}$  is the only case where experimental data favor a magnetic character of the upbend [225].

## 8.2. Isospin symmetry at finite temperature

In the experiments described in the previous sections the isospin mixing induced by the Coulomb interaction is the mechanism responsible of the E1 decay from excited dipole states characterized by a strong isoscalar nature. Here the

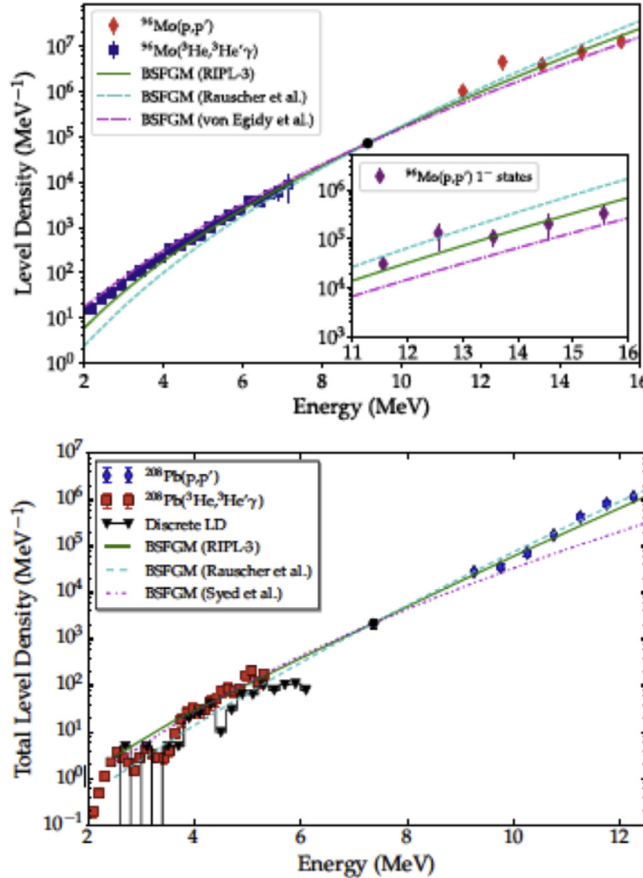


**Fig. 53.** Top panel: Total LD in  $^{96}\text{Mo}$  deduced from the fine structure of the ( $\text{p}, \text{p}'$ ) data in the energy region of the IVGDR (red diamonds) compared with the results from the ( $^3\text{He}, ^3\text{He}'\gamma$ ) Oslo experiment (blue squares) from [201,202]. The black circle point stems from s-wave resonance neutron capture [203]. BSFG models normalized to the value at Sn are shown as green solid [214], cyan dashed [210], and purple dashed-dotted [211] lines. The inset shows the LD of 1<sup>-</sup> states in comparison with absolute predictions of the models [52]. Bottom panel: Total LD from the ( $\text{p}, \text{p}'$ ) data for  $^{208}\text{Pb}$  [23,24] in comparison to the reanalyzed results from the Oslo experiment [199]. The black downward triangles are results from counting the levels identified in Ref. [52] in 200 keV bins. The magenta dashed-dotted, green solid, and cyan dashed lines are BSFG model predictions with the parameters of Refs. [210,214], and [211].

Source: Adapted from [52] and [200].

question of isospin mixing as probed by the E1 decay is further addressed focusing on the gamma decay of dipole oscillations at finite temperature. As a consequence of the Brink–Axel hypothesis the nuclear dipole vibration was found to be a common feature of all nuclei at all temperatures and this excitation mode can be easily induced by an external electric field. The research on the properties of the GDR at finite temperature has been very extensive in the last 30 years and it was motivated by the interesting problems of the evolution of shapes and of the damping mechanisms with temperature and angular momentum. For some of the latest works in this research area the reader is referred, for instance, to [230], the review [48] and references therein. Here below we concentrate on how the decay from the GDR at finite temperature can provide information on the isospin mixing (see Fig. 55).

The concept of charge symmetry and charge independence is formalized via the introduction of isospin quantum number  $I$ . This quantum number is fully preserved by the charge independent part of the nuclear interaction. However, the presence of the electromagnetic interaction and the charge dependent short range interaction break the isospin symmetry in nuclei. The most important part of the isospin symmetry breaking comes from the isovector Coulomb interaction which produces mixing of states separated by  $\Delta I = 0$ . The question of isospin impurity in nuclei, despite being a small effect, has been a long-standing open problem in nuclear physics. It is well known that the isospin impurity affects the properties and the spreading width of the Isobaric Analog States (IAS) and the superallowed Fermi decay of the  $N \approx Z$  nuclei near the proton drip line. The spreading width of the IAS  $\Gamma^\downarrow$  is directly related to the isospin mixing of the parent nucleus and is found to be originated by the Coulomb interaction coupling these states to the continuum. Instead, in case of the superallowed Fermi decay, the measured lifetime is related to the vector coupling constant  $G_V$  which is connected to the u-quark to d-quark transition matrix element  $V_{ud}$  of the Cabibbo–Kobayashi–Maskawa theory for the weak interaction

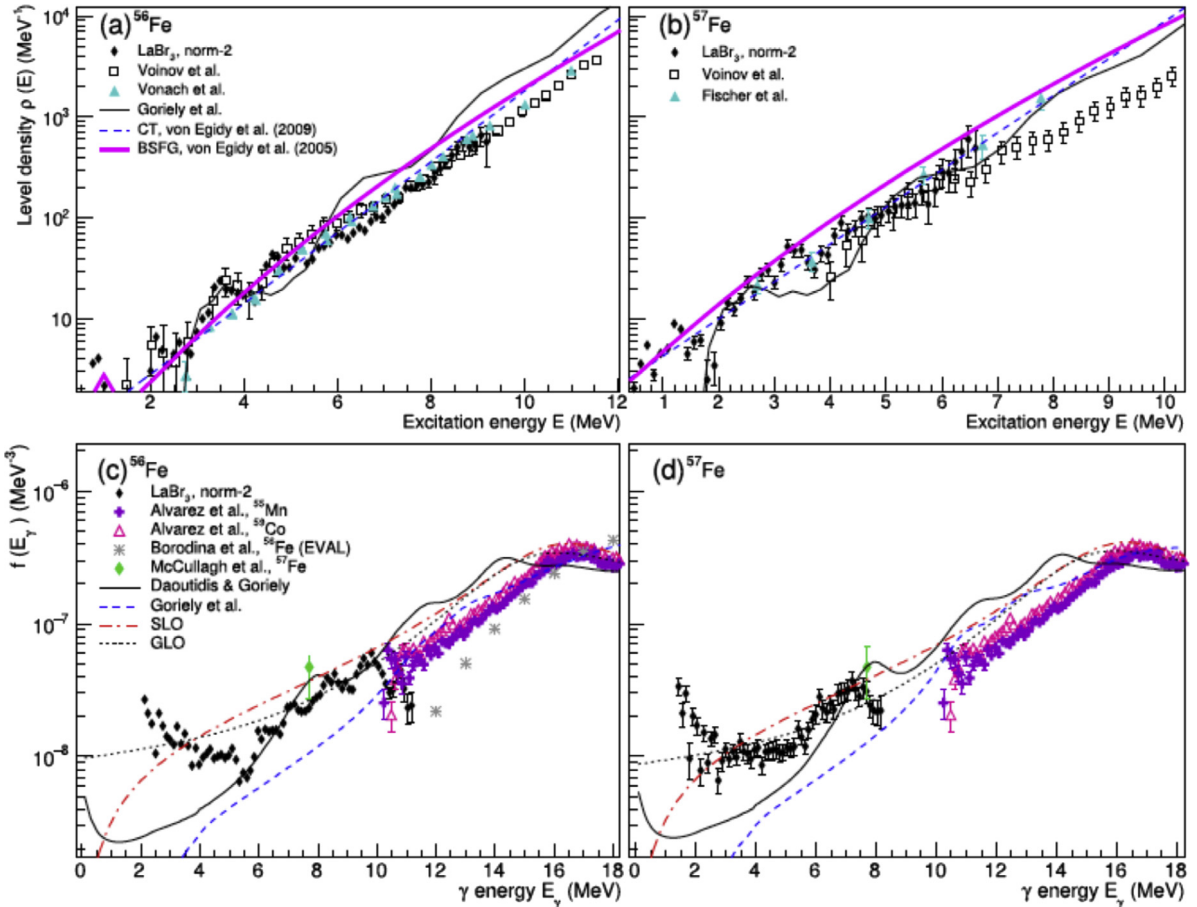


**Fig. 54.** Comparison of GSFs from different reactions for (a)  $^{56}\text{Fe}$  and (b)  $^{57}\text{Fe}$ . Photonuclear data are taken from [216], and the evaluated  $^{56}\text{Fe}(\gamma, n)$  cross section from [217]. Also the  $^{57}\text{Fe}$  E1 + M1 strength at  $E_\gamma > 7.7$  MeV from resonant  $(\gamma, n)$  neutron time-of-flight measurements are shown [218,219], and [220]. For  $^{56}\text{Fe}$  data cover the interval 2.1–11.3 MeV. For  $^{57}\text{Fe}$  data cover the interval 1.4–8.2 MeV. The photonuclear data from [216] are for  $E_\gamma > 10.2$  MeV.

Source: Adapted from [40].

among quarks. The isospin impurity of the nuclear wavefunction has implications in the Fermi transition decay rates, since corrections have to be made to account for it, and thus on the evaluation of the transition matrix element term  $V_{ud}$ .

In general the breaking of isospin symmetry can be observed by decays, which would be forbidden by the selection rules if isospin mixing were not to occur. Results on this problem were indeed obtained in Fermi  $\beta$ -decay, in the measurements of the Isobaric Analog States (IAS) splitting as deduced from  $\beta$ -delayed  $\gamma$ -rays and via the measurement of the E1 decay from self-conjugate nuclei. Since the E1 decays are isovector (within the long wavelength approximation) the consequence is that transitions of E1 type are forbidden from a nuclear state characterized by isospin  $I=0$  to a final state also characterized by isospin  $I=0$ , this being the case of  $N=Z$  nuclei. Thus if one measures E1 transitions among discrete states in  $N=Z$  nuclei one can deduce the isospin mixing. Indeed it is the  $I = 1$  component of the wavefunction, due to the isospin mixing induced by the Coulomb interaction, that allow the E1 decay. The experimental value of the isospin mixing deduced for a single state amounts to  $2.5^{+1}_{-0.7}\%$  and it was found in  $N=Z=32$   $^{64}\text{Ge}$  nucleus. The experiment involved the detection of a gamma-ray transition from a  $5^-$  to a  $4^+$  state for which the E1 character was deduced from angular distribution and a polarization measurement. The gamma-ray transition had an energy of about 1.6 MeV and, being this energy in the very low energy tail of the E1 response, the measured transition was very small.

This property of the E1 decay can be fully exploited by going in the gamma-ray region of the Giant Dipole Resonance where the maximum strength of the E1 transitions is concentrated. This approach was employed for the E1 decay of the GDR in nuclei at finite temperature  $T$ , formed in fusion evaporation reactions and the obtained result was also used to demonstrate the E1 character of the high energy gamma-rays emitted in compound nucleus reactions. Self-conjugated Compound Nuclei (CN) at high excitation energy can be formed using fusion-evaporation reactions. The use of self-conjugated projectile and target ensures population of CN with isospin  $I=0$  and thus with E1 decay from the GDR which is hindered. In contrast, if the initial state is not pure in isospin but contains an admixture of  $I=0,1$  states, it can decay

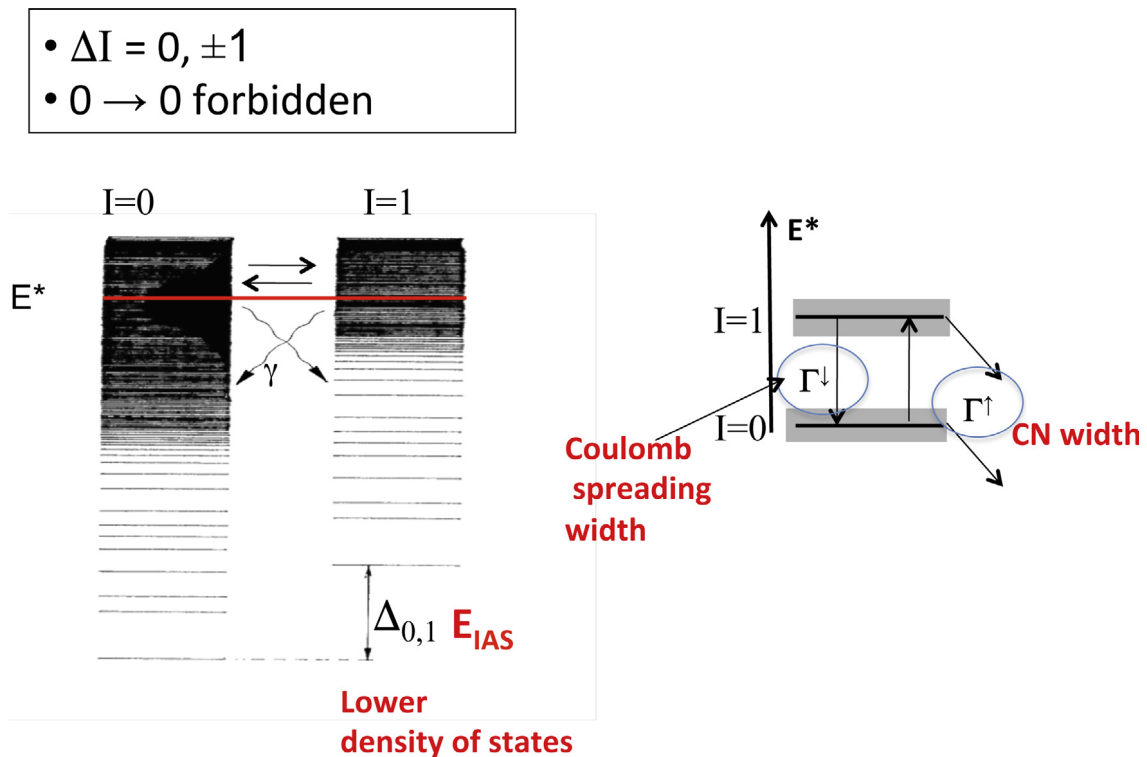


**Fig. 55.** Schematic illustration of the decay from the GDR in a Compound Nucleus described in terms of two sets of levels, one with isospin 1 and the other with isospin 0. The CN has a lifetime that compete with the mixing of states with different isospin induced by Coulomb interaction, as illustrated in the right part of the figure.

to the more numerous final states with isospin  $I=0$ . This is because the gamma decay from the GDR in compound nuclei follows the statistical law implying that emission occurs mainly at the first stage of the decay chain. Gamma-ray emission after particle decay comes from states with no longer isospin  $I=0$ . Particularly interesting is to investigate isospin mixing at finite temperature in different mass regions and in nuclei with  $N=Z$  and the mass region  $A=80-100$ , more difficult to reach, allows to test isospin mixing model predictions in a region where there are the largest discrepancies among them.

At finite temperature there is an additional effect, that of a partial restoration of the isospin symmetry. This is because the degree of mixing in a compound nucleus is limited by its finite lifetime for particle decay [231]. Nuclei at finite temperature are formed as compound nuclei using very often fusion reactions. It has to be noted that at high excitation energy, the compound nucleus, whose lifetime is determined primarily by the strong interaction, should not live long enough for the isospin symmetry to be broken by the relatively weak Coulomb interaction. In the work of Harney, Richter and Weidenmüller [232] it is proposed that compound nuclear isospin mixing should be characterized by an isospin violating spreading width which is approximately constant with mass number and excitation energy, and this was deduced from a large body of data where the spreading widths scatter over more of one order of magnitude. These values of the isospin-violating spreading widths are found to be similar to those deduced from the analysis of the Isobaric Analog States (IAS). The concept of a constant isospin-violating spreading width leads to a definite expectation concerning to the excitation energy dependence of isospin mixing within a given nucleus. At energies where the compound nuclear decay width is much larger than the level spacing, compound nuclear reaction theory implies that the mixing should depend on the ratio of isospin violating spreading width and the compound nuclear decay width. This ratio decreases with increasing excitation energy since the compound nucleus decay width becomes larger while the isospin violating spreading width stays constant. A more refined modeling of the isospin mixing as a function of temperature containing additional effects is reported in [231]. The results within this model are presented and discussed below in connection with the experiments here discussed.

One important point in these investigations is that the statistical model analysis of the experimental data, when isospin is a quantum number of interest, has to take into account that the system has two classes of isospin values which differ by one unit, as in the case of  $I=0$  and  $I=1$ . In the following expressions the lower indices denoted by  $<$  and  $>$  are used for several quantities. In particular, for states with lower isospin value we use  $<$  and higher isospin value we use  $>$ . For the decay cascades of the compound nucleus one needs to evaluate at each step of the decay the isospin mixing quantities

$\alpha_{>(<)}^2$  for the mixing of states of different isospin values:

$$\alpha_{>(<)}^2 = \frac{\Gamma_{>(<)}^\downarrow / \Gamma_{>(<)}^\uparrow}{1 + \Gamma_{>(<)}^\downarrow / \Gamma_{<(>)}^\uparrow + \Gamma_{<(>)}^\downarrow / \Gamma_{>(<)}^\uparrow} \quad (29)$$

where  $\Gamma_>^\uparrow$  is the statistical decay width of the compound nucleus. The  $\Gamma_>^\downarrow$  is the isospin violating spreading width defines as :

$$\Gamma_>^\downarrow = 2\pi |\langle I_> | H_{Coul} | I_< \rangle|^2 \rho(I_<) \quad (30)$$

and the relation between  $\Gamma_<^\downarrow$  and  $\Gamma_>^\downarrow$  as deduced from the principle of detail balance is given by:

$$\Gamma_<^\downarrow = \Gamma_>^\downarrow \frac{\rho(I_>)}{\rho(I_<)} \quad (31)$$

where the level density  $\rho(I_>)$  (in this case for I=1) is larger than  $\rho(I_<)$  (in this case for I=0).

The mixed population of the compound nuclear states are defined in the following by:

$$\tilde{\sigma}_< = (1 - \alpha_{<}^2) \sigma_< + \alpha_{>}^2 \sigma_> \quad (32)$$

and

$$\tilde{\sigma}_> = (1 - \alpha_{>}^2) \sigma_> + \alpha_{<}^2 \sigma_<. \quad (33)$$

In the above expressions  $\tilde{\sigma}_<$  and  $\tilde{\sigma}_>$  are the population cross sections of the pure isospin states (with lower and upper isospin value, respectively). The statistical model calculations for the reaction leading to I=0 compound nucleus contain  $\Gamma_>^\downarrow$  as the only free parameter since all the others are taken from a fit to the reference reaction data.

After the first experiment of M. Harakeh et al. [233] the most recent works on the isospin mixing at finite temperature were made for the  $^{32}\text{S}$  [234] and  $^{80}\text{Zr}$  compound nuclei [235,236].

The experiment to extract isospin mixing in  $^{32}\text{S}$  was performed using the fusion reaction  $^4\text{He}+^{28}\text{Si}$  at  $E_{beam} = 38$  MeV having  $I=0$  for both target and projectile and thus leading to a compound nucleus with  $I=0$  and the reaction  $^4\text{He}+^{27}\text{Al}$  at  $E_{beam} = 35$  MeV having a target with  $I=1/2$  and thus used as a reference reaction [234]. Indeed the mass, excitation energy and angular momentum of the compound nuclei are very similar and this implies that the isospin-violating spreading width, to be deduced from experimental data of gamma decay of the GDR, is the different quantity between the two reactions. In addition, for these reactions the critical angular momentum above which noticeable effects on the GDR width are observed is above  $11 \hbar$  for  $^{32}\text{S}$  and therefore the gamma-ray spectra are expected to be sensitive to temperature only. The main features of the experimental set up used in that experiment was the additional measurement of the coincidence fold distribution of low energy gamma rays and the detection of neutrons. With the measurement of the fold of low energy transitions one can select a specific part of phase space of the angular momentum (usually that at the higher values) and can reduce significantly the background events. The measurement of the energy of the neutrons evaporated by the compound nucleus, in that experiment made through the measurement of the time of flight (ToF), is used to check the value of the level density. In fact the latter enters in the statistical model analysis of both gamma-ray and neutron spectra.

In Fig. 56 the high-energy  $\gamma$ -ray spectra from the two reactions  $^4\text{He}+^{28}\text{Si}$  (at  $E_{beam} = 38$  MeV) and  $^4\text{He}+^{27}\text{Al}$  (at  $E_{beam} = 35$  MeV) used to obtain the isospin mixing in the nucleus  $^{32}\text{S}$  are shown (left panel) together with their ratio (right panel) in comparison with statistical model calculations corresponding to three different values of isospin violating width with the best fitting value  $\Gamma_>^\downarrow = 24$  keV. This value is about twice the one found for  $^{80}\text{Zr}$  but fall in the systematics which is shown in Fig. 57. From this figure one can see that the isospin violating Coulomb spreading width does not have a marked dependence on temperature. The values of Coulomb spreading width deduced from the gamma decay of the GDR at finite temperature are consistent with what found for isobaric analog states at zero temperature.

The experiments performed to obtain the isospin mixing in  $^{80}\text{Zr}$  used the fusion reactions  $^{40}\text{Ca}+^{40}\text{Ca}$  at  $E_{beam} = 136$ , 200 MeV leading to compound nuclei with  $I=0$ . Similarly to the case of  $^{32}\text{S}$  also in this case data were taken with the same experimental setup for a reference reaction, namely  $^{37}\text{Cl}+^{44}\text{Ca}$  at  $E_{beam} = 95$ , 153 MeV which gives rise to a yield of E1 gamma-rays not hindered by isospin selection rules. For the measurement at the higher excitation energy the recoiling compound nuclei and the charged particles were measured (see [235]) in addition to the high energy gamma-rays. In the case of the reactions leading to compound nuclei at the lower excitation energy the measurement of low energy gamma-rays was also made to identify the population of the residual nuclei. Both techniques resulted in an efficient and clean identification of fusion evaporation events and this is an important prerequisite if one wants to describe the measured high energy gamma-ray yield with the statistical model. This point is illustrated in Fig. 58 where the used statistical model reproduces also residual nuclei populations for different conditions of coincidence folds, reflecting a selection in the phase space related to the angular momentum of the compound nucleus.

To show the importance of measuring a reference reaction in the same experimental conditions, one should examine Fig. 59 displaying data obtained with the reactions  $^{40}\text{Ca}+^{40}\text{Ca}$  at  $E_{beam} = 200$  MeV and  $^{37}\text{Cl}+^{44}\text{Ca}$  at  $E_{beam} = 153$ . The details of the comparison between data and calculations can be seen in this figure. Data and prediction are shown in a linear scale

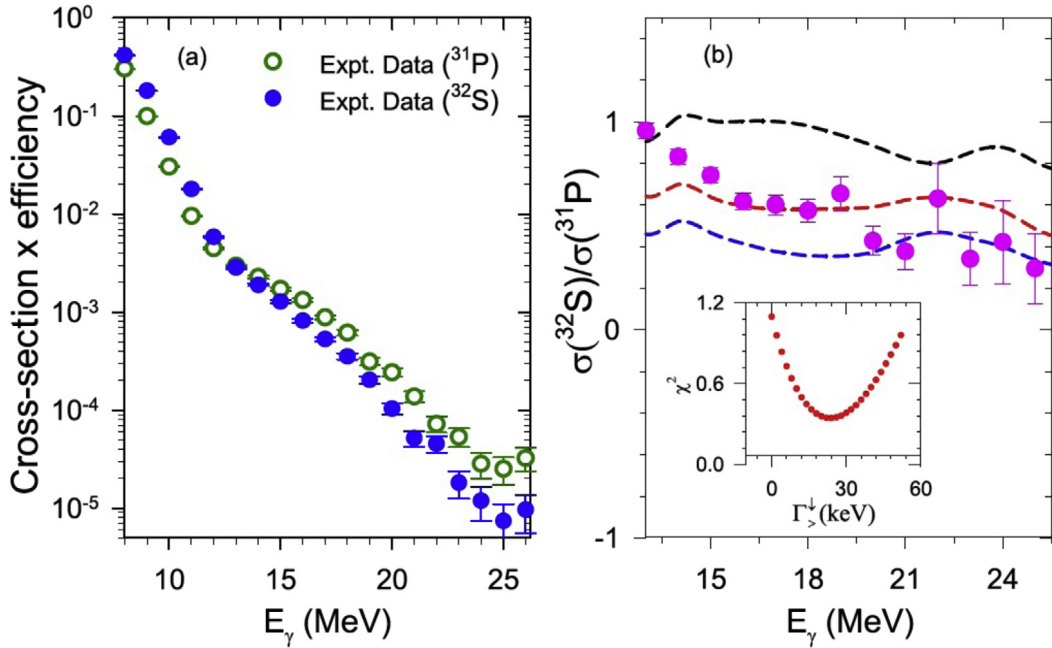


**Fig. 56.** (a) Experimental data for  $^{31}\text{P}$  (green open circles) and  $^{32}\text{S}$  (blue filled circles). (b) Experimental ratio (pink filled circles) of the high energy  $\gamma$ -ray cross sections of  $^{32}\text{S}$  and  $^{31}\text{P}$  along with the CASCADE predictions for different values of the Coulomb spreading width, 0 for blue dashed line (zero mixing), 24 keV for red dashed line and 10 MeV for black dashed line (full mixing). In the inset of part (b) it is shown the Chi-square as a function of the Coulomb spreading width.

Source: From [234].

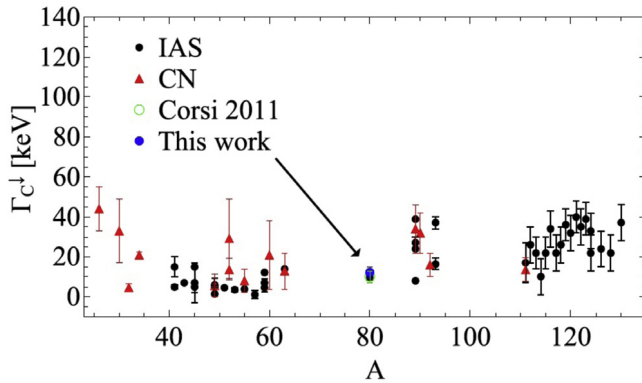


**Fig. 57.** Values of the Coulomb spreading width obtained in the IAS (black dots) data and data from the CN (red triangles). The arrow points to data from Refs. [237] and [235], overlapping with the value obtained in [235] (empty green dot, Corsi 2011 in the legenda).

Source: Adapted from [237].

following the linearization procedure which is usually applied in the study of the GDR in hot nuclei [48]. Statistical model calculations made without isospin mixing ( $\Gamma_c^\downarrow = 0$  keV), with the value of  $\Gamma_c^\downarrow = 10$  keV yielding the best fit and with a large mixing ( $\Gamma_c^\downarrow = 100$  keV) are compared with data. In support of the interpretation of the results, the small change in the yield of  $^{40}\text{Ca} + ^{40}\text{Ca}$  reaction was checked to see if it could be due to a different width of the GDR and not to isospin mixing. The opening of more first-step  $\gamma$ -decay channels induced by the isospin mixing has the same effect on the calculated  $\gamma$  spectra as the use of a  $\sim 1$  MeV smaller GDR width  $\Gamma_{GDR} = 9.7$  MeV. The best fitting value of  $\Gamma_{GDR}$  for  $^{80}\text{Zr}$  was then used for  $^{81}\text{Rb}$ . The results displayed in Fig. 59 show that indeed the  $\sim 1$  MeV change in  $\Gamma_{GDR}$  can mimic the effect of the isospin mixing in  $^{80}\text{Zr}$  but gives rise to an inconsistent result for the  $^{81}\text{Rb}$  spectrum, the latter not being reproduced with this smaller  $\Gamma_{GDR}$  value.

With the result obtained for the isospin mixing at finite temperature, the value at zero temperature was derived using the model of Ref. [231], which describes the variation of the mixing probability with temperature T. The isospin mixing

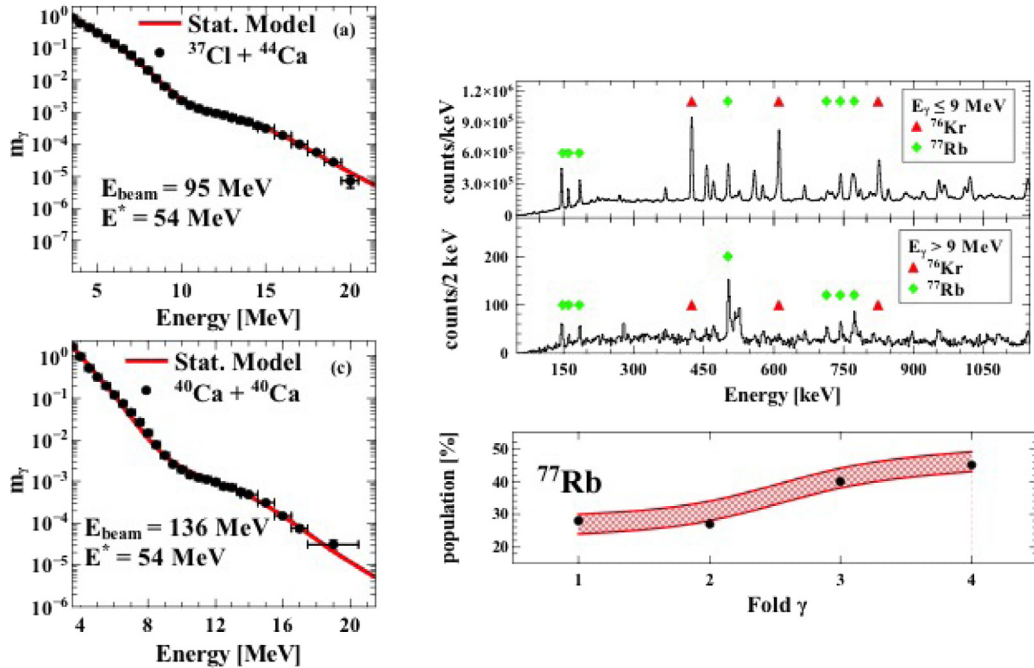


**Fig. 58.** Left panels: high energy \$\gamma\$-ray spectra for the reactions \$^{37}\text{Cl} + ^{44}\text{Ca}\$ (a) and \$^{40}\text{Ca} + ^{40}\text{Ca}\$ (c). The data, measured with LaBr<sub>3</sub>:Ce detectors, are shown with full circles in comparison with the best fitting statistical model calculations (red lines). Right panels: \$\gamma\$-ray energy spectra from the decay of the <sup>80</sup>Zr CN from AGATA array and obtained for two different conditions on the energy measured in coincidence with LaBr<sub>3</sub>:Ce detectors. The \$\gamma\$ transitions of two different residues are indicated with the triangle and diamond symbols. Bottom panel: population of the <sup>77</sup>Rb residue for different values of the measured fold of \$\gamma\$-ray coincidences. Experimental values are displayed with filled circles while the red lines are the statistical model predictions. The dashed area were obtained by varying the level density parameter from 7.5 to 8.5.

Source: Adapted from [236].

probability for a nucleus at finite temperature is defined as

$$\alpha_>^2(T) = \frac{1}{I_0 + 1} \frac{\Gamma_{IAS}^\downarrow}{\Gamma_{CN}(T) + \Gamma_{IVM}(IAS)} \quad (34)$$

where \$\Gamma\_{IAS}^\downarrow\$ is the Coulomb spreading width of the IAS, to be considered equal to \$\Gamma\_>^\downarrow\$, \$\Gamma\_{IVM}(IAS)\$ is the width of the Isovector Monopole Resonance (IVM) at the excitation energy of the IAS, which is expected to be constant with T. According to the systematics for the present case one has \$\Gamma\_{IVM}(IAS) = 240 \text{ keV}\$ [231,235,238]. \$\Gamma\_{CN}(T)\$ is the CN decay width increasing with temperature.

In the top panel of Fig. 60 the values of isospin mixing coefficient \$\alpha\_>^2\$ calculated using Eq. (34) are shown as a function of temperature T. The red line is obtained with a value of \$\Gamma\_>^\downarrow = 11 \pm 2.1 \text{ keV}\$, corresponding to the average of the two experimental values (the lower and upper curves corresponding to 8.9 and 13.1 keV, respectively). This calculation gives, at T = 0, \$\alpha\_>^2 = 4.6\% \pm 0.9\%\$, in rather good agreement with the prediction shown with the blue triangle from Ref. [239]. Following the discussion in Ref. [231], a weak linear dependence on T of the Coulomb spreading width was considered, namely \$\Gamma\_>^\downarrow(T) = \Gamma\_>^\downarrow(1 + cT)\$. In this expression the chosen slope parameter \$c = 0.1 \text{ MeV}^{-1}\$ is such that the value of \$\Gamma\_>^\downarrow\$ lays within the experimental error bar. The blue band in Fig. 60 displays the dependence of \$\alpha\_>^2\$ with T for such weak dependence of \$\Gamma\_>^\downarrow\$ (the limiting curves correspond to 8.9 and 13.1 keV). Two calculations were also made using \$\Gamma\_>^\downarrow = 11 \text{ keV}\$ and \$\Gamma\_{IVM}(IAS) = 220\$ and 260 keV and it was found that these two curves are well within the two colored bands of Fig. 60.

It is very interesting to connect the isospin mixing parameter \$\alpha\_>^2\$ to the isospin-correction term \$\delta\_C\$. As reported in Ref. [240] the quantity \$\delta\_C\$ is defined as:

$$\delta_C = 4(I+1) \frac{V_1}{41\xi A^{2/3}} \alpha^2 \quad (35)$$

where \$V\_1 = 100 \text{ MeV}\$ and \$\xi = 3\$, while \$\alpha^2\$ is the isospin impurity in the ground state and I is the isospin of the nucleus.

Using Eq. (35) the value \$\delta\_C = 0.81(16)\%\$ was obtained for <sup>80</sup>Zr. This value is shown in the bottom panel of Fig. 60 with the red star. In this figure the dashed black line is the prediction from the Damgaard model [241], while the red line is a shell model with Saxon-Woods radial wave function prediction [242]. Black circles are the experimental points extracted

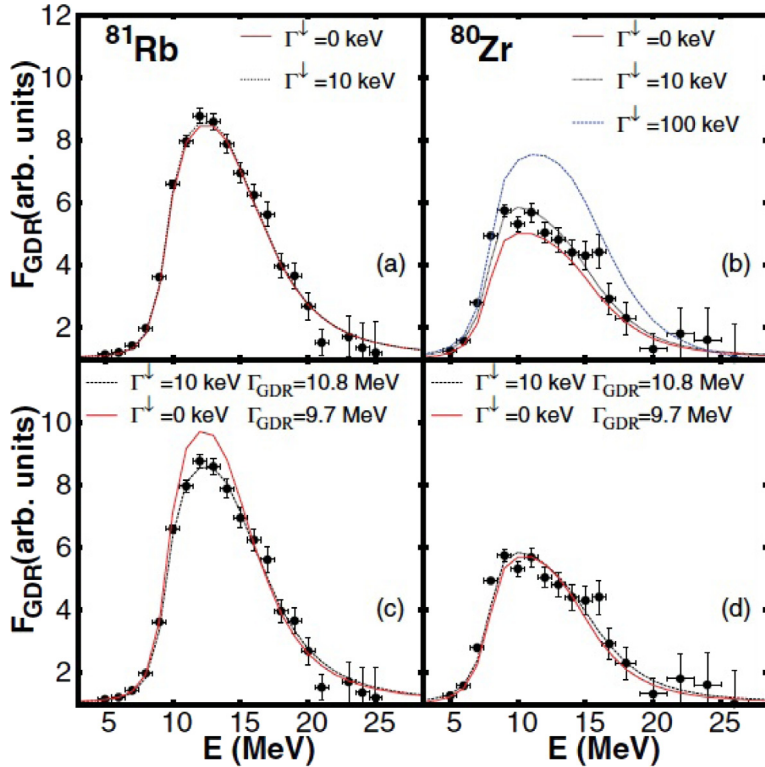


**Fig. 59.** Spectra obtained by dividing data and the best fitting calculations by a statistical spectrum evaluated with constant  $B(E1)$ . In this way one can visualize the details in the region of interest in a linear scale. The left panels refer to  $^{81}\text{Rb}$  while the right panel to  $^{80}\text{Zr}$ . In the top panels the set of GDR parameters obtained as described in the text ( $E_{\text{GDR}}= 16.2$  MeV,  $\Gamma_{\text{GDR}}=10.8$  MeV, and  $S=90\%$ ) is adopted together with different values of the Coulomb spreading with  $\Gamma_{>}=0$  (red line), 10 (black line), 100 (blue line, plotted only for  $^{80}\text{Zr}$ ). In the bottom panels, data are compared with the statistical model calculation of the top panel width  $\Gamma_{>}=10$  keV (black line) and with a statistical model calculation without isospin mixing (red line) but with a different set of GDR parameters (in particular a smaller  $\Gamma_{\text{GDR}}=9.7$  MeV).

Source: Adapted from [235].

form  $\beta$  decay as reported in Ref. [243], the blue triangle is the value obtained from the mass measurement in Ref. [244]. It is important to note that the quantity  $\delta_C/l+1$  is plotted in Fig. 60 since  $\beta$ -decay measurements are for  $I=1$  nuclei, while that for  $^{80}\text{Zr}$  is  $I=0$ . The result found for  $^{80}\text{Zr}$  is consistent with the data for  $^{74}\text{Rb}$  and follows the predicted trend. No calculations of the type of Ref. [243] are available for  $A=80$  and the  $\delta_C$  data for  $^{74}\text{Rb}$  are the only existing ones close to  $N=Z=40$ .

## 9. Summary and conclusions

The understanding of the electric dipole modes in nuclei, of their manifestations and of their implications on a number of global nuclear properties has driven a very fertile research activity that started many decades ago and continued vigorously during the years. The research in this field has received a particular boost in the last 15–20 years and this went hand-in-hand with the major experimental developments and improvements of theoretical models.

The wealth of interesting results on this topic has demonstrated that this simple mode is a very useful tool to gain insight into different nuclear properties. This review paper has primarily addressed the question of isospin properties of dipole states, concentrating in particular in the region below neutron separation energy. To large extent it is complementing, also for the time span, the previous review paper by D. Savran et al. [1].

In summary the following physical questions were discussed in terms of main results and achievements obtained so far and pointing out the need of future investigations.

- The study of the isovector dipole response (both PDR and GDR) using Coulomb excitation via proton inelastic scattering has been shown to be very powerful for providing stringent tests to the nuclear equation of state, needed to describe neutron stars. This is because the polarizability, that receives a sizable contribution also from the PDR region, was deduced with good precision. The size of the neutron skin, whose properties are similar to those of the neutron star crust, was obtained for few neutron rich nuclei, including one unstable nucleus. To challenge theory further, the

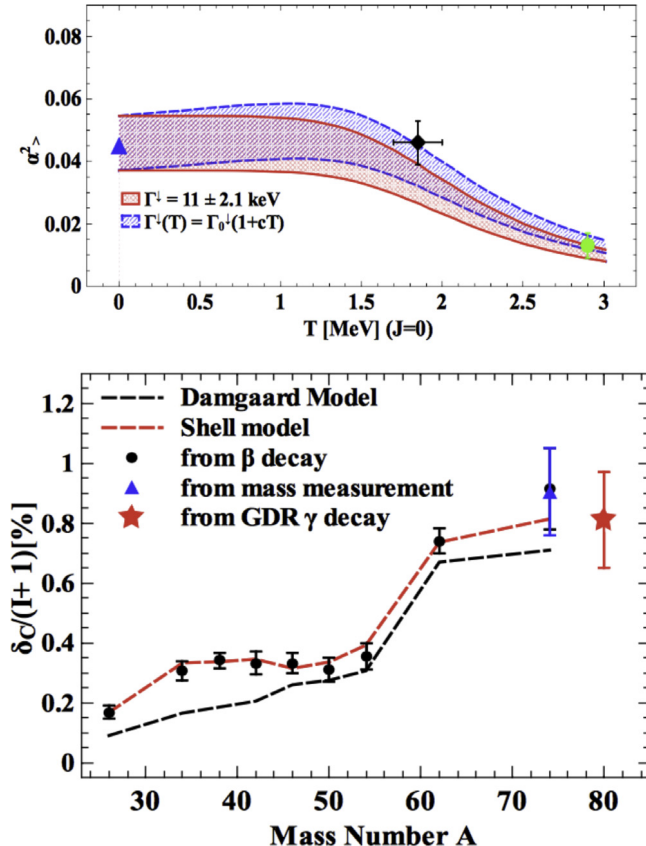


**Fig. 60.** Top panel. The isospin mixing  $\alpha_{>}^2$  as a function of  $T$  obtained with the procedure of [231] corresponding to  $\Gamma^{\downarrow} = 11 \pm 2.1$  keV (red region), constant with  $T$ . For the blue band  $\Gamma^{\downarrow}$  was assumed to vary mildly and linearly with  $T$  (see text). The blue triangle is the theoretical value at  $T = 0$  from [239], the green circle is the datum from [235], the black diamond is the datum from [236]. Bottom panel. The isospin mixing correction  $\delta_c$  as a function of the nuclear mass number  $A$ . The dashed black line is the prediction from the Damgaard model [241], while the red line is a shell model with Saxon-Woods radial wave function prediction [242]. Black circles are the experimental points extracted from  $\beta$  decay as reported in Ref. [243], the blue triangle is the value obtained from the mass measurement in Ref. [244]. The red star is the value of  $\delta_c$  reported in [236]. Source: Adapted from [236].

ongoing and future experimental efforts are devoted to measure with good precision decays and branching ratios (gamma and particles from the GDR).

- The study of the fine structure of the PDR states via electromagnetic probes (with the NFR technique) is addressed in all mass regions to pin down the important features of these states. The strength of electric dipole states was found to be larger in neutron rich nuclei and its fragmentation depends on level density. The latest major efforts are devoted to the measurements and understanding of branching ratios and to try to reach some of these states via beta decay.
- The study and the isospin character of the PDR has been driven by the urgent need to understand the nature of these electric dipole states. For this aspect, many theoretical efforts were dedicated to the understanding of some of its intrinsic properties, as collectivity or isospin mixing, among others, as well as to describe the experimental data. Indeed PDR states are characterized by unique properties, different than a single-particle transition but also considerably different than highly collective giant resonances. The general macroscopic picture is rather complex, ranging from the simplest neutron skin oscillation to toroidal motion, isoscalar and isovector mixing, etc. Many experiments with nuclear beams probing the nuclear surfaces were made, a few also with radioactive beams. Evidence for isoscalar character for the low lying pygmy states in few nuclei was found. The determination of the isoscalar strength and the interpretation of the measured cross sections was possible thanks to the developments in nuclear theory taking into account the interplay of nuclear structure and nuclear reaction effects. The efforts made up to now have addressed different mass regions and have indicated the need to excite these states with different probes and to measure their decay branching ratios. Much more work is ongoing and expected to advance the understanding of the nature of dipole states. The challenge for the future is determining the transitions from skin oscillation to highly collective oscillations (GDR).

- The measurement of the GDR with high energy resolution has allowed to deduce the nuclear level density, a quantity that has a major impact in the computation of nucleosyntheses. These studies, together with those using other experimental techniques, are also testing the widely used and well checked principle that the GDR exists also on excited states (compound nuclei). The present open question is the validity of this principle in general for all low-lying dipole states since specific nuclear structure effects might show up.
- Isospin mixing was probed via the decay of the GDR in hot compound nuclei with N=Z. It was shown that these studies allow for the determination of the isospin mixing corrections in mass regions not yet accessible with other methods. This correction is needed for the beta decay theory which involves the CKM matrix. Up to now the mass region 30 and 80 were studied with the  $\gamma$ -decay of the GDR in compound nuclei. New studies are needed to make this method more widespread and they will be carried out in the near future.

It is clear that the ongoing experimental and theoretical efforts on the questions reported above are key steps for exciting future research at the new facilities with radioactive beams and gamma beams. As shown in this work, most of the experimental information was obtained for stable nuclei. It is also clear from this review that the presence of the low-lying dipole states is strictly related to the presence of neutron excess. Therefore the study of the PDR for nuclei far from the stability line should be carried out in the future with several experiments providing data necessary to shed light on the unresolved problems and to confirm the present findings.

The awareness on the information richness that the dipole nuclear modes bear has increased during the years the attraction to these studies and will surely do so also in the next future.

## Acknowledgments

We would like to thank H. Sagawa for helpful discussion. The work of A. T. has been supported by the following grant: JSPS KAKENHI Grant No. JP14740154 and MEXT KAKENHI Grant No. JP25105509.

**Table 2**  
A list of acronyms most used in this paper.

Acronym	Meaning
AGATA	Advanced Gamma Tracking Array
BSFG	Back Shifted Fermi Gas
DSSD	Double Side Silicon Drift
DWBA	Distorted Wave Born Approximation
EDF	Energy Density Functional
EDP	Electric Dipole polarizability
EGLO	Enhanced Generalized Lorentzian
GDR	Giant Dipole Resonance
GSF	Gamma Strength Function
GT	Gamow Teller
HFB	Hartree–Fock–Bogoliubov
HFB–BCS	Hartree–Fock–Bogoliubov–Bardeen–Cooper–Schrieffer
IAS	Isobaric Analog States
ISEWSR	Isoscalar Energy Weighted Sum Rule
ISGDR	Isoscalar Giant Dipole Resonance
ISHEDR	Isoscalar High Energy Dipole Resonance
ISLED	Isoscalar Low Energy Dipole
IVGDR	Isovector Giant Dipole Resonance
LCS	Laser Compton Back scattering
MCP	Multi Channel Plate
MDA	Multipole Decomposition Analysis
NLD	Nuclear Level Density
NRF	Nuclear Resonance Fluorescence
PDR	Pygmy Dipole Resonance
PT	Porter–Thomas
PTA	Polarization Transfer Analysis
QPM	Quasi Phonon Model
QRPA	Quasi Particle Random Phase Approximation
RHB	Relativistic Hartree Bogoliubov
RIBF	Radioactive Isotope Beam Facility
RMT	Random Matrix Theory
RPA	Random Phase Approximation
RQRPA	Relativistic Quasi Particle Random Phase Approximation
RQTBA	Relativistic Quasi Particle Time-Blocking Approximation
SLO	Standard Lorentzian
SSRPA	Subtracted Second Random Phase Approximation
TAGS	Total Absorption Gamma Spectrometer
VDC	Vertical Drift Chamber

## References

- [1] D. Savran, et al., *Prog. Part. Nucl. Phys.* 70 (2013) 210.
- [2] P.F. Bortignon, A. Bracco, R.A. Broglia, *Giant Resonances: Nuclear Structure at Finite Temperature*, Harwood Academic Publishers, Australia, 1998.
- [3] M.N. Harakeh, A. van der Woude, *Giant Resonances*, Oxford Science Publications, 2001.
- [4] A. Klimkiewicz, et al., *Phys. Rev. C* 76 (2007) 051603.
- [5] A. Carbone, et al., *Phys. Rev. C* 81 (2010) 041301.
- [6] N. Paar, D. Vretenar, E. Khan, G. Colò, *Rep. Progr. Phys.* 70 (2007) 691.
- [7] P.-G. Reinhard, W. Nazarewicz, *Phys. Rev. C* 81 (2010) 051303(R).
- [8] S. Goriely, E. Khan, M. Samyn, *Nuclear Phys. A* 739 (2004) 331.
- [9] U. Garg, G. Colò, *Prog. Part. Nucl. Phys.* 101 (2018) 55–95.
- [10] B. Löher, et al., *Nucl. Instrum. Methods A* 723 (2013) 136.
- [11] N. Pietralla, et al., *Phys. Rev. Lett.* 88 (2002) 012502.
- [12] S. Gales, et al., *Phys. Rep.* 166 (2018) 125.
- [13] D. Filipescu, et al., *Eur. Phys. J. A* 51 (2015) 185.
- [14] C. Romig, et al., *Phys. Lett. B* 744 (2015) 369.
- [15] A. Tamii, et al., *Nucl. Instrum. Methods A* 605 (2009) 326.
- [16] R. Neveling, et al., *Nucl. Instrum. Methods A* 654 (2011) 29;
- R. Neveling, et al., *Nucl. Instrum. Methods A* 662 (2012) 101.
- [17] A. Tamii, et al., *Phys. Rev. Lett.* 107 (2011) 062502.
- [18] I. Poltoratska, et al., *Phys. Rev. C* 85 (2012) 041304.
- [19] V. Derya, et al., *Nuclear Phys. A* 906 (2013) 94.
- [20] J. Endres, et al., *Phys. Rev. C* 85 (2012) 064331.
- [21] J. Endres, et al., *Phys. Rev. C* 80 (2009) 034302.
- [22] H.J. Wörtche, *Nuclear Phys. A* 788 (2007) 27C.
- [23] D. Savran, et al., *Nuclear Phys. A* 788 (2007) 165C.
- [24] A. Bracco, et al., *Eur. Phys. J. A* 51 (2015) 99.
- [25] L. Pellegrini, et al., *Phys. Rev. C* 92 (2015) 014330.
- [26] F.C.L. Crespi, et al., *Phys. Rev. C* 91 (2015) 024323.
- [27] F.C.L. Crespi, et al., *Phys. Rev. Lett.* 113 (2014) 012501.
- [28] L. Pellegrini, et al., *Phys. Lett. B* 738 (2014) 519.
- [29] M. Krzysiek, et al., *Phys. Rev. C* 93 (2016) 044330.
- [30] D. Savran, et al., *Phys. Lett. B* 786 (2018) 16.
- [31] D. Savran, et al., *Nucl. Instrum. Methods A* 564 (2006) 267.
- [32] D. Mengoni, et al., *Nucl. Instrum. Methods A* 764 (2014) 241.
- [33] S. Akkoyun, et al., *Nucl. Instrum. Methods A* 668 (2012) 26.
- [34] A. Gadea, et al., *Nucl. Instrum. Methods A* 654 (2011) 88.
- [35] E. Farnea, et al., *Nucl. Instrum. Methods A* 621 (2010) 331.
- [36] N. Fukuda, et al., *Nucl. Instrum. Methods Phys. Res. B* 317 (2013) 323.
- [37] A. Giaz, et al., *Nucl. Instrum. Methods A* 729 (2013) 910.
- [38] G. Cardella, et al., *Nucl. Instrum. Methods A* 799 (2015) 64.
- [39] N.S. Martorana, et al., *Phys. Lett. B* 782 (2018) 112.
- [40] A.C. Larsen, et al., *J. Phys. G* 44 (2017) 064005.
- [41] D.M. Brink, (Ph.D. thesis), University of Oxford, 1955, Unpublished.
- [42] P. Axel, *Phys. Rev.* 126 (1962) 671.
- [43] B.L. Berman, *At. Data Nucl. Data Tables* 15 (1975) 319.
- [44] B.L. Berman, S.C. Fultz, *Rev. Modern Phys.* 47 (1975) 713.
- [45] O. Wieland, et al., *Phys. Rev. Lett.* 102 (2009) 092502.
- [46] D.M. Rossi, et al., *Phys. Rev. Lett.* 111 (2013) 242503.
- [47] N. Nakatsuka, et al., *Phys. Lett. B* 768 (2017) 387.
- [48] A. Bracco, F. Camera, *Phys. Scr.* 91 (2016) 083002.
- [49] C.A. Bertulani, G. Baur, *Phys. Rep.* 163 (1988) 299.
- [50] C. Bertulani, A. Nathan, *Nuclear Phys. A* 554 (1993) 158.
- [51] T. Hashimoto, et al., *Phys. Rev. C* 92 (2015) 031305.
- [52] D. Martin, et al., *Phys. Rev. Lett.* 119 (2017) 182503.
- [53] J. Birkhan, et al., *Phys. Rev. Lett.* 118 (2017) 252501.
- [54] M. Krumholz, et al., *Phys. Lett. B* 744 (2015) 7.
- [55] C. Iwamoto, et al., *Phys. Rev. Lett.* 108 (2012) 262501.
- [56] L.M. Donalson, et al., *Phys. Lett. B* 776 (2018) 133.
- [57] X. Roca-Maza, M. Brenna, G. Colò, et al., *Phys. Rev. C* 88 (2013) 024316.
- [58] X. Roca-Maza, et al., *Phys. Rev. C* 92 (2015) 064304.
- [59] J.S. Levinger, *Phys. Rev.* 84 (1951) 43.
- [60] M.B. Chadwick, et al., *Phys. Rev. C* 44 (1991) 814.
- [61] R. Weiss, B. Bazak, N. Barnea, *Phys. Rev. Lett.* 114 (2015) 0120501.
- [62] K.P. Schelhaas, et al., *Nuclear Phys. A* 489 (1988) 189.
- [63] A. Veissiere, et al., *Nuclear Phys. A* 159 (1970) 561.
- [64] S.C. Fultz, et al., *Phys. Rev.* 186 (1969) 1255.
- [65] A. Leprêtre, et al., *Nuclear Phys. A* 219 (1974) 39.
- [66] H. Utsunomiya, et al., *Phys. Rev. C* 84 (2011) 055805.
- [67] D. Gambacurta, M. Grasso, O. Vasseur, *Phys. Lett. B* 777 (2018) 163.
- [68] M. Miorelli, et al., *Phys. Rev. C* 98 (2018) 014324.
- [69] M.B. Tsang, et al., *Phys. Rev. C* 86 (2012) 015803.
- [70] A. Tamii, et al., *Eur. Phys. J. A* 50 (2014) 28.
- [71] K. Govaert, et al., *Phys. Rev. C* 57 (1998) 2229.

- [72] F. Bauwens, et al., Phys. Rev. C 62 (2000) 024302.
- [73] J. Reif, et al., Nuclear Phys. A 620 (1997) 1.
- [74] R.-D. Herzberg, et al., Phys. Lett. B 390 (1997) 49.
- [75] R.-D. Herzberg, et al., Phys. Rev. C 60 (1999) 051307.
- [76] A. Zilges, et al., Phys. Lett. B 542 (2002) 43.
- [77] J. Enders, et al., Nuclear Phys. A 741 (2004) 3.
- [78] J. Enders, et al., Phys. Lett. B 486 (2000) 279.
- [79] N. Ryezayeva, et al., Phys. Rev. Lett. 89 (2002) 272502.
- [80] J. Enders, et al., Nuclear Phys. A 724 (2003) 243.
- [81] T. Aumann, T. Nakamura, Phys. Scr. T 152 (2013) 014012.
- [82] U. Kneissl, et al., J. Phys. G 32 (2006) R217.
- [83] B. Ozel, et al., Nuclear Phys. A 788 (2007) 385C.
- [84] T. Hartmann, et al., Phys. Rev. Lett. 85 (2000) 274.
- [85] T. Hartmann, et al., Phys. Rev. C 65 (2002) 034301.
- [86] G. Rusev, et al., Eur. Phys. J. A 27 (2006) 171.
- [87] M. Scheck, et al., Phys. Rev. C 87 (2013) 051304.
- [88] S. Volz, et al., Nuclear Phys. A 779 (2006) 1.
- [89] A.P. Tonchev, et al., Phys. Rev. Lett. 104 (2010) 072501.
- [90] R. Schwengner, et al., Phys. Rev. C 76 (2007) 034321.
- [91] R. Schwengner, et al., Phys. Rev. C 78 (2008) 064314.
- [92] M.A. Bussing, et al., Phys. Rev. C 78 (2008) 044309.
- [93] A. Makinaga, et al., Phys. Rev. C 82 (2010) 024314.
- [94] R. Schwengner, et al., Phys. Rev. C 81 (2010) 054315.
- [95] D. Savran, et al., Phys. Rev. C 84 (2011) 024326.
- [96] C.T. Angell, et al., Phys. Rev. C 86 (2012) 051302.
- [97] S.L. Hammond, et al., Phys. Rev. C 85 (2012) 044302.
- [98] J. Isaak, et al., Phys. Lett. B 727 (2013) 361.
- [99] P.M. Goddard, et al., Phys. Rev. C 88 (2013) 064308.
- [100] C. Romig, et al., Phys. Rev. C 88 (2013) 044331.
- [101] R. Schwengner, et al., Phys. Rev. C 87 (2013) 024306.
- [102] M. Scheck, et al., Phys. Rev. C 88 (2013) 044304.
- [103] A. Makinaga, et al., Phys. Rev. C 90 (2014) 044301.
- [104] N. Benouaret, et al., J. Phys. G 43 (2016) 115101.
- [105] B. Löher, et al., Phys. Lett. B 756 (2016) 72.
- [106] R. Räut, et al., J. Phys. Conf. Ser. 337 (2012) 012048.
- [107] K. Govaert, et al., Nucl. Instrum. Methods A 337 (1994) 265.
- [108] T. von Egidy, D. Bucurescu, Phys. Rev. C 80 (2009) 054310.
- [109] K. Sonnabend, et al., Nucl. Instrum. Methods A 640 (2011) 6.
- [110] P. Carlos, et al., Nuclear Phys. A 172 (1971) 437.
- [111] B.L. Berman, et al., Phys. Rev. C 36 (1987) 1286.
- [112] N. Pietralla, et al., Phys. Lett. B 681 (2009) 134.
- [113] G. Bocchi, et al., Phys. Lett. B 760 (2016) 273.
- [114] R. Mohen, M. Danos, L.C. Biedenharn, Phys. Rev. C 3 (1971) 1740.
- [115] J.S. Brzosko, et al., Can. J. Phys. 47 (1969) 2849.
- [116] A.M. Lane, Ann. Phys. 63 (1970) 171.
- [117] H. Steinwedel, J.H.D. Jensen, Z. Naturforsch. 5a (1950) 413.
- [118] Y. Suzuki, K. Ikeda, H. Sato, Progr. Theoret. Phys. 83 (1990) 180.
- [119] M. Igashira, H. Kitazawa, M. Shimizu, H. Komano, N. Yamamoto, Nuclear Phys. A 457 (1986) 301.
- [120] M. Goldhaber, E. Teller, Phys. Rev. 74 (1948) 1046.
- [121] P. Van Isacker, M.A. Nagarajan, D.D. Warner, Phys. Rev. C 45 (1992) R13.
- [122] S.I. Bastrukov, et al., Phys. Lett. B 664 (2008) 258.
- [123] F. Catara, et al., Nuclear Phys. A 624 (1997) 449.
- [124] J. Piekarewicz, Phys. Rev. C 83 (2011) 034319.
- [125] J. Piekarewicz, Phys. Rev. C 73 (2006) 034319.
- [126] D. Vretenar, et al., Phys. Rev. C 85 (2012) 044317.
- [127] J. Liang, et al., Phys. Rev. C 75 (2007) 054320.
- [128] D. Vretenar, et al., Nuclear Phys. A 692 (2001) 496.
- [129] N. Paar, et al., Phys. Rev. C 67 (2003) 034312.
- [130] N. Paar, et al., Phys. Rev. Lett. 103 (2009) 032502.
- [131] D. Peña, et al., Phys. Rev. C 79 (2009) 034311.
- [132] E.G. Lanza, et al., Nuclear Phys. A 613 (1997) 445.
- [133] E.G. Lanza, et al., Nuclear Phys. A 636 (1998) 452.
- [134] M. Fallot, et al., Nuclear Phys. A 729 (2003) 699.
- [135] S. Drozdź, et al., Phys. Rep. 197 (1990) 1.
- [136] D. Gambacurta, M. Grasso, F. Catara, Phys. Rev. C 84 (2011) 034301.
- [137] M. Tohyama, T. Nakatsukasa, Phys. Rev. C 85 (2012) 031302.
- [138] T. Hartmann, et al., Phys. Rev. Lett. 93 (2004) 192501.
- [139] V.G. Soloviev, Theory of Atomic Nucleus: Quasiparticles and Phonons, Institute of Physics, Bristol, 1992.
- [140] C. Bertulani, Y.Yu Ponomarev, Phys. Rep. 321 (1999) 139.
- [141] V.I. Tselyaev, Phys. Rev. C 75 (2007) 024306.
- [142] E. Litvinova, et al., Phys. Rev. C 79 (2009) 054312.
- [143] E. Litvinova, et al., Phys. Rev. C 78 (2008) 014312.
- [144] E. Litvinova, et al., Phys. Rev. Lett. 105 (2010) 022502.
- [145] D. Vretenar, et al., Phys. Rev. C 65 (2002) 021301.
- [146] A. Repko, et al., Phys. Rev. C 87 (2013) 024305.

- [147] V. Nesterenko, et al., Phys. Atom. Nucl. 79 (2016) 842.
- [148] G. Colò, L. Cao, N. Van Gai, L. Capelli, Comput. Phys. Comm. 184 (2013) 142.
- [149] N. Van Gai, H. Sagawa, Phys. Lett. B 106 (1981) 379;
- N. Van Gai, N. Sagawa, Nuclear Phys. A 371 (1981) 1.
- [150] P. Papakostantinou, et al., Phys. Rev. C 92 (2015) 034311.
- [151] J. Terasaki, J. Engel, Phys. Rev. C 74 (2006) 044301.
- [152] P. Papakostantinou, et al., Phys. Lett. B 709 (2012) 270.
- [153] P. Papakostantinou, et al., Phys. Rev. C 89 (2014) 034306.
- [154] S. Landowne, A. Vitturi, Treatise on Heavy-Ion Science, vol. 1, Plenum Press, New York, 1984, p. 355.
- [155] E.G. Lanza, et al., Phys. Rev. C 79 (2009) 054615.
- [156] E.G. Lanza, et al., Phys. Rev. C 84 (2011) 064602.
- [157] N. Lyutorovich, et al., Phys. Rev. C 98 (2018) 054304.
- [158] D. Negi, et al., Phys. Rev. C 94 (2016) 024332.
- [159] E.G. Lanza, A. Vitturi, M.V. Andrés, Phys. Rev. 91 (2015) 054607.
- [160] G.R. Satchler, W.G. Love, Phys. Rev. 55 (1979) 183.
- [161] G.R. Satchler, Direct Nuclear Reactions, Oxford University Press, 1983.
- [162] G.R. Satchler, Nuclear Phys. A 472 (1987) 215.
- [163] S. Shlomo, et al., Phys. Rev. C 36 (1987) 1317.
- [164] K. Nakayama, G. Bertsch, Phys. Rev. Lett. 59 (1987) 1053.
- [165] T.J. Deal, Nuclear Phys. A 217 (1973) 210.
- [166] M.N. Harakeh, A.E.L. Dieperink, Phys. Rev. C 23 (1981) 2329.
- [167] G. Bertsch, et al., Nuclear Phys. A 284 (1977) 399.
- [168] Dao T. Khoa, W. von Oertzen, Phys. Lett. B 342 (1995) 6.
- [169] Dao T. Khoa, et al., Phys. Rev. C 56 (1997) 954.
- [170] P.D. Kunz, DWUCK4 code for DWBA at <http://spot.colorado.edu/kunz/DWBA.html>.
- [171] D. Vretenar, et al., Nuclear Phys. A 692 (2001) 496.
- [172] G. Colò, P.F. Bortignon, Nuclear Phys. A 696 (2001) 427.
- [173] G. Cò, et al., Phys. Rev. C 80 (2009) 014308.
- [174] X. Roca-Maza, G. Pozzi, M. Brenna, K. Mizuyama, G. Colò, Phys. Rev. C 85 (2012) 024601.
- [175] N. Paar, Y.F. Niu, D. Vretenar, J. Meng, Phys. Rev. Lett. 103 (2009) 032502.
- [176] J. Endres, et al., Phys. Rev. Lett. 105 (2010) 212503.
- [177] E.G. Lanza, A. Vitturi, E. Litvinova, D. Savran, Phys. Rev. C 89 (2014) 041601(R).
- [178] T.D. Poelhekken, et al., Phys. Lett. B 278 (1992) 423.
- [179] M.N. Harakeh, et al., Phys. Rev. C 11 (1975) 1008.
- [180] T. Inakura, et al., Nuclear Phys. A 768 (2006) 61.
- [181] V. Derya, et al., Phys. Lett. B 730 (2014) 288.
- [182] S. Kamerdzhiev, et al., Phys. Rep. 393 (2004) 1.
- [183] J. Chambers, E. Zaremba, J.P. Adams, B. Castel, Phys. Rev. C 50 (1994) R2671.
- [184] T. Inakura, T. Nakatsukasa, K. Yabana, Phys. Rev. C 84 (2011) 021302.
- [185] E. Yuksel, et al., Nuclear Phys. A 877 (2012) 35.
- [186] R. Massarczyk, et al., Phys. Rev. C 92 (2015) 044309.
- [187] O. Wiel, A. Bracco, Prog. Part. Nucl. Phys. 66 (2011) 374.
- [188] O. Wieland, et al., Phys. Rev. C 98 (2018) 064313.
- [189] D. Savran, et al., Phys. Rev. Lett. 97 (2006) 172502.
- [190] M. Wilhelm, et al., Phys. Rev. C 54 (1996) 449R.
- [191] M. Wilhelm, et al., Phys. Rev. C 57 (1998) 577.
- [192] T. Shizuma, et al., Phys. Rev. C 78 (2008) 061303.
- [193] M. Scheck, et al., Phys. Rev. Lett. 116 (2016) 132501.
- [194] A. Gottardo, et al., Phys. Lett. B 772 (2017) 359.
- [195] M. Madurga, et al., Phys. Rev. Lett. 117 (2016) 092502.
- [196] I. Daooutidis, S. Goriely, Phys. Rev. C 86 (2012) 034328.
- [197] A. Tonchev, et al., Phys. Lett. B 773 (2017) 20.
- [198] C.T. Angell, et al., Phys. Rev. C 91 (2015) 039901(R).
- [199] N.U.H. Syed, M. Guttormsen, F. Ingabretsen, A.C. Larsen, T. Lønnroth, J. Rekstad, A. Schiller, S. Siem, A. Voinov, Phys. Rev. C 79 (2009) 024316.
- [200] S. Bassauer, et al., Phys. Rev. C 94 (2016) 054313.
- [201] M.M. Guttormsen, et al., Phys. Rev. C 71 (2005) 044307.
- [202] A.C. Larsen, S. Goriely, Phys. Rev. C 82 (2010) 014318.
- [203] H. Beil, R. Berg're, P. Carlos, A. Leprtre, A. De Miniac, A. Veysiere, Nuclear Phys. A 227 (1974) 427.
- [204] H. Utsunomiya, et al., Phys. Rev. C 88 (2013) 015805.
- [205] G. Rusev, et al., Phys. Rev. C 79 (2009) 061302.
- [206] I. Poltoratska, et al., Phys. Rev. C 89 (2014) 054322.
- [207] H.A. Weidemüller, G.E. Mitchell, Rev. Modern Phys. 81 (2009) 539.
- [208] G.E. Mitchell, A. Richter, H.A. Weidemüller, Rev. Modern Phys. 82 (2010) 2845.
- [209] R.U. Haq, A. Pandey, O. Bohigas, Phys. Rev. Lett. 48 (1982) 1086.
- [210] T. Rauscher, F.-K. Thielemann, K.-L. Kratz, Phys. Rev. C 56 (1997) 1613.
- [211] T. von Egidy, D. Bucurescu, Phys. Rev. C 72 (2005) 044311.
- [212] S. Goriely, S. Hilaire, A.J. Koning, Phys. Rev. C 78 (2008) 064307.
- [213] P. Demetriou, S. Goriely, Nuclear Phys. A 695 (2001) 95.
- [214] R. Capote, et al., Nucl. Data Sheets 110 (2009) 3107.
- [215] A. Voinov, et al., Phys. Rev. Lett. 93 (2004) 042504.
- [216] R.A. Alvarez, B.L. Berman, D.D. Faul, F.H. Lewis Jr., P. Meyer, Phys. Rev. C 20 (1979) 128.
- [217] S.S. Borodina, A.V. Varlamov, V.V. Varlamov, B.S. Ishkhanov, M.I. Mokeev, Report No.2000, Moscow State University Institute of Nuclear Physics, 2000, 6/610.
- [218] H.E. Jackson, E.N. Strait, Phys. Rev. C 4 (1971) 1314.
- [219] C.M. McCullagh, M.L. Stelts, R.E. Chrien, Phys. Rev. C 23 (1981) 1394.

- [220] T. Belgya, et al., Handbook for Calculations of Nuclear Reaction Data, 2006, RIPL-2 IAEAECDOC-1506, <http://nds.iaea.org/RIPL-2/>.
- [221] A.C. Larsen, et al., Phys. Rev. Lett. 111 (2013) 242504.
- [222] M. M. Guttormsen, et al., Phys. Rev. Lett. 116 (2016) 012502.
- [223] A.C. Larsen, et al., Phys. Rev. C 76 (2007) 044303.
- [224] A. Bürger, et al., Phys. Rev. C 85 (2012) 064328.
- [225] A.V. Voinov, et al., Phys. Rev. C 81 (2010) 024319.
- [226] M. Wiedeking, et al., Phys. Rev. Lett. 108 (2012) 162503.
- [227] G.M. Tveten, et al., Phys. Rev. C 94 (2016) 025804.
- [228] R. Schwengner, S. Fraendorf, A.C. Larsen, Phys. Rev. Lett. 111 (2013) 232504.
- [229] B.A. Brown, A.C. Larsen, Phys. Rev. Lett. 113 (2014) 252502.
- [230] M. Ciemala, et al., PRC 91 (2015) 054313.
- [231] H. Sagawa, P.F. Bortignon, G. Colò, Phys. Lett. B 444 (1998) 1, and private communication.
- [232] H.L. Harney, A. Ritcher, H.A. Weidenmüller, Rev. Modern Phys. 58 (1986) 607.
- [233] M.N. Harakeh, et al., Phys. Lett. B 176 (1986) 297.
- [234] Debasish Mondal, et al., Phys. Lett. B 763 (2016) 422.
- [235] A. Corsi, et al., Phys. Rev. C 84 (2011) 041304(R).
- [236] S. Ceruti, et al., Phys. Rev. Lett. 115 (2015) 222502.
- [237] S. Ceruti, et al., Phys. Rev. C 95 (2017) 014312.
- [238] T. Suzuki, H. Sagawa, G. Colò, Phys. Rev. C 54 (1996) 2954.
- [239] W. Satula, J. Dobaczewski, W. Nazarewicz, M. Rafalski, Phys. Rev. Lett. 103 (2009) 012502.
- [240] N. Auerbach, Phys. Rev. C 79 (2009) 035502.
- [241] J. Damgaard, Nuclear Phys. A 130 (1969) 233.
- [242] I.S. Towner, J.C. Hardy, M. Harvey, Nuclear Phys. A 284 (1977) 269.
- [243] I.S. Towner, J.C. Hardy, Phys. Rev. C 82 (1977) 065501.
- [244] I. Kellerbauer, et al., Phys. Rev. Lett. 93 (2004) 072502.